Clinical applications of ultra-high resolution and phase-sensitive optical coherence tomography

The University Of Sheffield.

Joseph Boadi
Materials Science Engineering
University of Sheffield

A thesis presented for the degree of
Doctor of Philosophy
2016

Abstract

The transparency of the human cornea is vital in maintaining vision. The cells on the surface, corneal epithelium cells, are constantly replaced by differentiated limbal stem cells. Damage to the limbus can cause a deficiency in the limbal stem cell population which can cause cornea opacity and vascularisation consequently leading to blindness. Currently limbal stem cell deficiency can be detected clinically and treated surgically by transplanting stem cells onto the damaged cornea. However, the long term success rate is low 68% and the results vary from patient to patient. There is an interest to understand the cause for this variability in results and the low long term success rates.

The aim of the project was to develop an Ultrahigh resolution OCT (UHROCT) to locate the transplanted corneal epithelium cells. Optical Coherence Tomography system (OCT) is a non-invasive micron resolution imaging technique that can image several millimetres in tissue. The cells to be transplanted are labelled with super paramagnetic iron oxide (SPIO) nanoparticles. After uptake these SPIO embedded cells are displaced with an external magnetic field at a known frequency whilst being imaged by the UHROCT. This technique known as phased resolved magnetomotive OCT, allowed us to locate the oscillating nanoparticle which is embedded in the cell by detecting the location of the modulation frequency. For the Ultrahigh resolution OCT a super luminescent diode (SLD) light with centre wavelength at 890×10^{-9}m and a bandwidth of 150×10^{-9}m. The system has an axial and lateral resolution of 2.5μm and 6.20 μm in air respectively. The system was able to detect as low as 1273 SPIO loaded cells/ mm^2 on rabbit cornea.

The spectral domain UHROCT constructed was also used to image 3D oral mucosa constructs. The system shows superior contrast in comparison to 1310 nm swept source systems. The UHROCT was able to identify key difference between the normal, dysplastic and malignant construct. For the malignant construct Cal27s, hematoxylin and eosin staining was used to confirm the formation of a keratinized superficial layer. The keratinized layer was presented as a hyper-reflective thickened layer superficial to a darker region on both OCT platforms. This keratinized layer causes a sharp fall in the signal in the UHROCT making it difficult to visualise the underlying structures of the construct.

Acknowledgement

A note of gratitude to ....

Prof. Steve Matcher & Prof. Sheila MacNeil for being enthusiastic supervisors and for excellent guidance and critique of my research.

Prof. Dan Allwood & Dr. Rene Dost for allowing me to use the magnetics lab

Dr Zenghai Lu & Dr. Abigail Pinnock for their support with the use of OCT systems and preparation of biological samples.

Dr. Xuesong Hu, Robert Byers & Chrisandrea Charalambous for our fruitful discussions and for a wonderful time working together.

EPSRC for the funding support

All my friends and family especially my wife Kayshia and our two boys Josiah and Ezra for their emotional support and patience throughout my PhD research.

Publications and Conferences

Publications

1. System for tracking transplanted limbal epithelial stem cells in the treatment of corneal stem cell deficiency (Conference Presentation)
Authors: Joseph Boadi Stephen Matcher Sheila MacNeil Virender S. Sangwan

2. 1300 nm and 890 nm OCT images of oral cancer tissue engineered models and biopsy samples offer complimentary performance
Authors: Joseph Boadi Robert A. Byers Jon Fernandes Shweta Mittar Vanessa Hearnden Zenghai Lu Sheila MacNeil Martin Thornhill Craig Murdoch Keith D. Hunter Alasdair McKechnie Stephen J. Matcher

3. Optical coherence elastography for human finger-pad skin deformation studies
Authors: Xuesong Hu Raman Maiti Joseph Boadi Wei Li Matt J. Carr Roger Lewis Steven E. Franklin Stephen J. Matcher

Conferences

1. Institute of Physics (IOP) Optical Group Optical Coherence Tomography II, University of Manchester 2014 (Oral Presentation)

2. SPIE Conference, Imaging, Manipulation, and Analysis of Biomolecules, Cells, and Tissues XIII. San Francisco, California, 2015.(Oral Presentation)

Contents

List of Figures

List of Tables

Chapter 1

Theory and Literature review

1.1 Corneal Physiology

The transparent cornea serves as an entrance for us to capture light from our external environment. A combination of the avascular nature and the arrangement of collagen fibre in the stroma make the cornea transparent [1]. It is usually stated that the cornea provides two thirds of the focussing power of the eye. After the cornea the light travels through the lens which then focuses it onto the retina. Until recently the cornea was thought to consist of five basic layers, namely the Epithelium, Bowmans layer, Stroma, Descements membrane and the Endothelium as shown in figure 1.1.

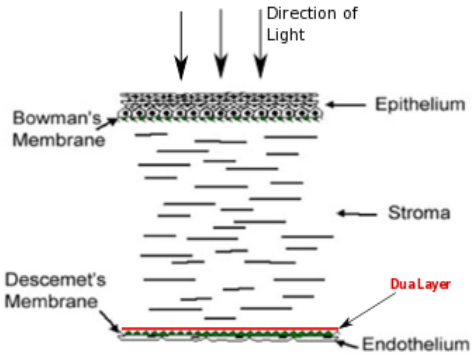

Figure 1.1: The five traditional cornea layers

However, a new pre-Descement layer has been discovered and is been term the Dua layer [2]. The first layer the corneal epithelium forms a mechanical barrier and acts

as a bio-defense layer against foreign matter. The layer has been reported to have a thickness of between 50-52 μm [3].The thickness has been measured more recently to be 53.4± 4.6 μm in a normal population using a high frequency ultrasound [4]. The thickness of the central cornea and the epithelium layer have been measured using Optical Coherence Tomography (OCT) as 54.7 ± 1.9 μm and 44.9 ± 3.4 μm respectively. [5] [6] [7]. The cornea does most of the refracting of light in the eye, light entering the eye passes through air with refractive index of 1 and enters the cornea with a refractive index of 1.376. This change in refractive index is the largest the beam of light experiences on it's journey onto the retina.

In a healthy individual the cornea is transparent due to the absence of blood vessels. This attribute of the cornea is very important if the cornea is to refract light effectively through the lens which then focuses the light onto the retina. The vascularisation of the cornea changes its refractive index and hence its refracting properties and may lead to ocular conditions. An interesting question arises about how the corneal epithelium cells are kept functioning without any blood supply. The corneal cells source of nutrients is the tear film. The tear film, consisting of water mucin and lipids, the tear film allows oxygen to be transported through it to the corneal cells. It flushes away foreign products and protects against shear forces generated when blinking and during eye movements. Waste products are channeled away in the tear film from the cornea into the tear ducts to be drained. It is generally accepted that corneal epithelium is regenerative and the regenerative action is centripetal. New epithelial cells move from the peripheral to the centre of the cornea, this movement have been observed in corneal epithelial wound healing experiments conducted by both Buck and Kuwabara [8] [9]. Kuwabara describes this centripetal movement as a sliding of the epithelium cells fuelled by the cells' glycogen storage. Even though there is a general agreement about the trajectory of new epithelium cells there are however two main hypothesis about the origin of these replacement corneal epithelium cells.

1.1.1 Limbal Stem Cell Transportation

1.1.1.1 Limbal Stem Cells

The prevailing hypothesis is that the regeneration of the corneal epithelium cells is dependent on the availability and activity of primitive stem cells, the limbal epithelium stem cells. The limbal region encompasses the cornea and separates the cornea and conjunctiva. The Limbal region is highly vascular and was thought to be the site for limbal stem cells until H.S. Dua confirmed the existence of limbal stem cell niches now termed the lImbus or palisades of Vogt [10]. Due to the shape of the palisade of Vogt and its folding structure it provides protection against mechanical stresses and damages [11]. It is also thought that within the palisade of Vogt the stem cells can remain in their undifferentiated state [12]. Limbal stem cells are thought to initially differentiate to form transient amplifying cells (TAC), these TAC reside on the basal layer of the corneal epithelium. The TACs have a higher differentiation rate than the stem cells but have a limited proliferation capacity. Once produced the TAC migrate towards the surface of the epithelium whilst differentiating to form terminal cells to replenish the superficial corneal epithelium cells as illustrated in figure 1.2 [13]. A complete replacement cycle occurs every 5 to 7 days [14].

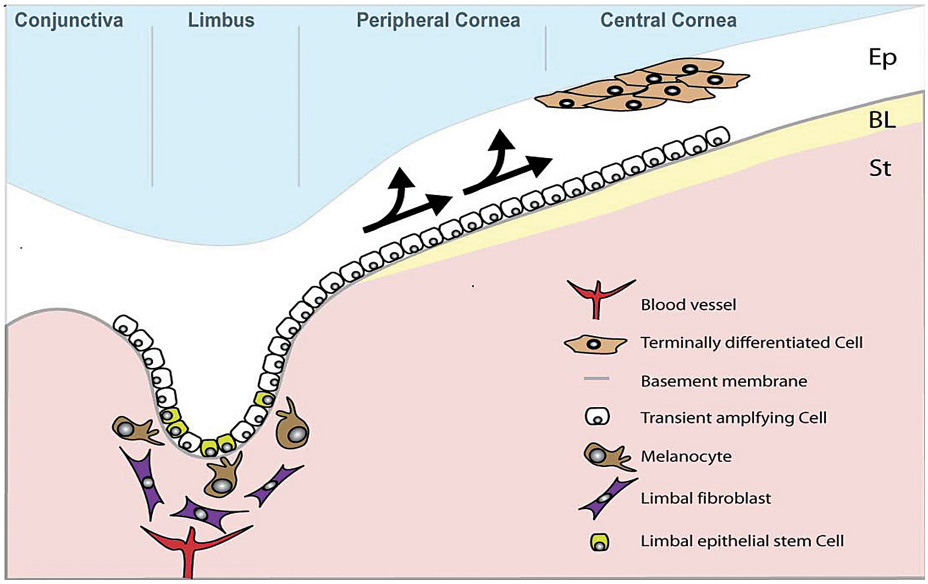

Figure 1.2: Limbal Epithelium Stem Cell Transportation [13]

The stem cell hypothesis is based on experimental observations. Two of these observations are that the limbal basal epithelium contains the lowest differentiated cells in the cornea epithelium and the cells in the basal layer of the limbal niches exhibit the proliferative behaviours of stem cells.

The basal layer epithelium has the least differentiated cells

The different cell populations in the cornea epithelium was only segmented after varying levels of keratin expressions were observed. The presence of some keratins are evidence of high level of differentiation while others are mainly found in less differentiated cells. The use of antibodies allowed the identification of 64 kDa keratin K3, this keratin and its pair K12 indicates cornea specific type of differentiation. The presence of the 64 kDa keratin K3 in the suprabasal epithelium of the limbus and its absence in the basal layer or the conjunctiva led to the hypothesis that the limbus basal epithelium cells had not differentiated to have cornea phenotype and hence would be the least differentiated cells of the epithelium [15]. Further investigations have revealed that the basal limbal epithelium shows no expression of the keratin K12, however, this keratin is expressed throughout the cornea epithelium. These

observations led to the conclusion that the basal limbal epithelium is the least differentiated region in the entire cornea epithelium. Further evidence supporting the stem cell hypothesis includes the absence of keratin K19 in the supra basal layers and the cornea epithelium. Keratin K19 is linked with low differentiation phenotype. Since keratin K19 is, however, observed in the adult limbal basal epithelium and in a foetus throughout the entire cornea epithelium and the limbus; it may therefore mean that the basal limbal layer contains embroyogenetically young cells (stem cells). Cells in the peripherals have been identified to contain expressions of K19 this could be due to the centripetal cell migration [16].

The limbal basal cells exhibit proliferative behaviours similar to stem cells

Cells can be labelled with agents which identify their rate of mitotic division, this technique has been used to differentiate between fast and slow proliferating cells. Short term labelling experiments can be conducted to identify fast cycling cells such as epithelium cells and transient amplifying cells. However, longer labelling experiments are needed to identify stem cells which innately have slow cycles. Using labelling experiments Cotsarelis and his group were one of the first to be able to distinguish between stem cells and transient amplifying cells in the basal layer of the limbus [17]. The group initially experimented for a short period, in their experimentation they labelled cells with tritiated thymidine and noticed cell proliferation in both the limbal and peripheral corneal basal epithelium. This was used as identification of the TAC cells, the group then extended the period of application of the tritiated thymidine to 14 days and observation period to 4 weeks. With these conditions only a few cells in the limbal basal epithelium layer showed any proliferations. The team concluded that the cycling time of the limbal stem cells was no longer than 2 weeks. The phenotype of these cells in the basal layer are primitive as they stay round and small. This was confirmed using in vivo confocal microscopy [18].

1.1.1.2 Conjunctival Transdifferentiation

The second hypothesis originated when conjunctival epithelium ingrowth was found on denuded cornea during a cornea wound healing experiment. Some patients after damaging their cornea and limbus would develop a seemingly normal cornea. Experiments showed that in the absence of blood supply the conjunctival epithelium cells on the corneal surface loses its conjunctival phenotype and becomes more cornea-like [19]. This observation led to idea that in a healthy individual the corneal epithelium is maintained by the neighbouring conjunctival epithelium. However, histological analysis has shown that the phenotype of these transdifferentiated conjunctival epithelium (TDCE) differs from that of true cornea epithelium. An example of this is the absence of goblet cells on the cornea when the limbus is completely damaged whilst normally goblet cells are present on the cornea producing mucin and antibacterial proteins for the protection of the cornea [20] [21]. Another interesting observation is that the transdifferentiation can be inhibited by the presence of vascularisation. This gave birth to the idea that there must be a component in the blood supply which is needed to maintain the conjunctival phenotype. This idea was pursued by Tseng who identified retonic acid to be one of the possibly many components in the blood which inhibits the transddifferentiation process [22]. Retonic acid is also needed for the differentiation of goblet cells. For these reasons and more it has been shown that transdifferentiated cornea epithelium is inherently different from genuine corneal epithelium. Additional studies shows that transdifferentiation does not happen, at least in animal models. It may be due to the subtotal loss of limbal epithelium stem cells and early transient amplifying cells. The incomplete loss of the limbus may allow the reconstruction of the cornea after a certain period when the the limbal epithelium has been restored. This process may be mistaken as conjunctival transdifferentiation.

1.2 Limbal Stem Cell Deficiency (LSCD)

The limbal region has two important role, firstly to keep the cornea healthy by replacing the epithelium cells and secondly to act as a mechanical barrier separating the avascular corneal cells from the vascularised conjunctival cells [23]. Damage to the limbal region will compromise the region's ability to complete these functions. Severe damages can lead to a painful disease known as limbal stem cell deficiency (LSCD) where the limbal stem cells population is severely reduced. For a LSCD sufferer the transparent cornea is no longer maintained but it is invaded by the neighbouring conjunctiva cells. The vascular conjunctiva begins to form blood vessel connection over the cornea. LSCD can lead to severe vision impairment and even blindness. There are numerous reasons for the onset of the disease. Reasons include hereditary conditions such as Aniridia [24], chemical/thermal burns, inflammatory diseases and even improper use of contact lens which may inflame the limbus [25]. LSCD is clinically diagnosed usually by the scarring and vascularisation of the corneal epithelium. The diagnosis can be confirmed with a corneal impression cytology test [26] [27]. This technique simply checks for the presence of conjunctival cells on a filter paper placed over the corneal epithelium. A high count of conjunctival epithelium cells could indicate limbal stem cell deficiency.

1.2.1 Treatments

Depending on the extent of the damage and whether the damage is bilateral (both eyes) or unilateral (single eye), a limbal allograft or limbal autograft can be done. For a LSCD patient with unilateral damage, the usual treatment would be an autograft. In a limbal autograft, stem cells are taken from the undamaged eye and harvested for transplantation onto the damaged eye. This is only possible if the damage is unilateral or if both eyes are affected then a small area of the limbus must be healthy. Whiles

auto grafting is the preferred treatment it is not always applicable e.g. if the damage is bilateral. In this situation an allograft is the second choice with this the stem cells are sourced from a relative. The undamaged stem cells are transplanted into the damage limbus after any conjunctival or scarring tissues are removed [28] [29]. Due to the high vascularisation of the limbus patients who undergo allograft transplantation will have to take immunosuppressants forever or until the transplant become viable [30]. For the cells to be transplanted a carrier is needed. A carrier is used to transport the healthy cells onto the patient's cornea. It dissintigrates over time leaving the transported donor corneal cells on the patient's cornea. The usual carrier tends to be Human Amniotic Membrane (HAM). The amniotic membrane is a good carrier because it has antimicrobial, antiviral, anti-inflammatory and inhibits fibrosis [31] [32]. Other reasons for the use of HAM are because of its low immunogenicity [33] [34] and its previous roles in healing corneal after thermal and chemical burns [35]. More recently cell expansion techniques have been developed. These techniques allow for smaller amounts of stem cells to be removed from donor cell, which is then cultured and expanded. The donor stem cells are obtained by anaesthetising the eye and gently scraping the limbal region. This technique avoids the case where limbal stem cell deficiency is induced in the donor eye [36]. With this technique the small amount of stem cells proliferates in the laboratory until a large enough mass is acquired. The benefits of this technique is that there is a small chance of inducing LSCD in the donor eye and it is possible to attempt a second biopsy of the donor if the first treatment was not successful. The donor cells are transferred to the recipient eye either via fibrin[30], inactivated 3T3 mouse fibroblasts or human amniotic membrane [37] [38] [39]. New biodegradable synthetic carriers are being developed to replace the amniotic membrane which has to be stored in banks. A biodegradable carrier has been synthesised out of poly-lactide-co-glycolide(PLGA) using a 50:50 ratio of lactide and glycolide [40]. PLGA shows good prospects due to its low cytotoxicity and that fact that it is already used in ocular surgeries.

Initially limbal damage was treated by full corneal transplant however these were not very successful. The low success rate was due to the fact that there usually aren't

enough stem cells in the recipient eye to sustain the regeneration process. [40] [41]. Now the preferred treatment, aims to replace, or increase, the population of limbal stem cells specifically. This can be done either by autologous or allografting. Limbal grafting techniques via human amniotic membrane have a fairly high success rate (76%) in the short term (a year or less) but the success rates fall as time passes. After 4 years the rate of success will have fallen to 68.2% [42]. So any reoccurring symptoms would mean that the treatment was unsuccessful. It has also been shown that the success rate increases after the second transplantation and also grafts that were considered successful after the first year remained successful [43].

The aim of the research is to be able to identify the transplanted limbal epithelium cells using Optical Coherence Tomography and possibly find some reasoning for this high failure rate in the long term. This would be a great step towards increasing the long term success rate of the transplantation surgeries.

1.3 Principle of Optical Coherence Tomography

Optical Coherence tomography is a non invasive imaging technique which generates two dimensional and three dimensional tomograms of materials using low temporally coherent light sources. The technique was developed from the principle of low coherence interferometry (LCI) [44]. The application of LCI for biological tissues was first explored by D. Huang in 1991 [45] [46]. OCT uses the principle of coherence gating to measure the temporal source of constructive interferences and uses this to produces images unlike conventional microscopy which uses spatial gating. OCT can be based on different types of interferometers such as Mirau [47], Fizeau [48], Mach-Zehnder and the Michelson interferometer. Haungs original system was based on the Michelson interferometer (see figure 1.3).

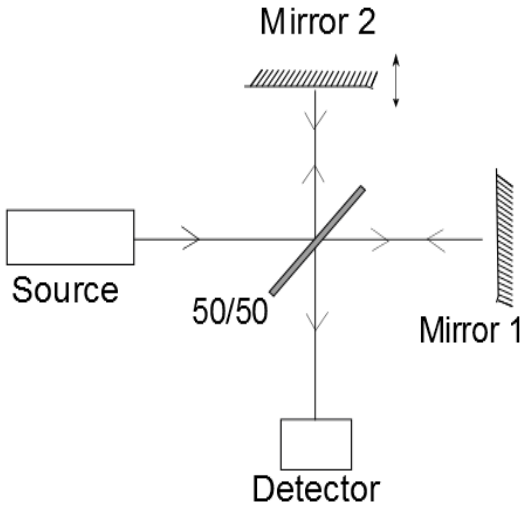

Figure 1.3: Michelson Interferometer

Most systems' set-up are based on the Michelson interferometer configuration, the system we used in our investigations was also based on this configuration. Hence we will be discussing the Michelson configuration type system. In the set-up, the light beam emitted from the source is incident onto a beam splitter or coupler which splits

the source beam into two output beams with their individual intensities dependent on the splitting ratio of the coupler or splitter. One of the beams travels towards the sample and the other towards a plane mirror, these are respectively described as the sample and reference arms. The plane mirror serves as a length reference. The reflected and scattered beams from the different layers in the sample are recombined by the splitter/coupler with the beam reflected by the reference mirror. The returning beams are also split according to the coupling/splitting ratio of the splitter. As an example a 50/50 split coupler will be recombining at most 25% of the source power from each arm. The emerging beam is then directed onto the detector. Due to the low coherence of the light source, constructive interference only occurs on the detector when the optical path of the reference and sample arms is matched within the coherence length of the source. [49].

The proportion of return light received by the detector can be very low in systems but this can be improved in fibre based systems by using favourable couplers such a 70/30 split ratio for ophthalmic imaging where there is a power restriction sample incident light. A single sample depth profile known as an A scan (axial scan) is acquired in the direction of the reference mirror scan. In Fourier domain systems there is no scanning and an A scan is acquired by either sweeping through the wavelength range of the light source and hence probing different depths in swept source systems or by using a diffraction grating to dispersing the recombined beam into individual wavelength components in spectral domain systems. The probing sample beam can be scanned in one direction (laterally, perpendicular to the axial) to produce a B scan or in two directions to produce a three dimension image.

The interference recorded for a single reflector by the detector is of the form

$$E(\omega,\tau) = s_{(\omega)} exp^{[i(\omega\tau+kz)]} \tag{1.1}$$

$$E_{in}(\omega,\tau) = s_{(\omega)} e^{i\omega\tau} \tag{1.2}$$

$$E_r(\omega,\tau,\Delta z) = (T_r T_s)^{1/2} E_{in}(\omega,\tau) e^{i\phi(\Delta z)} \tag{1.3}$$

$$E_s(\omega,\tau) = (T_r T_s)^{1/2} E_{in}(\omega,\tau) H(\omega) \tag{1.4}$$

$$E_{out}(\omega,\tau,\Delta z) = E_r(\omega,\tau) + E_s(\omega,\tau,\Delta z) \tag{1.5}$$

where ϕ the phase difference between the sample beam and reference

$$\phi(\Delta z) = \frac{2\omega n_{air}\Delta z}{c} \tag{1.6}$$

Integrating over time gives the intensity, the angular brackets are used to denote the time average

$$I(\omega,\Delta z) = \langle E_{out}(\omega,\tau,\Delta z) E_{out}(\omega,\tau,\Delta z)\rangle \tag{1.7}$$

$$I(\omega,\Delta z) = \langle E_s E_s*\rangle + \langle E_r E_r*\rangle + 2\mathbb{R}E_s E_r* \tag{1.8}$$

$$I(\tau) = I_s + I_r + 2I_0\sqrt{T_r T_s}|\gamma(\tau)|\cos(\omega\tau+\phi) \tag{1.9}$$

Equation (1.1) describes a plane polarized wave, with amplitude s(ω), frequency ω and time variation τ. Wavenumber k and distance z explain the phase throughout the interferometer. E_{in}, E_{out}, E_r and E_s, are the optical fields in the input, output, reference and sample arms, respectively

$I(\tau)$ is the intensity recorded by the detector, I_0 is the source intensity, I_r and I_s are the intensity due to the self-interference in the reference and sample arm respectively. T_r and T_s are the transmission coefficients. The sum of I_r and I_s gives the DC component of the signal. The third term give the cross interference. γ is the partial coherence term. ω and τ are the frequency of oscillation and the time delay between the beam from the reference and the sample arm. The cosine term carries the depth

information.

The image quality depends on several parameters, the most important is the sensitivity or signal to noise ratio SNR; the SNR determines the brightness of the images. Sensitivity is discussed in more detail in section 1.3.1. The other major parameters are the lateral and axial resolution.

Lateral Resolution

The lateral resolution is dependent on the imaging optics, using a sample lens with a high numerical aperture will produce a small spot size improving the lateral resolution. For example, if we direct a Gaussian beam centred at λ through a lens with focal length f and fill the aperture d, a 2ω spot size is created where this is equivalent to the lateral resolution Δx of the OCT system, ω is half the beam diameter at the waist.

$$\Delta x = \frac{4 \cdot \lambda \cdot f}{\pi \cdot d} \tag{1.10}$$

Equation (2.18) calculates the theoretical lateral resolution using the system's optics parameters. However, in practical applications resolution test targets are used to measure lateral resolution. A common one is the USAF resolution target plates as shown below in figure 1.4. The target plates have groups of lines with the number of lines per millimetre known. The lateral resolution of the system is therefore taken as the smallest line pair the system can distinguish, according to the Rayleigh criterion.

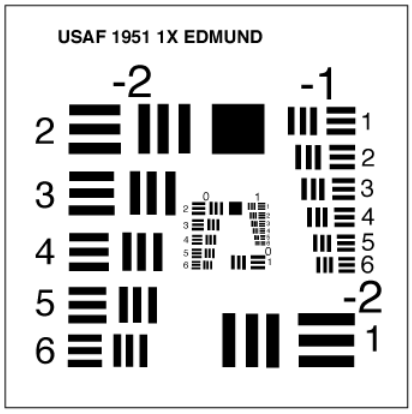

Figure 1.4: USAF resolution target [50]

Although using a high numerical aperture is desirable for an improved lateral resolution, it decreases the imaging depth. In our investigations where we are predominately interested in a superficial layer, the epithelium we can improve the lateral resolution at the expense of the imaging depth.

Axial Resolution

The axial resolution Δz is defined as half the coherence length of the light source. For a light beam with a Gaussian spectral profile, the coherence length l_c is related to the centre wavelength of the source λ_o and the bandwidth $\Delta\lambda$ as measured at the full width half maximum (FWHM).

$$l_c = \frac{4ln2}{n\pi}\frac{\lambda^2}{\Delta\lambda} \tag{1.11}$$

$$\Delta z = \frac{l_c}{2} \tag{1.12}$$

In practical measurements the axial resolution is measured by measuring the FWHM of the point spread function PSF. The PSF is calculated by Fourier transforming the interference recorded by the detector. In this measurement a plane mirror is used as

the sample for it's high reflectivity and low scattering properties.

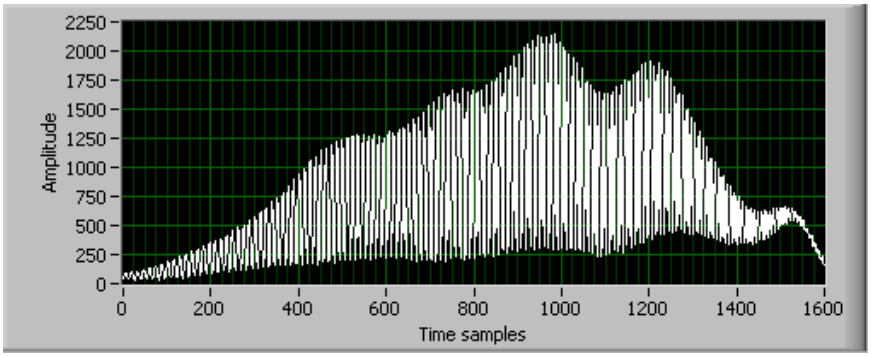

(a) Interference signal on top of the spectrum prior to reference subtraction been done

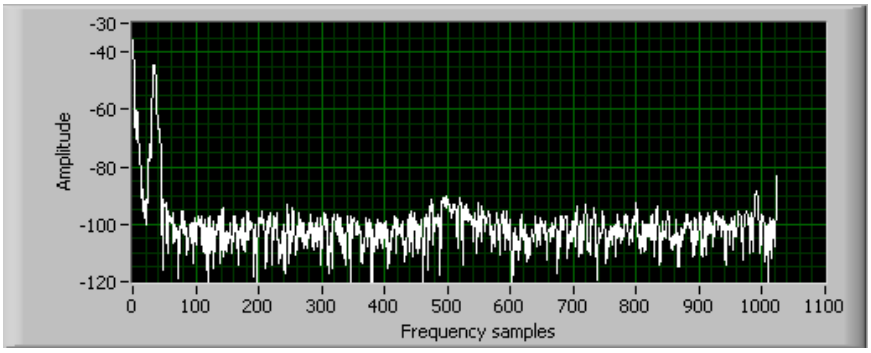

(b) The PSF near zero optical path difference/OPD

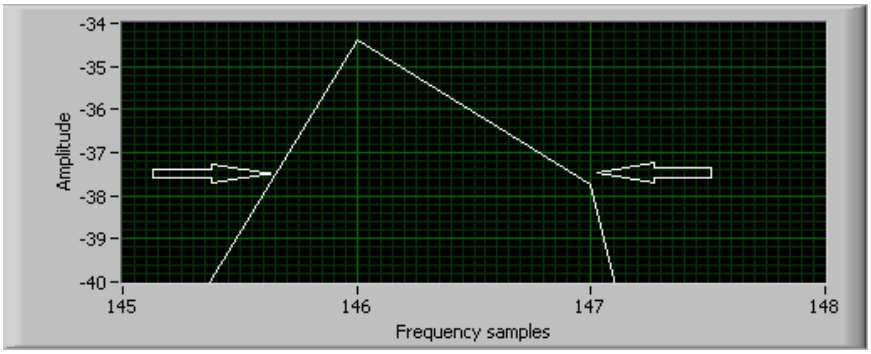

(c) The arrows showing where the axial resolution would be measured FWHM (-3dB)

Figure 1.5: The y axis is recording intensity in decibels and the x axis shows the number of pixels. These were recorded using a linescan CCD(EV71YEM1GE2014-BA9)

1.3.1 Sensitivity

The most common measurement of sensitivity is the signal to noise ratio (SNR). With SNR the recombined signal power is normalised by dividing it by the noise floor. This is convenient because it allows images to be compared even after brightness and contrast modifications.

The spectral domain set up used in our investigations provides an improvement in the SNR. Sensitivity in time domain is lower than that in the spectral domain by a factor of (N/2) where N is the number of pixels. The derivation is demonstrated below.

$$Sensitivity_{TDOCT} = 10 \log \frac{4 \cdot P_{sig} \cdot t \cdot \epsilon}{h \cdot \nu} \frac{2}{N} \tag{1.13}$$

$$P_{sig} = \int S_{sample} \, \mathrm{d}\omega \tag{1.14}$$

$$Sensitivity_{SDOCT} = 10 \log \frac{4 P_{sig} \cdot t \cdot \epsilon}{h \cdot \nu} \tag{1.15}$$

$$Sensitivity_{TDOCT} = Sensitivity_{SDOCT} - 10 \log \frac{N}{2} \tag{1.16}$$

where N = number of pixels, P_{sig} is the power returned from the sample arm, t is the acquisition time, ϵ is the quantum efficiency of the detector and $h\nu$ is the photon energy These formulas are derived in [51]. However, a more mathematically detailed description can be found by Leitgebs group [52].

1.3.1.1 Sensitivity Roll off

In our study sensitivity roll off is defined as how much the sensitivity fall with depth measured as dB/mm. With the aim of achieving high axial resolution in spectral domain OCT a broadband light source is used. The return light going onto the detector is dispersed into smaller wavelength 'packets' and each wavelength must

be detected to utilise the full power of the light source. The spectrometers used, however, have a fixed and limited number of pixels on the detector and hence has to bin wavelengths together. This has an averaging effect on the spectral waveform [51]. In Swept Source OCT (SSOCT) the light source outputs single frequencies per unit time, which is then detected by a photo-diode so this averaging effect is reduced, so the rate of sensitivity fall in SSOCT is much less than in SDOCT. Another reason why the sensitivity decreases with depth is because the finite resolution of the spectrometer reduces fringe visibility more significantly at high frequencies [53]. The rate at which sensitivity falls has been described below. The sinc function in equation (1.17) is from the Fourier transformation of the rectangular pixels and is multiplied by the Gaussian beam profile. The roll-off rate, R(z), after the Fourier transform of the interference signal is given as the product of a sinc function and the Gaussian function as shown below:

$$R(z) = \left(\frac{sin\ \xi}{\xi}\right)^2 exp\left[\frac{-\ w^2}{2ln2}\xi\right] \tag{1.17}$$

where

$$\xi = (\frac{\pi}{2})(\frac{z}{z_{max}})$$
$$z_{max} = \frac{\lambda^2}{4\Delta\lambda}$$
$$w = \frac{\delta\lambda}{\Delta\lambda}$$

where z_{max} is the maximum imaging depth, $\Delta\delta$ is the spectral resolution and $\Delta\lambda$ is the wavelength pixel spacing as proved by [51]. Figure 1.6 shows the theoretical SNR roll off for our OCT system with z_{max}=2.1 mm, λ=890 $\times$ 10^{-9}m, $\Delta\lambda$=150 $\times$ 10^{-9}m and w =1.58. A SNR roll off of 12.3 dB/mm is predicted.

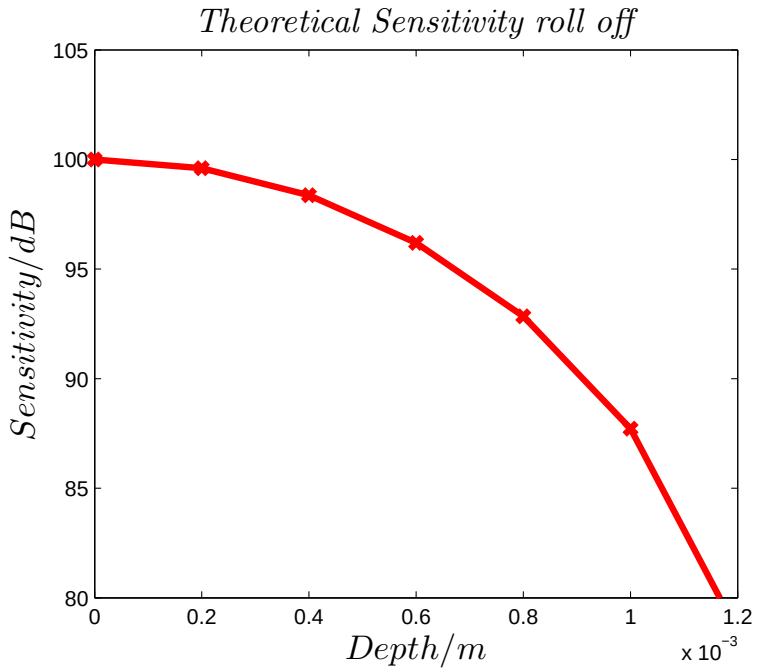

Figure 1.6: Sensitivity roll off calculated using system parameters

1.4 Magnetomotive OCT

In the project we propose to use magnetomotive OCT (MMOCT) to track the labelled limbal epithelium cells. In magnetomotive OCT we induce a shift or displacement in the spatial domain by the use of a magnetic field gradient. The sample under investigation is labelled with magnetic nanoparticles which can be functionalised with various groups. The magnetic particles used in the experiments are described in section 3.2. These particles are then actuated by the external magnetic field, usually the resultant displacement caused is too minute (order of nanometres) to be detected via structural OCT imaging, however phase resolved OCT can detect the resultant change in phase due to these displacement. The actuation of the nanoparticles causes small displacement changes in the cells' locations. Commonly the magnetic field gradient is usually generated by a solenoid. The solenoid can be constructed with an air core or with a metal with a high magnetic permeability such as iron or mild steel. Constructing the solenoid with a ferrite core increases the magnetic field strength but it concentrates the field around the core. Inserting a core allows the use of a lower current to achieve a desired magnetic field strength.

The labelled cells experience the greatest forces in the axial direction due to the orientation of the magnetic field lines, this is ideal for OCT since usually the axial resolution is higher than the lateral. MMOCTs can detect change in displacement either via amplitude modulation or phase modulation. In amplitude modulation a B scan is acquired with the magnetic field on and actuating the nanoparticles, this image is then compared to that of the same sample location but with the magnetic field off. A subtraction of the two images will lead to zero values at all the pixels in the image apart from the location of the nanoparticles because during the two images the location of the nanoparticles will be different [54]. Due to the need of imaging twice the technique is time expensive, it is possible to utilise phase modulation detection. In this scheme the nanoparticles are modulated at a set frequency, the image is then acquired and either a short time Fourier transform or wavelet transforms can be

applied to detect the location of that particular frequency [55].

1.4.1 Phase Stability

In phase resolved technique the phase stability of the OCT system is important as it sets the limit on the lowest phase change the system can detect. Phase stability is described as the standard deviation of the phase fluctuations usually of a plane mirror, since a plane mirror doesn't usually exhibit any phase fluctuations, any fluctuations detected can be attributed to the instabilities in the system.

Theoretically it can be calculated as below:

$$\delta\phi = \sqrt{\frac{1}{SNR}} \tag{1.18}$$

[56] where $SNR = 10^{(SNR(dB)/10)}$

For a given measured phase difference $\Delta\phi$, we can obtain the physical displacement using equation (1.22).

$$\Delta\phi = 2n\omega\Delta t \tag{1.19}$$

$$\Delta\phi = \frac{2n\pi c}{\lambda_o}\frac{\Delta z}{c} \tag{1.20}$$

$$\Delta\phi = \frac{4n\pi}{\lambda_o}\Delta z \tag{1.21}$$

$$\Delta z = \frac{\Delta\phi\lambda_o}{4n\pi} \tag{1.22}$$

where Δz is the change in displacement, λ_o is the centre wavelength and n is the refractive index, ω is the angular frequency.

References

[1] J. Krachmer, *Cornea*, vol. One. Elsevier Mosby, 2005.

[2] H. S. Dua, "Human corneal anatomy redefined : A novel pre-descemet's layer (dua's layer)," *Opthalmology*, 2013.

[3] M. J. Hogan, *Histology of the Human Eye*. Elsevier Health Sciences, 1971.

[4] D. Z. Reinstein, T. J. Archer, M. Gobbe, R. H. Silverman, and J. Coleman, "Epithelial thickness in the normal cornea: Three-dimensional display with artemis very high-frequency digital ultrasound," *Journal of Refractive Surgery*, vol. 24, pp. 571–581, 2008.

[5] J. H. Wang, D. Fonn, T. L. Simpson, L. Sorbara, R. Kort, and L. Jones, "Topographical thickness of the epithelium and total cornea after overnight wear of reverse-geometry rigid contact lenses for myopia reduction," *Investigative Ophthalmology & Visual Science*, vol. 44, pp. 4742–4746, 2003.

[6] S. Haque, L. Jones, and T. Simpson, "Thickness mapping of the cornea and epithelium using optical coherence tomography," *Optometry and vision science : official publication of the American Academy of Optometry*, vol. 85, pp. E963–76, 2008.

[7] Y. Feng and T. L. Simpson, "Corneal, limbal, and conjunctival epithelial thickness from optical coherence tomography," *Optometry and Vision Science*, vol. 85, pp. 880–883, 2008.

[8] R. C. Buck, "Cell migration in repair of mouse corneal epithelium.," *Investigative ophthalmology & visual science*, vol. 18, no. 8, pp. 767–784, 1979.

[9] T. Kuwabara, D. G. Perkins, and D. G. Cogan, "Sliding of the epithelium in experimental corneal wounds.," *Investigative Ophthalmology & Visual Science*, vol. 15, no. 1, pp. 4–14, 1976.

[10] H. S. Dua, V. A. Shanmuganathan, A. O. Powell-Richards, P. J. Tighe, and A. Joseph, "Limbal epithelial crypts: a novel anatomical structure and a putative limbal stem cell niche," *British Journal of Ophthalmology*, vol. 89, pp. 529–532, 2005.

[11] B. P. John R. W. Masters, *Human Adult Stem Cells*. Springer, 2009.

[12] R. Schofield, "The stem-cell system," *Biomedicine & Pharmacotherapy*, vol. 37, pp. 375–380, 1983.

[13] J. T. D. Genevieve A. Secker, *StemBook [Internet]*. Harvard Stem Cell Institute, 2008.

[14] C. Hanna and J. E. Obrien, "Cell production and migration in the epithelial layer of the cornea," *Archives of Ophthalmology*, vol. 64, pp. 536–539, 1960.

[15] A. Schermer, S. Galvin, and T.-T. Sun, "Differentiation-related expression of a major 64k corneal keratin in vivo and in culture suggests limbal location of corneal epithelial stem cells.," *The Journal of cell biology*, vol. 103, no. 1, pp. 49–62, 1986.

[16] F. E. Kruse, "Stem cells and corneal epithelial regeneration," *Eye*, vol. 8, no. 2, pp. 170–183, 1994.

[17] G. Cotsarelis, S.-Z. Cheng, G. Dong, T.-T. Sun, and R. M. Lavker, "Existence of slow-cycling limbal epithelial basal cells that can be preferentially stimulated to proliferate: implications on epithelial stem cells," *Cell*, vol. 57, no. 2, pp. 201–209, 1989.

[18] A. C. Romano, E. M. Espana, S. H. Yoo, M. T. Budak, J. M. Wolosin, and S. C. Tseng, "Different cell sizes in human limbal and central corneal basal epithelia measured by confocal microscopy and flow cytometry," *Investigative ophthalmology & visual science*, vol. 44, no. 12, pp. 5125–5129, 2003.

[19] J. Friedenwald, W. Buschke, and R. Scholz, "Effects of mustard and nitrogen mustard on mitotic and wound healing activities of the corneal epithelium.," *Bulletin of the Johns Hopkins Hospital*, vol. 82, no. 2, pp. 148–160, 1948.

[20] R. C. Buck, "Ultrastructure of conjunctival epithelium replacing corneal epithelium," *Current eye research*, vol. 5, no. 2, pp. 149–159, 1986.

[21] A. Pajoohesh-Ganji, S. Pal-Ghosh, G. Tadvalkar, and M. A. Stepp, "Corneal goblet cells and their niche: implications for corneal stem cell deficiency," *Stem cells*, vol. 30, no. 9, pp. 2032–2043, 2012.

[22] S. C. Tseng and M. Farazdaghi, "Reversal of conjunctival transdifferentiation by topical retinoic acid.," *Cornea*, vol. 7, no. 4, pp. 273–279, 1988.

[23] S. Ahmad, "Concise review: Limbal stem cell deficiency, dysfunction, and distress," *Stem Cells Translational Medicine*, vol. 1, pp. 110–115, 2012.

[24] K. Ramaesh, T. Ramaesh, G. N. Dutton, and B. Dhillon, "Evolving concepts on the pathogenic mechanisms of aniridia related keratopathy," *International Journal of Biochemistry & Cell Biology*, vol. 37, pp. 547–557, 2005.

[25] T. E. Clinch, K. M. Goins, and L. M. Cobo, "Treatment of contact lens-related ocular surface disorders with autologous conjunctival transplantation," *Ophthalmology*, vol. 99, pp. 634–638, 1992.

[26] J. Dart, "Impression cytology of the ocular surface - research tool or routine clinical investigation?," *British Journal of Ophthalmology*, vol. 81, pp. 930–930, 1997.

[27] V. Puangsricharern and S. C. G. Tseng, "Cytologic evidence of corneal diseases with limbal stem-cell deficiency," *Ophthalmology*, vol. 102, pp. 1476–1485, 1995.

[28] K. R. Kenyon and S. C. G. Tseng, "Limbal autograft transplantation for ocular surface disorders," *Ophthalmology*, vol. 96, pp. 709–723, 1989.

[29] G. Pellegrini, C. E. Traverso, A. T. Franzi, M. Zingirian, R. Cancedda, and M. DeLuca, "Long-term restoration of damaged corneal surfaces with autologous cultivated corneal epithelium," *Lancet*, vol. 349, pp. 990–993, 1997.

[30] M. S. Santos, J. A. P. Gomes, A. L. Hofling-Lima, L. V. Rizzo, A. C. Romano, and R. Belfort, "Survival analysis of conjunctival limbal grafts and amniotic membrane transplantation in eyes with total limbal stem cell deficiency," *American Journal of Ophthalmology*, vol. 140, pp. 223–230, 2005.

[31] M. Fernandes, M. S. Sridhar, V. S. Sangwan, and G. N. Rao, "Amniotic membrane transplantation for ocular surface reconstruction," *Cornea*, vol. 24, pp. 643–653, 2005.

[32] J. A. P. Gomes, A. Romano, M. S. Santos, and H. S. Dua, "Amniotic membrane use in ophthalmology," *Current opinion in ophthalmology*, vol. 16, pp. 233–40, 2005.

[33] C. Akle, I. McColl, M. Dean, M. Adinolfi, S. Brown, A. H. Fensom, J. Marsh, and K. Welsh, "Transplantation of amniotic epithelial membranes in patients with mucopolysaccharidoses," *Experimental and Clinical Immunogenetics*, vol. 2, pp. 43–48, 1985.

[34] C. A. Akle, K. I. Welsh, M. Adinolfi, and S. Leibowitz, "Immunogenicity of human amniotic epithelial-cells after transplantation into volunteers," *Lancet*, vol. 2, pp. 1003–1005, 1981.

[35] G. M. Tosi, M. Massaro-Giordano, A. Caporossi, and P. Toti, "Amniotic membrane transplantation in ocular surface disorders," *Journal of Cellular Physiology*, vol. 202, pp. 849–851, 2005.

[36] C. Jenkins, S. Tuft, C. Liu, and R. Buckley, "Limbal transplantation in the management of chronic contact-lens-associated epitheliopathy," *Eye*, vol. 7, pp. 629–

633, 1993.

[37] N. Koizumi, T. Inatomi, T. Suzuki, C. Sotozono, and S. Kinoshita, "Cultivated corneal epithelial stem cell transplantation in ocular surface disorders," *Ophthalmology*, vol. 108, pp. 1569–1574, 2001.

[38] A. Fatima, V. S. Saingwan, G. Iftekhar, P. Reddy, H. Matallia, D. Balasubramanian, and G. K. Vemuganti, "Technique of cultivating limbal derived corneal epithelium on human amniotic membrane for clinical transplantation," *Journal of Postgraduate Medicine*, vol. 52, pp. 257–261, 2006.

[39] C. Osei-Bempong, C. Henein, and S. Ahmad, "Culture conditions for primary human limbal epithelial cells," *Regenerative Medicine*, vol. 4, pp. 461–470, 2009.

[40] P. Deshpande, C. Ramachandran, F. Sefat, I. Mariappan, C. Johnson, R. McKean, M. Hannah, V. S. Sangwan, F. Claeyssens, A. J. Ryan, and S. MacNeil, "Simplifying corneal surface regeneration using a biodegradable synthetic membrane and limbal tissue explants," *Biomaterials*, vol. 34, pp. 5088–5106, 2013.

[41] S. I. Brown, M. P. Tragakis, and D. B. Pearce, "Corneal transplantation for severe alkali burns," *Transactions - American Academy of Ophthalmology and Otolaryngology. American Academy of Ophthalmology and Otolaryngology*, vol. 76, pp. 1266–74, 1972.

[42] V. S. Sangwan, S. Basu, G. K. Vemuganti, K. Sejpal, S. V. Subramaniam, S. Bandyopadhyay, S. Krishnaiah, S. Gaddipati, S. Tiwari, and D. Balasubramanian, "Clinical outcomes of xeno-free autologous cultivated limbal epithelial transplantation: a 10-year study," *British Journal of Ophthalmology*, vol. 95, pp. 1525–1529, 2011.

[43] P. Rama, S. Matuska, G. Paganoni, A. Spinelli, M. De Luca, and G. Pellegrini, "Limbal stem-cell therapy and long-term corneal regeneration," *Human Gene Therapy*, vol. 22, pp. A8–A8, 2011.

[44] A. F. Fercher, "Optical coherence tomography - development, principles, applications zeitschrift fur medizinische physik," *Zeitschrift fur medizinische Physik.*, 2010.

[45] D. Huang, E. A. Swanson, C. P. Lin, J. S. Schuman, W. G. Stinson, W. Chang, M. R. Hee, T. Flotte, K. Gregory, C. A. Puliafito, and J. G. Fujimoto, "Optical coherence tomography," *Science*, vol. 254, pp. 1178–1181, 1991.

[46] P. H. Tomlins and R. K. Wang, "Theory, developments and applications of optical coherence tomography," *Journal of Physics D-Applied Physics*, vol. 38, pp. 2519–2535, 2005.

[47] A. Dobroiu, H. Sakai, H. Ootaki, M. Sato, and N. Tanno, "Coaxial mirau interferometer," *Optics Letters*, vol. 27, pp. 1153–1155, 2002.

[48] P. Casaubieilh, H. D. Ford, and R. P. Tatam, "Optical fibre coherence tomography based on fizeau interferometer configurations," vol. 5486, (Cranfield Univ, Silsoe, ENGLAND), pp. 112–122, 2003.

[49] S. J. Matcher, "Practical aspects of oct imaging in tissue engineering," *3d Cell Culture: Methods and Protocols*, vol. 695, pp. 261–280, 2011.

[50]

[51] S.-W. Lee, H.-W. Jeong, B.-M. Kim, Y.-C. Ahn, W. Jung, and Z. Chen, "Optimization for axial resolution, depth range, and sensitivity of spectral domain optical coherence tomography at 1.3 mu m," *Journal of the Korean Physical Society*, vol. 55, pp. 2354–2360, 2009.

[52] R. Leitgeb, C. K. Hitzenberger, and A. F. Fercher, "Performance of fourier domain vs. time domain optical coherence tomography," *Optics Express*, vol. 11, pp. 889–894, 2003.

[53] S. Yun, G. Tearney, B. Bouma, B. Park, and J. de Boer, "High-speed spectral-domain optical coherence tomography at 1.3 μm wavelength," *Optics Express*, vol. 11, no. 26, pp. 3598–3604, 2003.

[54] A. Oldenburg, F. Toublan, K. Suslick, A. Wei, and S. Boppart, "Magnetomotive contrast for in vivo optical coherence tomography," *Optics Express*, vol. 13, no. 17, p. 6597, 2005.

[55] A. L. Oldenburg, V. Crecea, S. A. Rinne, and S. A. Boppart, "Phase-resolved magnetomotive oct for imaging nanomolar concentrations of magnetic nanoparticles in tissues," *Optics Express*, vol. 16, pp. 11525–11539, 2008.

[56] M. A. Choma, A. K. Ellerbee, C. H. Yang, T. L. Creazzo, and J. A. Izatt, "Spectral-domain phase microscopy," *Optics Letters*, vol. 30, pp. 1162–1164, 2005.

Chapter 2

Ultra High Resolution Spectral Domain OCT (UHR-SDOCT) for corneal imaging

2.1 Summary

In this chapter, we discuss optical coherence tomography, the theory and how the system used in our study was constructed. Properties such as axial and lateral resolution along with sensitivity and depth roll off are also discussed. The methods for measuring the properties are also discussed. The measured parameters are compared to the theoretically calculated values.

2.2 Introduction

This chapter discusses the construction of the Ultrahigh Resolution Spectral Domain Optical Coherence Tomography system (UHRSDOCT) which throughout the thesis

will be referred to as OCT system and the Magnetomotive OCT (MMOCT). The UHRSDOCT was used for imaging oral mucosal tissue, rabbit cornea and then extended and adapted to perform as a Magnetomotive OCT (MMOCT). The MMOCT was used to locate labelled cells while the UHR-SDOCT was used to produce high resolution images of the corneal epithelium to help with the visualisation of the limbus. For these requirements the system needs not only high resolution but also good phase stability to allow the locating and tracking of the labelled stem cells using the MMOCT.

The system is fibre based and built on a Michelson interferometer configuration. A 50/50 fibre coupler is used to split the source beam and also to recombine the scattered and reflected beams from the reference and sample arm. Most components of the system are caged to increase the phase stability which is essential for making accurate displacement measurements. The whole system was then placed on vibration absorbing rubber.

Spectral domain OCT systems require no reference arm scanning for it's image formation, this reduces the image acquisition time. Spectral Domain OCT (SDOCT) has an increased efficiency due to the use of a spectrometer to detect the interference signal in the detector arm [1]. The spectrometer increases the sensitivity of the system. A sensitivity increase of 21.7dB compared to the time domain OCT has been published [2] [3]. In the spectral domain OCT, the detected spectral interference is recorded in terms of wavelength to allow for the retrieval of sample depth information, the spectral interference data is re-sampled into evenly spaced wave numbers and Fourier transformed into the spatial domain to retrieve the depth information of the sample.

2.3 Experimental Setup

2.3.1 Light Source

In building an ultra-high resolution OCT system the choice of light source is critical. A common choice is the Super-Luminescent diode (SLDs). These can be fabricated to produce a variety of spectra with different combinations of central wavelengths and bandwidths whilst giving a usable output power (>3mW). A dual SLD (Broadlighter D890-HP, Superlumdiodes Ltd) with centre wavelength $\lambda_o = 890$ nm and a bandwidth $\Delta\lambda = 150$ nm was used. Figure 2.1 shows the spectrum of the light source recorded using an optical spectrum analyser. The source emits partially polarized light with a nominal power of 4.9 mW. The theoretical axial resolution of the system is determined by the central wavelength and bandwidth of the light source.

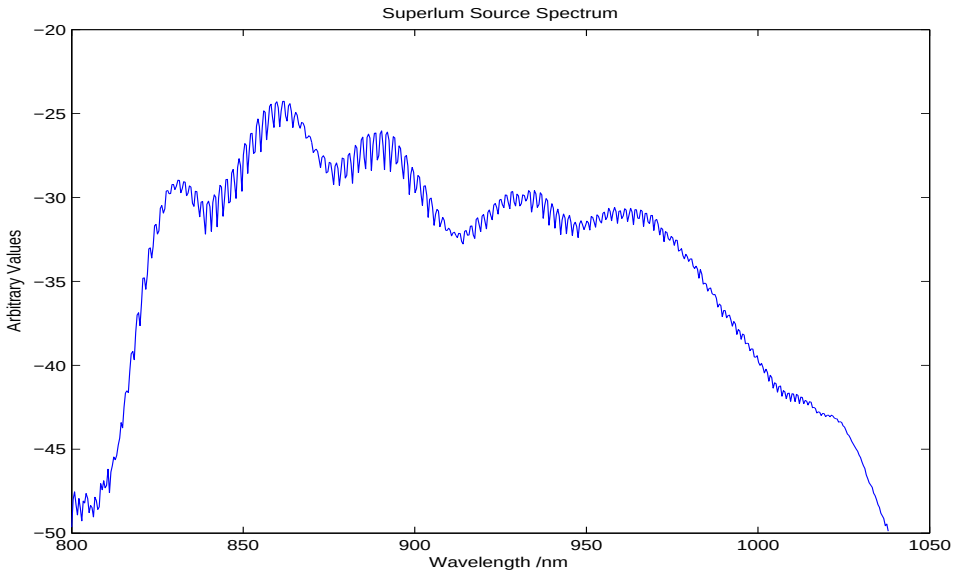

Figure 2.1: Spectrum of Light Source measured using Spectrum Analyser with both SLDs on. The presence of the ripples are due to internal reflection in the SLD

An optical isolator (OFR IO-SLD150-895 APC) was used to reduce the power of light reflected from the interferometer set-up back into the source. The trade off

for this safety feature is the reduction in the power of the light beam entering the interferometer. A reduction of source power by 0.1 dB was measured.

Figure 2.2 is a schematic drawing of the Ultrahigh resolution OCT system and a photograph is attached in the appendix.

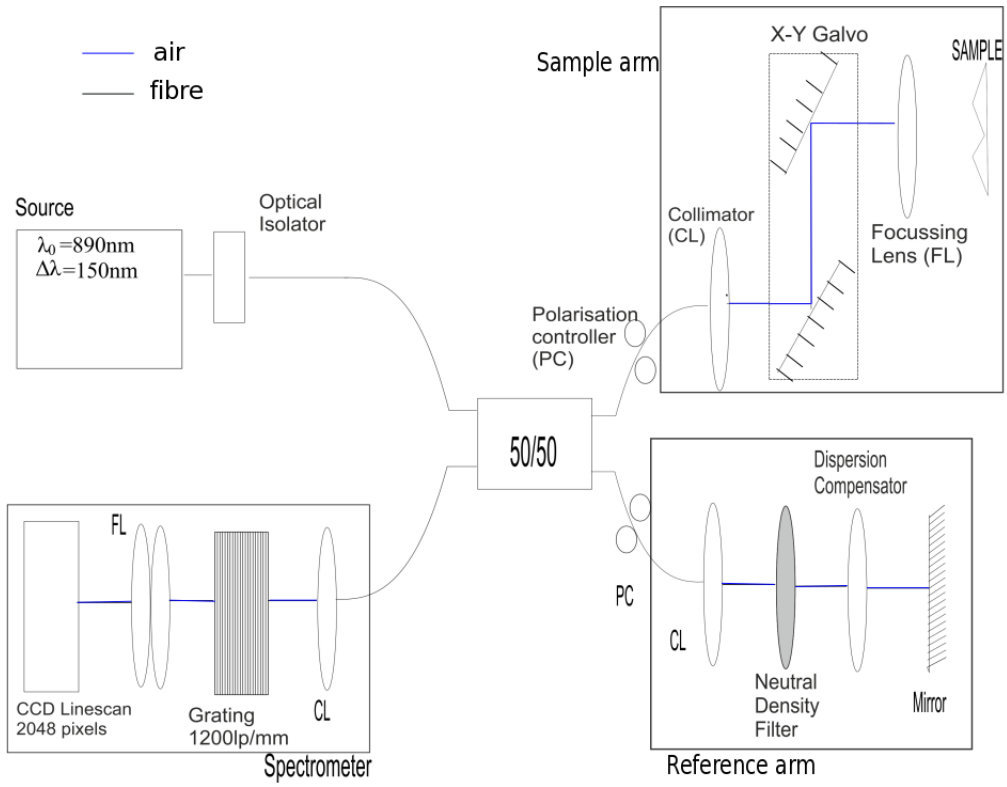

Figure 2.2: Spectral Domain OCT Experimental Set-up

2.3.2 Optical Fibre and Coupler

The system is fibre based, the fibre used throughout most of the system was Nufern 630-HP.The single mode fibre has a core diameter of 3.5μm, a core numerical aperture of 0.130 and a cladding diameter of 125.0$\pm$1.0μm. A 2$\times$2 fibre coupler (Gould Optics) with a 50/50 splitting ratio and a 3 dB insertion ratio was used to split the source beam into the reference and sample beams figure 2.2.

2.3.3 Sample arm component

The sample to be imaged is placed at the end of the sample arm. During alignment and calibration, a plane mirror is used as a sample due to it's high reflectivity. Therefore, a higher proportion of the light is reflected into the detector. The galvanometer system(Thorlabs, GVS002) allows for the lateral scanning of the sample to provide B scans (2D images). The galvanometer system has a pair of galvanometer scanners (TSH 22556-Y and TSH 22555-X) and this allows the system to acquire volumetric images. The scanners are powered via a National Instrument DAQ board which is controlled using a bespoke LabView software. A telecentric scanning lens (Thorlabs, LSM02-BB) with an effective focal length of 17.93 mm, $\times$10magnification and spot size of 9 μm (these values are quoted for beam with centre wavelength of 850 nm) giving a numerical aperture of 0.11.

Initially the sample plate (holds the sample or plane mirror during alignment) had 2 thumbscrews for adjustment however this gave low amounts of returned light to the detector. The two screw adjustment plate was changed for a plate with three adjustment screws. A 3% increase in the sample arm return power is achieved with the three point adjustable screws. Optimising the sample arm return power(P_s) is of great importance because the maximization of this power will improve the SNR of the system.

$$SNR = 10log\frac{4P_s t\epsilon}{h\nu} \tag{2.1}$$

Equation (2.1) as stated in [3] defines the shot noise limited signal to noise ratio (SNR) or the optical dynamic range in terms of P_s the fractional power reflected by the sample arm, t the exposure (signal collection time), ϵ the detector quantum efficiency and $h\nu$ the photon energy.

2.3.4 Reference arm components

In the reference arm the light beam emitted from the coupler is reflected by a plane mirror. A dispersion compensator (Thorlabs, LSM02DC) was placed in the path of the beam after the collimator so that the beam travels through the same length of material, in this case glass, in both the reference and the sample arm. The dispersion compensator has an identical refractive index and thickness as the focusing lens in the sample arm. Without the compensator the axial resolution degrades due to extra chromatic dispersion experience by the sample beam relative to the reference beam. Also a variable neutral density filter was needed to attenuate the signal from the reference arm, without this attenuation the reference signal (0.28 mW) would saturate the CCD.

2.3.5 Detector arm components

Light from the sample and reference arms are recombined by the coupler and travels into the detector arm. The detector arm is composed of an in house built spectrometer. The light emitted from the coupler fibre tip passes through a collimating lens. This serves as a beam expander to increase the illumination spot size on the diffraction grating. The diffraction grating of the spectrometer was changed from reflective to a transmission grating with 820 lp/mm to a transmission grating (Wasatch Photonics) with 1200 lp/mm. The increased lp/mm increases the angle of dispersion and hence from a fixed distance away the transmission grating model would disperse the spectrum across larger number of the CCD pixels and therefore give a better spectral resolution. The improved spectral resolution will increase the imaging depth [4] [5].

The CCD camera used in the experimentations that follows is the Aviiva EV71YEM1GE2014-

BA9. It is a line scan camera with 2048 rectangular pixels with dimension 14μm $\times$ 28μm. The photon counts and exposure time has a linear relationship as seen in figure 2.3. This is expected because the longer the CCD spends collecting photons the higher the photon count will be. However, for the gain the photon counts increases in steps. With light incident on the CCD pixels, there is no change in intensity recorded by changing the gain, the gain has to be increase from the lowest -24dB to -21dB before an increase in number of intensity is seen and then increased to a gain of -15 dB to see another increase. The count dependency on gain is not linear figure 2.4. The gain setting changes the conversion ratio in the pre amplifier before the signal enters the analogue to digital converter (ADC). A higher gain gives a higher output voltage for the fixed photon flux on the CCD pixels. Therefore, a lower photon flux is needed to saturate the output of the ADC.

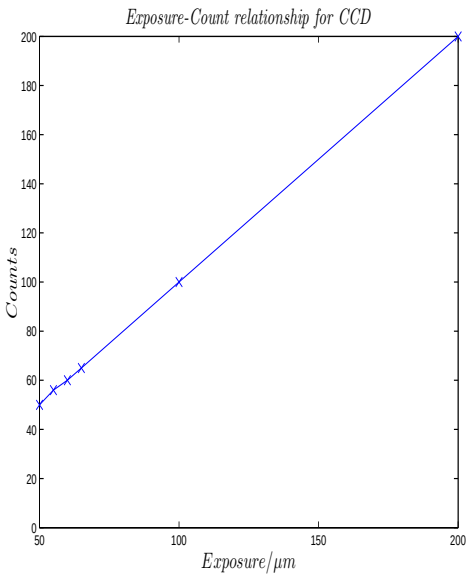

Figure 2.3: Photon counts increases with exposure time

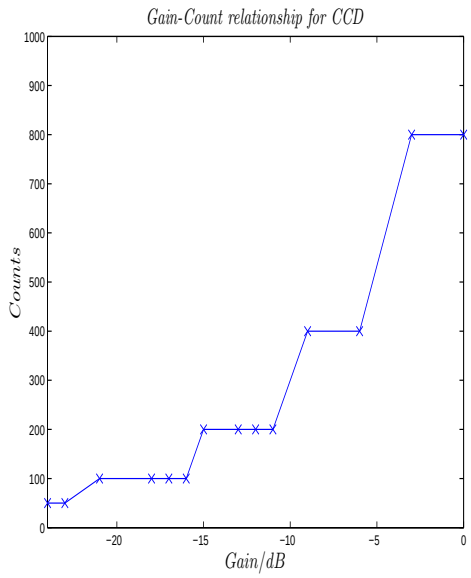

Figure 2.4: Photon counts showing increment in steps for increasing gain

The optimal gain setting was found to be -12 dB for the shortest exposure time of 50 μs. Increasing the gain above -12 dB increases the noise by the same amount as the signal so there is no overall benefit. From equation (2.1) we see that by increasing the exposure time increases the SNR but this increases the time needed to acquire the image. With the project being aimed for clinical implementation the lowest exposure

time was used. Even with the lower exposure time the SNR achieved (95 dB) is comparable to the systems of some of the leading groups in the field.

There is a maximum power limit before the CCD saturates. The CCD saturation level is dependent on its full well capacity; the maximum number of electrons each pixel can hold. Any excess electrons may be leaked into neighbouring pixels causing saturation.

The optical power required to saturate the CCD charge wells can be calculated from the manufacturer's data as follows.

$$\textit{Full well capacity per pixel} = 312500 \ \textit{electrons} \tag{2.2}$$

$$\textit{Full well capacity for array} = 312500 \times 2048 \tag{2.3}$$

$$= 640 \times 10^6 \ \textit{electrons} \tag{2.4}$$

$$\textit{Full well energy} = \textit{Full well capacity} \times h \times f \tag{2.5}$$

$$\textit{Full well energy (Saturation Energy)} = \tag{2.6}$$

$$(640 \times 10^6) \times 6.63 \times 10^{-34} \times \left(\frac{3 \times 10^8}{890 \times 10^{-9}}\right) \tag{2.7}$$

$$= 1.43 \times 10^{-10} J$$

$$\textit{Saturation Power} = \frac{\textit{Saturation Energy}}{\textit{Exposure time}} \tag{2.8}$$

$$= \left(\frac{1.43 \times 10^{-10}}{50 \times 10^{-6}}\right) \tag{2.9}$$

$$= 2.86 \mu W$$

$$\textit{Saturation power per pixel} = 2.86 \mu W / 2048 \tag{2.10}$$

$$= 1.40 nW \tag{2.11}$$

$$\tag{2.12}$$

If the power falling onto the CCD is larger than 2.86 μW then we get saturation. The ADC output could also be saturated depending on the Gain.

2.3.6 Spectrometer components

Equation (2.13) gives the angular dispersion ($\delta\theta$) of a beam passing through a grating. For our set-up the diffraction order (m) is 1. To increase the angular dispersion, the line spacing(d) must be decreased. So the 1200 lp/mm will have a larger angular dispersion and hence the spectrum will cover a larger number of pixels improving the spectral resolution.

$$Angular\ \ dispersion: \frac{\delta\theta}{\delta\lambda} = \frac{m}{dcos\theta} \tag{2.13}$$

The smallest separation between two wavelengths which the grating can resolve is known as the resolving power

$$ResolvingPower = mN = \frac{\lambda}{\delta\lambda} \tag{2.14}$$

where m is the order of diffraction which is 1 for our system, d is the separation between adjacent slits (inverse of number of grooves) and N= total number of grooves illuminated on grating.

The collimated beam entering the detector arm has a diameter of 5 mm. This beam is incident on the diffraction grating. Using the transmission grating gives a resolving power of 6000 using equation (2.14). The transmission grating (1200 lp/mm) gives a central spectral resolution of 890 nm/6000=0.15nm.The resolution will be slightly better at the lower wavelength 815 nm (0.14 nm) and slightly higher resolution at the higher wavelength 965 nm (0.16 nm).

The diffracted beam exiting the grating needs to be focused onto the CCD pixels. The lenses in the spectrometer focuses the diffracted spectrum from the grating onto the CCD pixels. The source has a bandwidth of $150nm$ this needs to fit onto the 2048

pixels which has a combined length (l) of 28.67mm (2048 $\times$ 14μm). To achieve a spectral resolution of 0.15 nm and detect the full 150 nm bandwidth, the least number of pixels needed is $\frac{150nm}{0.15nm}$= 1000 pixels. The CCD used, has twice this amount of pixels. However, for the FFT and resampling only 1600 pixels are used since the interference covers only this number of pixels. The light beam is incident on the diffraction grating at an angle of 35^o. This gives a centre wavelength diffraction angle of $-29.63°$. The lowest wavelength (815nm) has diffraction angle of $-23.85°$ and the highest wavelength (965nm) has a diffraction angle of $-35.76°$. Therefore, the spectral range 815-965 nm is dispersed at $-29.63 \pm 6.5°$. The angular spread ($\Delta\theta$) is 13°.

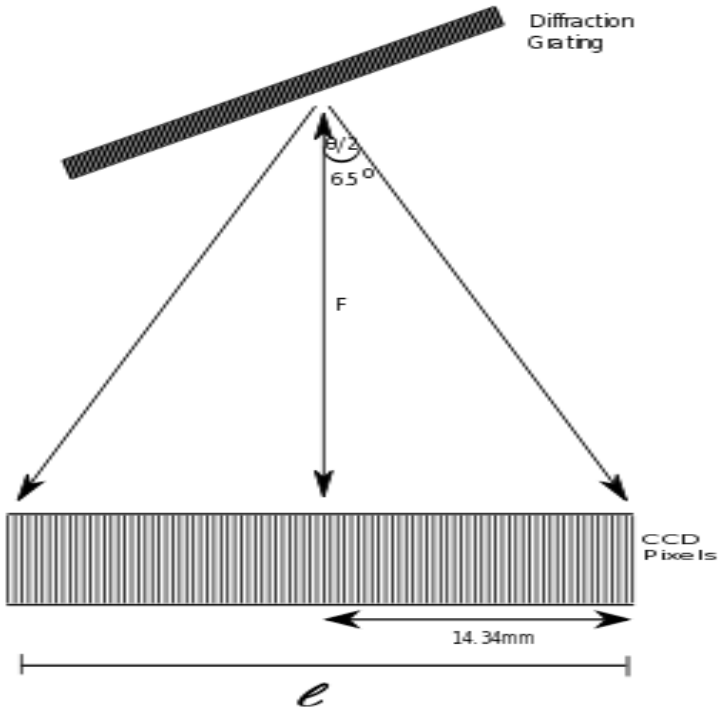

Figure 2.5: Shows dispersion angle onto the pixel array

The focal length of the optics is given by:

$$F = \frac{l}{2} \div \tan\left(\frac{\Delta\theta}{2}\right) \tag{2.15}$$

$$F = \frac{28.67}{2} \div \tan(6.5^{\circ}) \tag{2.16}$$

$$F = 125.86mm$$

Initially 3 identical focusing lenses (total focal length =75 mm) were used in the spectrometer, one followed by the other. Each lens has a focal length of 200 mm. The number of focusing lens was changed to 2 instead with an effective focal length= 100 mm.

The 2 lenses give a much closer focal length to the calculated equation (2.15) than the 3 lens combination. The excess 25.86 mm from equation (2.15) was achieved by the use of micrometer stage to move the camera towards the lenses. The larger 100mm focal plane length allows the spectrum to be dispersed over a larger number of pixels. The spectrum covering a larger number of pixels will improve the spectral resolution and the sensitivity roll off with depth. The sensitivity roll off with depth is dependent on the optical resolution limit of the spectrometer and the pixel width [3].

2.4 Matching Path Length

To obtain constructive interference between the sample (a mirror during alignment) and the reference mirror the optical path lengths of both arms must be matched so the zero path difference occurs conveniently close to the tissue surface. The length of fibre in each arm is measured taking into account, alongside the refractive index of the fibre (glass, n_{glass}=1.47) the air gaps. The sensitivity of the detector depends on the sample return power equation (2.1), so the first the sample mirror is moved to the focal plane of the sample arm focusing lens for the maximum return power and then the reference arm mirror is moved to a position to equal the length of the sample arm. At the point of zero path length difference the point spread function has the highest amplitude and narrowest width.

2.5 Imaging Parameters

2.5.1 Axial Resolution

An advantage of OCT is that the axial and lateral resolutions of the system are independent of each other. The axial resolution is dependent on the source used and the lateral is defined by the optics. The axial resolution (Δz) is described as half the coherence length of the source:

$$\Delta(z) = \frac{2ln2}{n\pi}\frac{\lambda^2}{\Delta\lambda} \tag{2.17}$$

Where λ is the central wavelength, $\Delta\lambda$ is the spectral bandwidth of the light source and n is the refractive index of the sample medium.

The source being used has a theoretical axial resolution of 2.3 μm in air. However due to the camera's wavelength dependent responsitivity an axial resolution of 2.5 μm was achieved. The success of the project is tied to the axial resolution. The higher the resolution the more probable it is that the corneal cells may be identified and the corneal layers differentiated.

The axial resolution can be measured from the full width half maximum of the point spread function(PSF). The PSF is found by Fourier transforming the interference signal.

When the sample path length is matched to the reference arm path length within the coherence length of spectral channel we get interference. Figure 2.6a shows the interference recorded using all 2048 pixels of the CCD camera. However, the interference does not cover all the pixels but approximately 1600 pixels. So these 1600 pixels were selected to be used in the re-sampling and Fourier transformation after the reference power is subtracted Figure 2.6b. The reference power is subtracted by blocking the

sample arm and recoding the reference power, spectrum is then saved and subtracted from the interference spectrum.

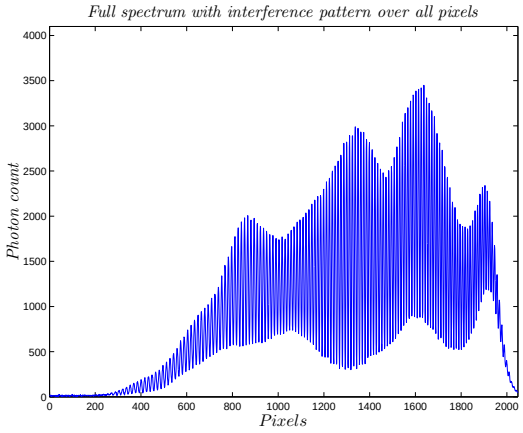

(a) Interference between sample and reference arm detected with 2048 pixels

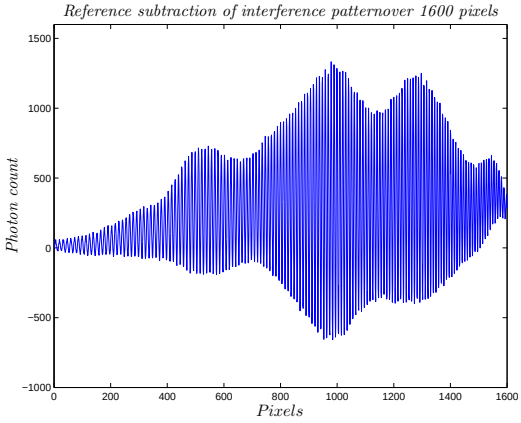

(b) Interference used for re-sampling captured by 1600 pixels after reference subtraction

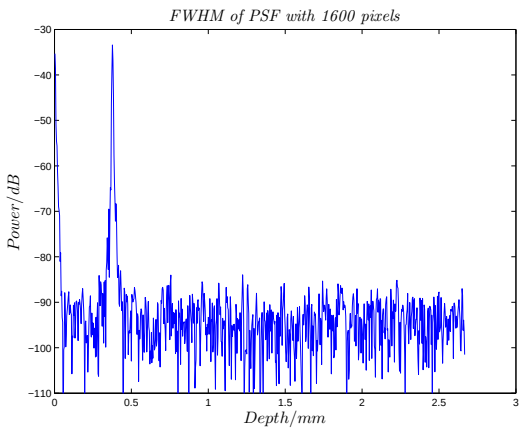

(c) PSF from 1600 pixels interference after re-sampling

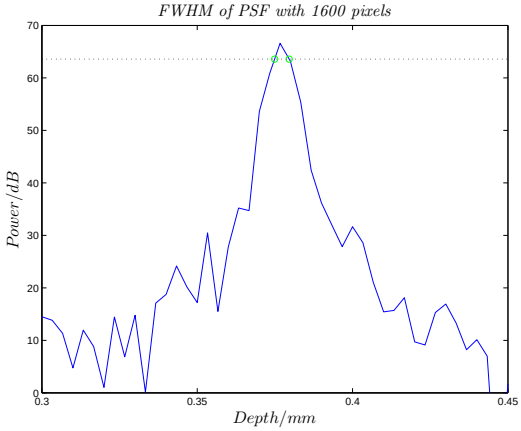

(d) Point Spread function using 1600 pixels re-sampling. The green circle markers mark the FWHM position

Figure 2.6: Stages in measuring axial resolution

For the re-sampling, 1600 pixels were used from pixel 350 to 1950. In figure 2.6b the reference power has been subtracted so the remaining signal should be a cosine modulation. The cosine should be centred around zero because usually the reference power is much greater than the sample arm power. However, in the set-up the sample

power is similar to the reference power so there is still some DC component on the interference even after the reference subtraction.

The PSF is obtained by Fourier transforming the interference and taking the squared modulus. This gives the power spectrum against depth. The axial resolution was measured to be 2.5±0.3 μm in air, this is lower than the theoretical 2.3 μm. The difference is most likely due to the chromatic dispersion and the optics not been perfectly aligned. Figure 2.6c shows the PSF at for mirror position 400 μm from zero path difference. In Figure 2.6 shows the points used to measure the axial resolution in green.

After the beam is dispersed onto the CCD, the recorded spectrum is linear in wavelength but needs to be re-sampled to be linear in wave number. The re-sampled spectrum is Fourier transformed. Without re-sampling the PSF is very broad and gives large axial resolutions and also the axial resolution deteriorates rapidly with depth. The resampling was done using the zero crossing technique. A LabView program was written to carry out this process. The LabView script was written by Dr. Zenghai Lu, based on code supplied with a commercial swept-source OCT system (EX 1301, Michelson Diagnostics Ltd). This technique works by finding the points where the cosine modulations cross the zero point. Assuming that these points should be periodic, it can be used to re-sample the interference signal in wave number.

2.5.2 Lateral Resolution

The lateral resolution (Δx) is dependent on the geometric parameters of the sample arm focssing optics.

$$\Delta x = \frac{4\lambda f}{\pi d} \tag{2.18}$$

Where f and d are the focal length and d is spot size of the focusing lens. The lens has a focal length of 17.95 mm and a spot size diameter of 4 mm so a lateral resolution of 5 μm is the optimum.

The resolution of each group and element on USAF resolution target was calculated as follows:

$$Resolution(lp/mm) = 2^{(group+((element-1)/6)} \tag{2.19}$$

$$Resolution(mm) = \frac{1}{2 \times lp/mm} \tag{2.20}$$

The lateral resolution was measured using a resolution targets. The resolution target (Edmund Optics, 1951 USAF) is a glass plate with chrome patterned lines. The lines are sectioned into groups and elements. Each group has 6 elements and each element has 3 lines (no chrome) and 2 lines with chrome. The lines have equal widths. The widths of the lines decrease with increasing group numbers (-2 to 7), in each group the width of the lines decreases with increasing element number. The lateral resolution is defined by the smallest lines resolvable. An en face image figure 2.7 was acquired of the resolution target and the smallest element which was resolvable was group 6 element 3 which equates to a lateral resolution of 6.20 μm.

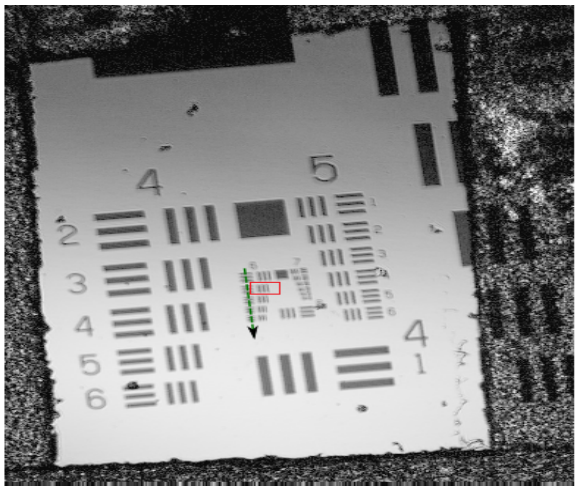

Figure 2.7: Enface image of USAF resolution target taken using the SDOCT. Group 6 element 3 is the smallest resolvable element

A gray scale profile showing the gray scale levels across the whole of group 6 following the green dashed arrow on figure 2.7. Figure 2.8 is the gray scale profile of group 6. From the profile it is evident that the last resolvable element is 3. Each element should have two peaks representing the bright regions on the USAF resolution target. The red dashed line on the profile plot are placed at the beginning of element 2, the boundary between elements 2/3 and at the end of element 3. The peaks within element 2 and 3 are resolvable.

The peaks in elements have contrast greater than 50% whilst the higher elements have contrast levels lower than this.

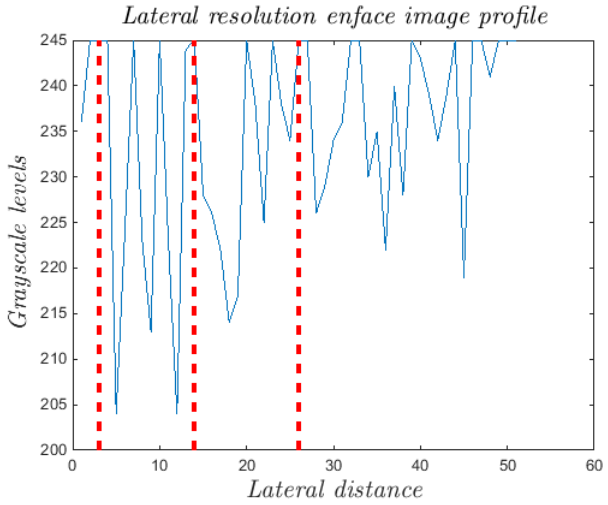

Figure 2.8: Gray scale profile plot of enface image of USAF resolution target. Red dashed lines show boundaries of elements 2 and 3

2.5.3 Sensitivity

The sensitivity is defined as the minimum reflected signal detectable from a sample. It can also be looked at as the difference between the signal and noise variance. The sensitivity is normally defined numerically as a decibel ratio of the signal power to the noise (SNR) power ($20log(\frac{P_{signal}}{P_{noise}})$). The are three main sources of noise in OCT systems shot noise, Relative Intensity Noise(RIN) and detector noise. The shot noise arises from the random arrival of photons in the sample signal. The RIN is produced by instabilities in the light source and finally the detector noise is due to thermal fluctuations in the detector, ADC quantization noise etc. Ideally the OCT system should be shot noise limited.

2.5.3.1 Method

Initially the point of of zero path difference needed to be found and the back reflected signals in the sample and reference arms need to be maximised. This will increase the amplitudes of the interferences since the SNR is mainly dependent on the sample return power equation (2.1). The sample arm is moved into a position where the

maximum return power is achieved and then the reference mirror moved until the paths in the arms are equal. In the sample arm a focusing lens is used to focus the beam onto the sample. Therefore, the mirror (used as a sample) has to be placed onto the stage and adjusted in the depth direction until the surface of the mirror is at the focal plane of the focusing lens. Once at the focal plane the angle of the sample was adjusted using the thumb-screws underneath the sample. These were adjusted to give a maximum sample return power. This power also saturates the CCD therefore a pair of neutral density filters with attenuation of 40 dB were used in the sample arm to reduce the sample return power. At the focus plane the sample return power is highest. In the reference arm the mirror is adjusted to back reflect the most light into the coupler. The returned reference arm power exceeded the saturation limit of the CCD detector, so had to be attenuated with a wheel neutral density filter. The SNR can also be increased by adjusting the polarisation controls in the sample and reference arms to place both arms in the same polarisation state to ensure maximum interference. Once the reference and sample return powers have been maximised the camera position can be adjusted in the pitch, yaw, x y and z directions to allow all the diffracted beam to fall onto the camera pixels. Finally, with the beam falling onto the CCD pixels the interference signal can be used to resample the interference signal from wavelength to wavevector and then Fourier transformed to give a PSF with sensitivity of 95 dB.

2.5.4 Sensitivity roll off with depth

As the path difference changes increases from zero i.e. the depth being probed increases the signal being detected decreases. This decrease of sensitivity is described as the sensitivity roll off. The sensitivity roll off gives the usable imaging depth, since if the sensitivity falls too low approximately below 80dB the image appears dark and difficult to image biological samples.

In OCT, images are produced using coherence interferometry unlike other sub micron imaging modalities which may use confocal gating. In coherence interferometry, the maximum signal is detected when the path lengths in the arms of the interferometer are equal. As the path length difference becomes non zero the signal decreases. If the path length difference is larger than the coherence length of the light source the signal falls rapidly. This path length condition means that OCT can reject background noises which are incoherent. In the confocal gated modalities, the signal strength and background noise rejection is achieved through the use of lens combinations and a pin hole. The lens combination used in these modalities for example in the confocal microscopy means the laser beam is focused on a single sample plane. The pin hole plane is the conjugate plane of sample plane, so in an ideal situation only back scattered emissions from this plane will make it though the pin hole and onto the detector. The diagram below illustrates the working and difference between coherence and confocal gating.

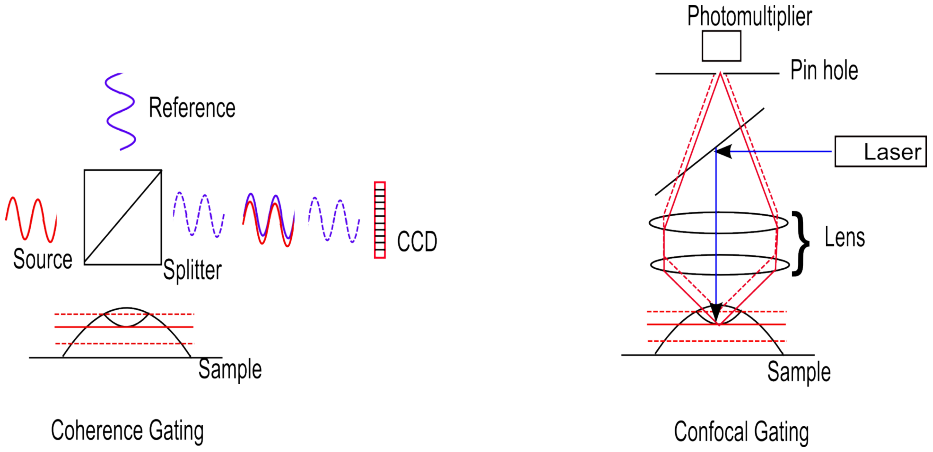

Figure 2.9: Difference between confocal and coherence gating

In coherent gating case in figure 2.9 there is only interference if the path length of the reference arm and the sample is matched and in this case the path is matched when the sample light is reflected from a point along the solid red line. So from this point there is interference but there is no interference from signals reflected from the above dashed line or the dash line below. In the confocal gating case the signal is only detected if the reflected beam focuses at the pin hole and this only happens when the sample plane is the conjugate of the pin hole plane. So in this case we only detect the reflection from the solid red line and not the dashed lines.

2.5.5 Method

To measure the SNR roll off, firstly the interference needs to be re-sampled. We find that the SNR is greatest at the path difference where the re-sampling lookup table was generated. The roll off characterises the fall of SNR with depth so the depth needs to be calibrated. The depth is calibrated by moving the reference arm by a known distance(1mm) using its micrometer stage and noting how many pixels the PSF moves. For the SNR roll off data below the system was calibrated as 1mm: 375 pixels. Therefore, every pixel is 2.7 μm. The SNR roll off measurement was started from 100 μm instead of zero path difference due to the DC component, which is still

slightly present after subtraction. From 100 μm the sample is moved in increments of 100 μm and the SNR is remeasured. The progression of the SNR roll off is graphed in figure 2.10.

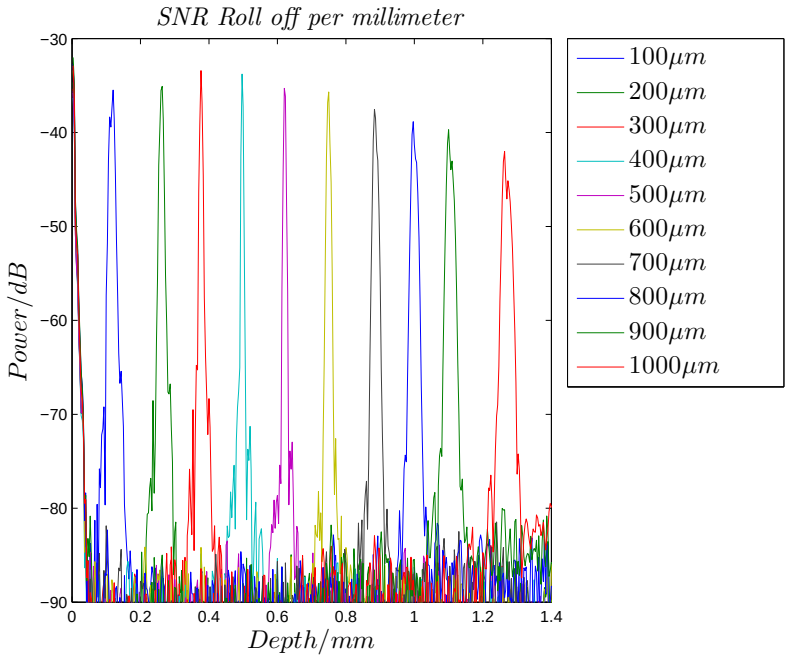

Figure 2.10: Sensitivity roll off with depth for 1mm

The SNR roll off was measured to be 6.5 dB/mm (difference between the peak at 1mm and the highest peak before). The SNR roll off appears to be better than the predicted this is discussed in the following subsection.

The SNR roll off is a very important measurement since it determines our imaging depth. Our result of 6.5 dB/mm is very comparable to systems with larger number of CCD pixels [6]. For the project large imaging depths are not crucial but it is desired because without out this the system will be limited to imaging only low scattering materials and superficial tissues. Also the axial resolution decreases with increasing depth. This noticeable with the increasing FWHM of the PSF with depth. The PSFs at 400 μm has a larger SNR compared to the other even the PSF closer to zero OPD. This is because the re-sampling from wavelength to k was done at this depth so the interpolation is more accurate than at higher or lower fringe frequencies.

2.5.6 Theoretical against measured Performance

The loss in sensitivity with increasing depth is a disadvantage in using SDOCT. The loss is due to various factors including the limited spectrometer resolution, the finite width of the pixels and aliasing at high spatial frequencies as described in section 1.3.1.1.

Comparing our measured SNR roll off to that predicted by equation (1.17) our measured SNR roll off of 6.5 dB/mm is an improvement on the theoretical prediction of 12.3 dB/mm. This occurs because from zero depth to 0.4 mm (3^{rd} peak in figure 2.10) the SNR increases rather than decrease and then falls after this point. The reason for this happening is due to the limitations in the resampling algorithm. Normally once resampling is done regardless at which frequency it was done the SNR is greatest at zero path difference and decreases there after, because the fringe frequency is lowest at the zero path difference and is easily resolved. However, this is not the case here, a possible reason for this could be that a higher order polynomial is needed when re sampling from wavelength λ to wave vector k. So the conversion is accurate at the frequency where resampling is done but falls in accuracy as the frequency reduces (smaller depth) and increases (larger depth). To get a better SNR roll off curve, the peaks in the SNR data are plot(blue line in figure 2.11) and a Gaussian curve is fitted (red line in figure 2.11) to the data. The fit curve addresses the problem of the the SNR increasing with depth. The fit curve has a decreasing SNR with depth. The fitted curve gives a SNR roll of rate of 8.84 dB/mm this is still better than the shot noise limit theoretical rate. However, the theoretical rate is calculated based on the spectral resolution of the spectrometer. The spectral resolution $\delta\lambda$ is calculated from knowing how much of the diffraction grating is illuminated, measuring this value is tricky and therefore carries with it some error. Calculating the wavelength pixel $\Delta\lambda$ spacing also carries errors since you can't exactly sure how much bandwidth you are collecting on the CCD.

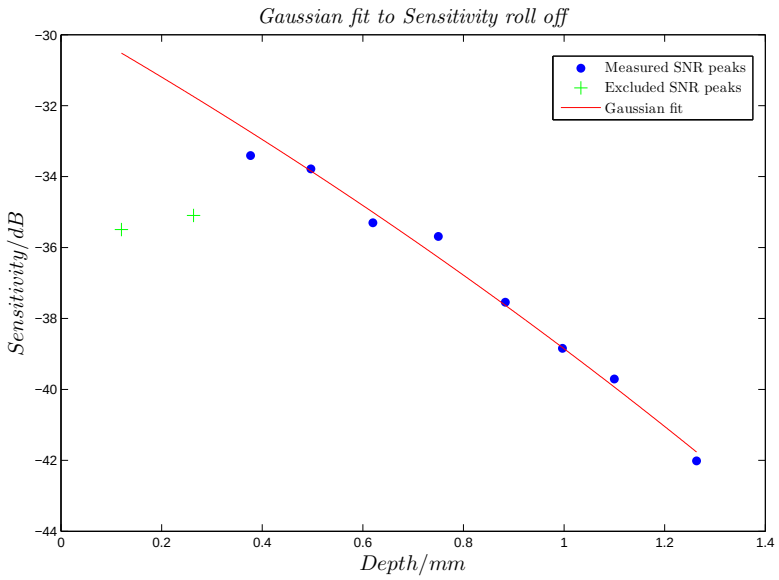

Figure 2.11: Gaussian curve fitted to sensitivity peaks. The green cross on the plot were not used in calculating the Gaussian fit curve $a \times e^{-\frac{(x-b)^2}{c^2}}$, a= -2.9×10^{174}, b = 2998, c = 150

.

2.6 Magnetomotive OCT

To track the corneal limbal epithelium stem cells, a functional OCT is needed. We decided to build and use a magnetomotive OCT for this purpose. This adaptation would require a solenoid for the actuation of the iron nanoparticles. A mild steel core solenoid was made and placed 1 cm beneath the sample. The mild steel is used to increase the field strength. The solenoid has a length of 3 cm and with 1200 turns. The solenoid produces a field of 0.08T at the sample position which was 1 cm away from the tip of the magnetic core, when a current of 1.6 A is applied at a modulation frequency of 80 Hz. The solenoid has a field gradient of 7.5 T/m.

Before constructing the solenoid, a magnetic field strength calculation was done to give an estimate of the parameters needed to achieve a field strength of 0.08 T.

$$B = \frac{\mu N I}{L} \tag{2.21}$$

Equation (2.21) was used to calculate the magnetic field strength of a solenoid. Where B is the magnetic field strength, μ is the magnetic permeability of the core, N is the number of turns and L the length of the solenoid.

The magnetic field strength increases proportionally with the wire turn density ($\frac{N}{L}$), however the minimum value of L could not be less than 3 cm due to the design of the coil winder. The coil winder could not wind a solenoid shorter than 3 cm. The applied current was to be 1.6 A but could be increased to give higher field strengths, this increase however would cause the wires wound around the core to start smoking before the imaging was complete. According to the British Stainless Steel Association (BSSA), the mild steel used as the core should have a magnetic permeability between $1.3 - 1.4 \times 10^{-6}$. Using these parameters and a mean permeability of 1.35×10^{-6} a predicted 1100 turns was needed to achieve our desired field strength of 0.08 T. In practise 1200 turns was needed as the magnetic permeability was most likely lower than was used theoretically.

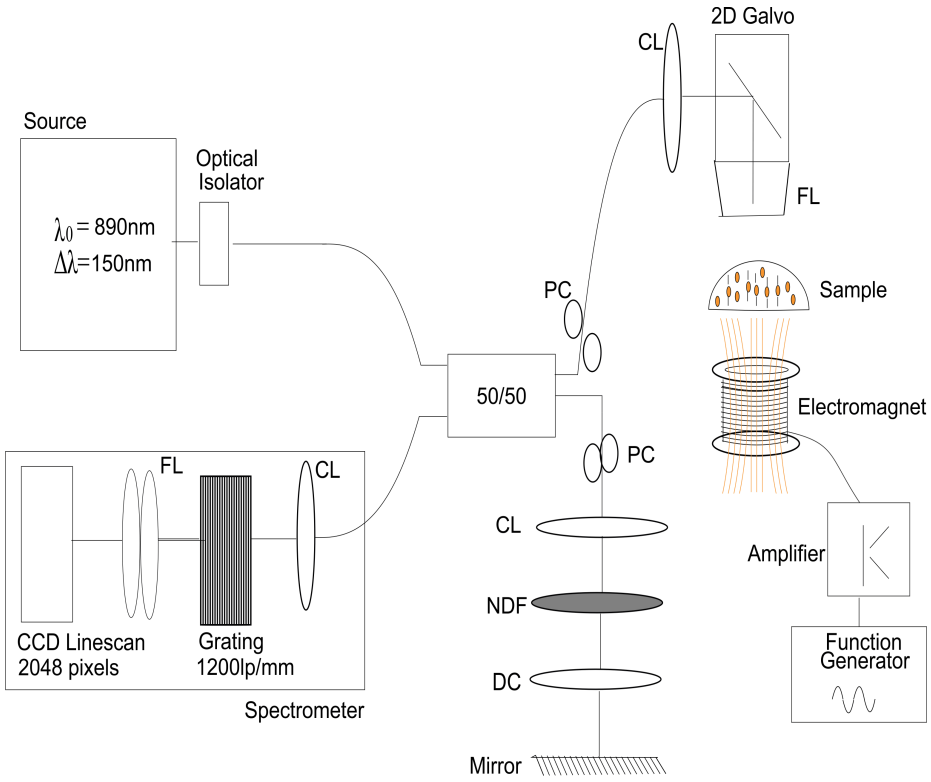

Figure 2.12:
Magnetomotive OCT Experimental Set-up

2.6.1 Phase stability

The minimum displacement detectable via this technique is limited by the phase stability of the system. The phase stability for a shot noise limited system is defined as the standard deviation of the phase fluctuations of a mirror [7] [8].

$$\textit{Phase fluctuation } (\Delta\phi) \textit{ rads} = \sqrt{\frac{1}{SNR}} \qquad (2.22)$$
$$\textit{where } SNR = 10^{SNR(dB)/10}$$

The system has a sensitivity of 95 dB this should give a theoretical phase stability of 17.8 μrads using equation (2.22).

The phase fluctuations can be converted into the minimum linear displacement measurable by using:

$$\text{Displacement } (\Delta z) = \frac{\Delta\phi\lambda_o}{4\pi n} \qquad (2.23)$$

To measure the phase stability experimentally, a M-mode scan (A scans at a single point) of a plane mirror is taken as shown in figure 2.13. During a M-mode scan the galvonometer scanners are held stationary. The depth with the highest reflectivity is selected for the phase calculation, in this case 0.9 mm. The highest reflectivity corresponds to the surface. The CCD is set to collect a 1000 A-scans in 50 μs. Taking the Fourier transforms of these A-scans gives complex expressions and the phase is obtained by finding the angles between the real and the imaginary components of these complex expressions. The phase fluctuations with time at the surface is shown in figure 2.14. The phase stability is measured as the standard deviation of the phase fluctuation. The dataset recorded had a phase stability of 522 μrad, using equation (2.23) this converts to a minimum detectable displacement of 0.37

$\mathring{A}$. The minimum detectable displacement is approximately 30 times larger than the theoretical prediction of $0.0126\mathring{A}$ from equation (2.22).

Figure 2.15 shows the Fourier transform of the phase fluctuations, this was done to show that there are no underlying vibrations without the application of the solenoid. If there were, prominent peaks at those frequencies would be present. The figure shows that there is only random noise present.

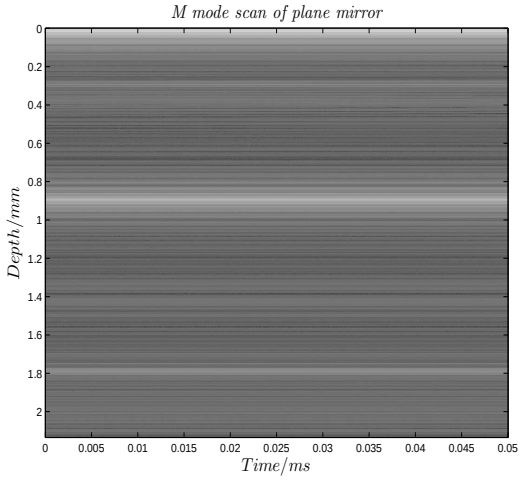

Figure 2.13: Mmode scan of mirror for phase stability measurement

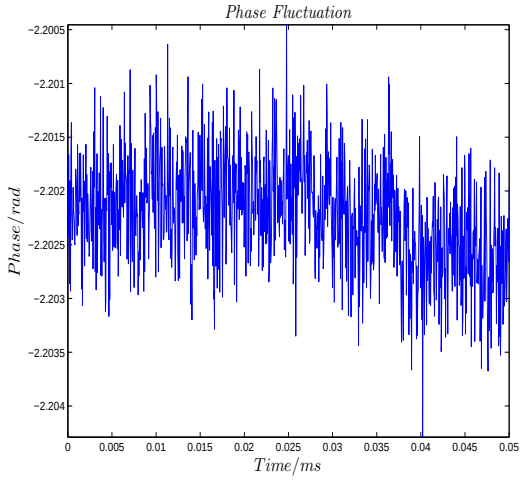

Figure 2.14: Phase fluctuation of mirror recorded for 50μs

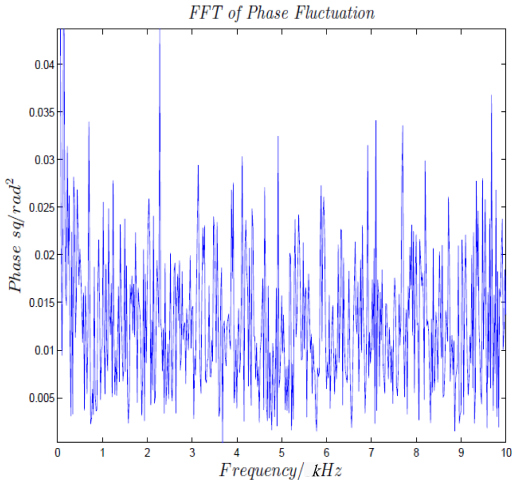

Figure 2.15: Fourier transform of phase fluctuation. No prominent vibrational signals are seen

References

[1] J. F. de Boer, B. Cense, B. H. Park, M. C. Pierce, G. J. Tearney, and B. E. Bouma, "Improved signal-to-noise ratio in spectral-domain compared with time-domain optical coherence tomography," *Optics Letters*, vol. 28, pp. 2067–2069, 2003.

[2] N. A. Nassif, B. Cense, B. H. Park, M. C. Pierce, S. H. Yun, B. E. Bouma, G. J. Tearney, T. C. Chen, and J. F. de Boer, "In vivo high-resolution video-rate spectral-domain optical coherence tomography of the human retina and optic nerve," *Optics Express*, vol. 12, pp. 367–376, 2004.

[3] Z. Yaqoob, J. Wu, and C. Yang, "Spectral domain optical coherence tomography: a better oct imaging strategy," *BioTechniques*, vol. 39, pp. S6–13, 2005.

[4] S.-W. Lee, H.-W. Jeong, B.-M. Kim, Y.-C. Ahn, W. Jung, and Z. Chen, "Optimization for axial resolution, depth range, and sensitivity of spectral domain optical coherence tomography at 1.3 mu m," *Journal of the Korean Physical Society*, vol. 55, pp. 2354–2360, 2009.

[5] S. Yun, G. Tearney, B. Bouma, B. Park, and J. de Boer, "High-speed spectral-domain optical coherence tomography at 1.3 μm wavelength," *Optics Express*, vol. 11, no. 26, pp. 3598–3604, 2003.

[6] B. Potsaid, I. Gorczynska, V. J. Srinivasan, Y. Chen, J. Jiang, A. Cable, and J. G. Fujimoto, "Ultrahigh speed spectral/fourier domain oct ophthalmic imaging

at 70,000 to 312,500 axial scans per second," *Optics express*, vol. 16, no. 19, pp. 15149–15169, 2008.

[7] C. Joo, T. Akkin, B. Cense, B. H. Park, and J. F. de Boer, "Spectral-domain optical coherence phase microscopy for quantitative phase-contrast imaging," *Optics letters*, vol. 30, no. 16, pp. 2131–2133, 2005.

[8] M. A. Choma, A. K. Ellerbee, C. H. Yang, T. L. Creazzo, and J. A. Izatt, "Spectral-domain phase microscopy," *Optics Letters*, vol. 30, pp. 1162–1164, 2005.

Chapter 3

Imaging corneal limbal epithelium stem cells using Magnetomotive OCT

3.1 Summary

The prevailing hypothesis for the existence and healing of the avascular corneal epithelium is that this layer of cells is continually produced by stem cells in the limbus and transported onto the cornea to mature into corneal epithelium. Limbal Stem Cell Deficiency (LSCD), in which the stem cell population is depleted, can lead to blindness. LSCD can be caused by chemical and thermal burns to the eye. A popular treatment, especially in emerging economies such as India, is the transplantation of limbal stem cells onto damaged limbus with hope of repopulating the region. Hence regenerating the corneal epithelium. In order to gain insights into the success rates of this treatment, new imaging technologies are needed in order to track the transplanted cells. Optical Coherence Tomography (OCT) is well known for its high resolution in vivo images of the retina. A custom OCT system has been built to image the corneal surface, to investigate the fate of transplanted limbal stem cells. We evaluate

magneto-labelling for tracking the transplanted cells. To evaluate magneto-labelling the stem cells are loaded with magnetic nanoparticles (20-30nm in size) and then imaged with a custom-built, magneto-motive OCT system. The imaging was done on a mixture of SPIO with gelatin, agar and finally on rabbit cornea. The results show that the system can detect transplanted cells with SPIOs embedded.

3.2 Introduction

Magnetomotive Optical Coherence Tomography is a functional adaptation of OCT. An electromagnet is used to displace the magnetic contrast agents in a sample and the displacement is retrieved via phase resolved measurements. The MMOCT can operate as an amplitude modulator, in this case a scan is taken of the sample with the magnetic (B) field off (control) and then the scan repeated with the B field on. The location of the contrast agents are identified by subtracting the images. This technique is quite slow because it requires scanning the sample twice before the contrast agents can be located. However, it is possible to modulate the B field at a set frequency f_B and then carry out a lock in detection at this frequency to locate the contrast agents. In the experiments conducted, superparamagnetic iron oxides are used. Superparamagnetism is a subset of magnetism which applies to small ferromagnetic or ferrimagnetic nanoparticles. Small refers to a diameter size of between 3-50nm. Superparamagnetic materials which essential have a single magnetic domain can be magnetised by change in temperature but when an external magnetic field is applied they align with the field applied. The application of an external field to the superparamagnetic materials causes the material to be displaced. The displacements experienced by the superparamagnetic iron oxide (SPIOs) causes a phase change in the interferometric signal recorded.

In OCT the intensity recorded is the sum of self interference from the reference I_r, sample arms I_s and the cross interference $2\mathbb{R}\{I_r I_s^*\}$. The cross interference carries

encodes the depth information used in producing the image.

$$\begin{aligned} I_{out} &= I_r + I_s + 2\mathbb{R}\{I_r I_s^*\} \\ 2\mathbb{R}\{I_r I_s^*\} &= 2cos(kz + \phi) \\ \Delta\phi(\Delta z) &= \frac{2\omega n_{air}\Delta z}{c} \end{aligned} \tag{3.1}$$

From equation (3.1), we know that a shift Δz in the spatial domain will manifest as a change in the phase.

The purpose of this study was to demonstrate that MMOCT system with superparamagnetic iron oxide (SPIO) nanoparticles as contrast agents can be used to locate and track stem cells on the cornea. Three experiments were carried out the first was M-mode imaging of gelatine/milk samples mixed with SPIOs, this experiment was done to test and validate the MMOCT system. Also this was done to investigate whether the MMOCT could detect SPIOs at a depth and whether the SPIOs surroundings had an effect on the phase modulation. A M-mode is an acquisition technique, where the imaging beam is held in a fixed location. M-mode shows the reflectance of region been imaged evolves with time.

Before the arrival of the rabbit corneas agar phantoms were used as a replacement for the corneas. Agar phantoms are commonly used to mimic the mechanical and optical properties of soft tissue [1]. SPIOs were placed both on top of the agar samples to test whether the SPIO location could be highlighted even in the presence of strong Fresnel reflection. Finally, rabbit limbal epithelium cells (rLEC) embedded with SPIOs were transplanted onto the rabbit cornea epithelium. Different rLEC densities were transplanted onto the cornea and investigated.

3.3 Materials

3.3.1 Superparamagnetic iron oxide (SPIO) nanoparticles

Magnetite $Fe_3^{(II,III)}O_4$ SPIO nanoparticles powder (#637106, Sigma Aldrich) of size 20-30 nm were used [2] . SPIOs in this size range can be used in both in-vivo and in-vitro applications. In 1996 the FDA approved the use of magnetite SPIOs after a toxicology study [3]. The particles are uncoated so we do see aggregation of the particles during preparation and imaging. Different coatings can be used to reduce the aggregation effect and also the use of coatings such as dextran and aminosilane [4] [5] have been said to improve the cellular uptake of SPIO in mouse macrophages. Bare SPIO have been shown not to affect cell viability in various tissues [4]. The particles are paramagnetic and hence the force exerted on particles remains in one direction irrespective of the polarity of the magnetic field.

$$\vec{F_p} = \frac{V(\chi_p - \chi_{medium})\nabla \mid \vec{B} \mid^2}{2\mu_o} \tag{3.2}$$

$\vec{F_p}$ is the force exerted on particle, χ_p is the magnetic susceptibility of the SPIO particle, χ_{medium} is the magnetic susceptibility of the medium surrounding SPIO particle and $\vec{B}$ is the magnetic field.

3.3.2 Magnetic field generator

We constructed an in-house MMOCT using a wound solenoid with a ferrite core (mild steel). The solenoid has both length and outer radius of 3 cm and with 1200 wire turns. The solenoid produces a field of 0.08 T at the sample position (1 cm away) when a current of 1.6 A is applied at a modulation frequency of 80 Hz. The solenoid

has a field gradient of 7.5 T/m at this frequency.

3.3.3 Animal models

Animal models, eyes were obtained from New Zealand albino rabbits generously donated by Dr. Toby Holmes (University of Sheffield) and also some eyes from wild-bred rabbits were purchased (Blackface Meat Company). The eyes were removed and dissected to separate the posterior and anterior segments. The reason for dissection is to allow the cornea to be flattened for imaging, if not flattened due to the cornea's curvature the limbus can not be imaged because of the SNR roll off with depth. The dissection of the eyes does not mean that the MMOCT imaging technique can not be used in a clinical setting. In a clinical environment the patient can be asked to look in various directions and to turn their head, so the region of the eye been imaged is nearly perpendicular to the imaging beam.

3.3.3.1 Rabbit limbal epithelial cells (rLEC)

To replicate the clinical scenario rLEC are harvested from the rabbit's limbus to later be labelled with SPIO and transplanted back onto the cornea to be located using the MMOCT system. Before harvesting the rLEC, the eyes are cleaned initially by removing excess fat and tissue on the globe and then disinfected using 3% videne antiseptic solution(Ecolab, Swindon, UK). The limbal region of the cornea was excised into segments and placed into Dispase II of concentration 2.5 mg/ml(Roche Diagnostics Ltd) at 37^{o}C and 5% CO_2 for 45 min. The limbal cells are then scraped off the tissues into phosphate buffered saline(PBS) solution using a blunt scalpel blade. The PBS and limbal cells solution was centrifuged at 1000 rpm for 5 min. The supernatant was discarded and the cells were re-suspended in fresh epithelial culture medium. The cells were seeded into flasks containing growth arrested NIH3T3 murine fibroblasts as a feeder layer. The culturing media for the rLEC consisted of Dulbecco's Modified Ea-

gle Medium (DMEM GlutaMAX^{TM}, D0819-500ml) and Ham's F12 medium (N4888-6x500mL) with 1:1 ratio augmented with 10% foetal calf serum (F9665-500mL), 5 μg/ml insulin(91077C-1G), 10 ng/ml epidermal growth factor(E5036-200UG), 2.5 μg/ml Amphoterin B (A2942-100mL)and 100 U/ml penicillin with 100 g/ml streptomycin (P0781-100mL) the above components are purchased from Sigma Aldrich. For the experimentation passage 2 cells were used.

The figure 3.1 below shows the experimental setup of the MMOCT system. The system is the based on the previously built ultra-high resolution SDOCT with the main addition being the electromagnet.

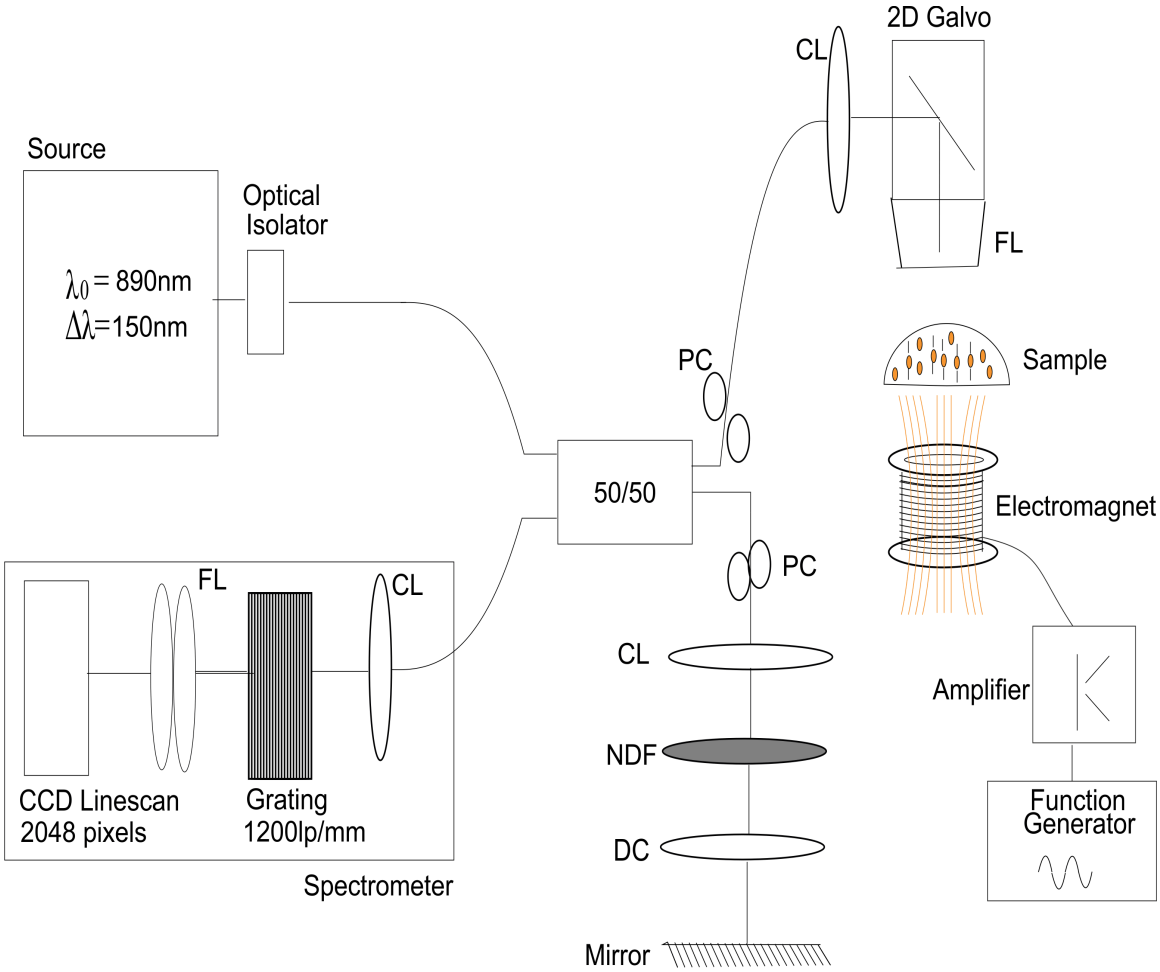

Figure 3.1: Phase resolved MMOCT experimental setup

where OI: Optical Isolator, PC: polarization controller, LP: linear polarizer, CL: collimating lens, NDF: Neutral density filter, DC: dispersion compensation, FL: focusing

lens and CCD: charged couple device.

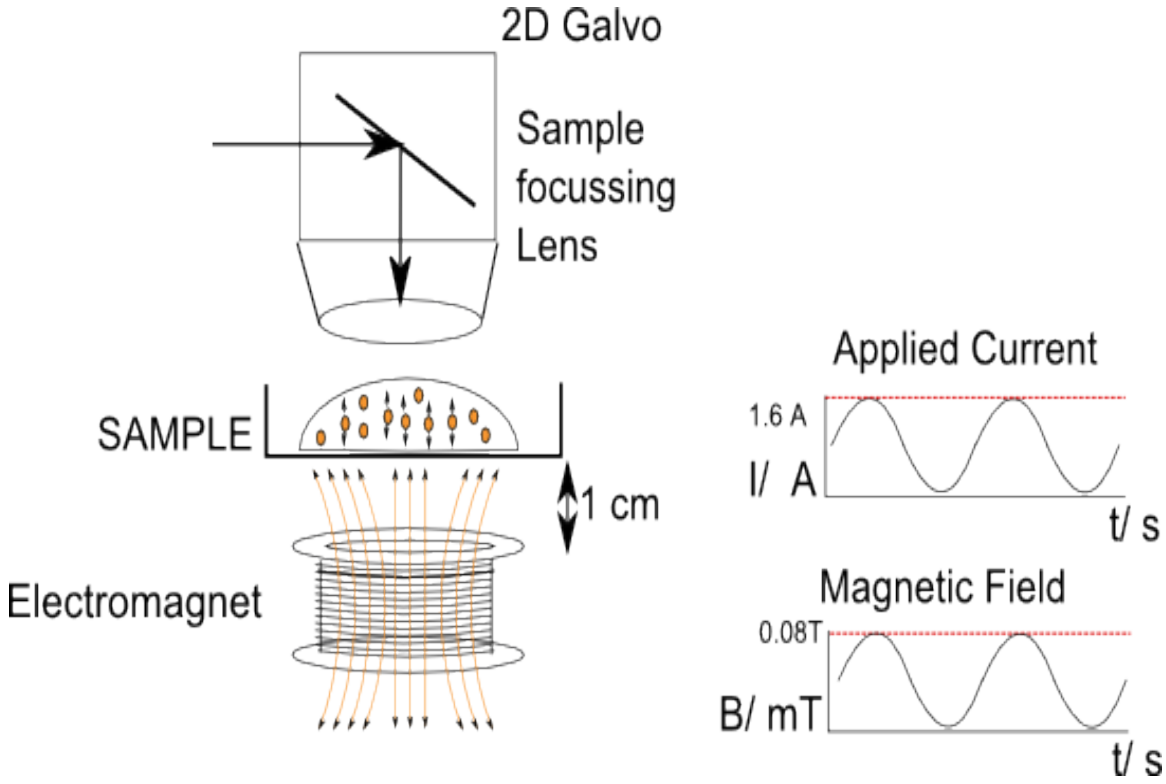

Figure 3.2: Phase resolved MMOCT experimental setup

3.4 M-mode imaging of gelatine phantoms

The MMOCT system works by actuating the SPIO nanoparticles with an external magnetic field at a specified frequency. The aims of this experiment was to firstly determine if the B field produced by the solenoid is sufficient, then to investigate if the SPIOs actuations could be detected by phase resolving the interferometric data from the MMOCT and finally confirm the signal detected originated from the SPIOs. In this experiment phantoms were made compromising of gelatine and milk. The milk is added as an optical scatterer. M-modes were acquired of the phantoms, to be used to analyse how the amplitude and phase of the spectral data evolve over time with the B field being modulated. The phase fluctuations will be used to verify the magnetic modulation frequency detected corresponds to double the frequency applied and also used to calculate the displacement of the SPIOs.

3.4.1 Method

The current for the solenoid originates from a function generator (#72-6805,Tenma) and is amplified by an audio amplifier (#7224, AE Techron) to a peak current of 1.6 A. This current gives a B field strength of 0.08 T. The peak B field produced by the solenoid was measured using a Gaussmeter (GM05,Hirst). For this experiment a modulation frequency of 20 Hz was used. The field was measured to be 144.6 mT on the tip of the solenoid core and 80 mT at the sample position. The B field produced is comparable to that found in the literature for similar set-up and experimentation [2]. Gelatine phantoms were made using 2.5 mg of dried gelatine with 50 mL of milk to act as an optical scatterer. Six concentrations 1 mg/ml, 0.5 mg/ml, 0.25 mg/ml, 0.1 mg/ml, 0.05 mg/ml, 0.01 mg/ml and control where no SPIOs are added; 20 μl of each was pipetted into a petri dish to be imaged. For example, the 0.01 mg/ml corresponds to a mass of 0.01 mg of SPIO mixed in a 1 ml solution of the gelatine

and milk solution. A-scans were collected with a camera line rate of 20 kHz and a camera exposure time of 50 μs. The camera acquisition rate seems quite high for the modulation frequency applied to the SPIO and hence the modulation frequency is seen quite close to the DC component. Nevertheless, there is clear evidence for the presence of magnetic induced displacement. The high exposure time is selected to collect the maximum signal. The aim of this experiment is not fast acquisition but to confirm that a magnetically induced signal can be observed. The solenoid is placed 1 cm underneath the sample and the magnetic field is applied whiles the A scans are acquired. A schematic of the sample set up in relation with the electromagnet is show in figure 3.2. After the collection of one frame consisting of a 1000 A scans, the phase was evaluated at a constant depth of 20 μm underneath the surface for the duration of the acquisition. The MMOCT signal detectable will fall with depth. As SNR falls so does the MMOCT sensitivity. The depth of 20 μm was used so the area of investigation is close enough to surface but not at the surface. The MATLAB script used to process the phase and frequency detection is attached in the Appendix.

A one dimensional Fourier transform of the phase is computed along the transverse direction to give the frequency components in the phase signal at this depth.

Figure 3.3a shows the M-mode image of the 0.01 mg/ml sample. All the other concentrations have very similar structural M-mode images and does not give any extra information so are not included here. The green line shows the line of interest (20 μm) where the phase resolving technique was applied.

3.4.2 Results

Five SPIO concentrations and a control were investigated. With the magnetic field applied the SPIOs should be displaced along the axial direction predominately. This is assumed due to the close proximity of the sample to the tip of the electromagnet. The M mode acquisitions shows the evolution of the SPIO's displacement with time. The

spectrum of the displacements gives a modulation frequency of twice the modulation frequency (f_B) due to the paramagnetic nature of the nanoparticles.

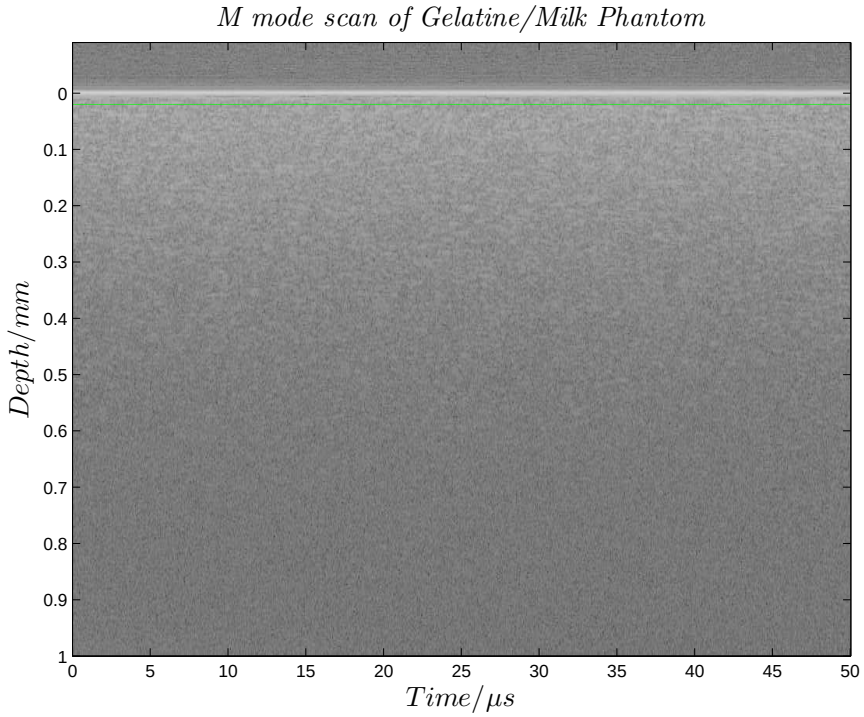

(a) M-mode of Gelatine/milk phantom with SPIO mixed at 0.01mg/ml

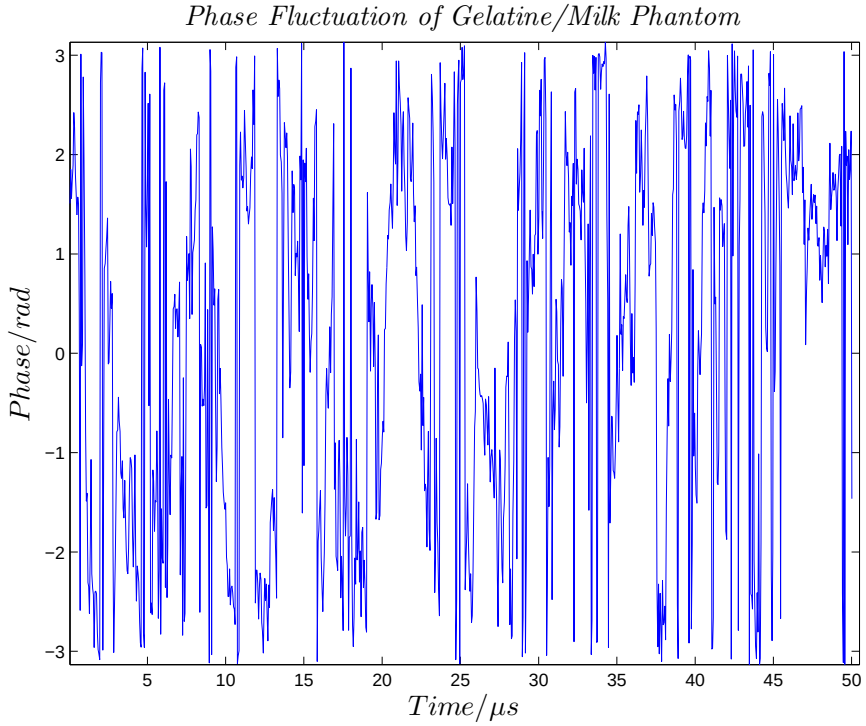

(b) Phase evolution over 50μs for Gelatine/milk phantom with SPIO mixed at 0.01mg/ml

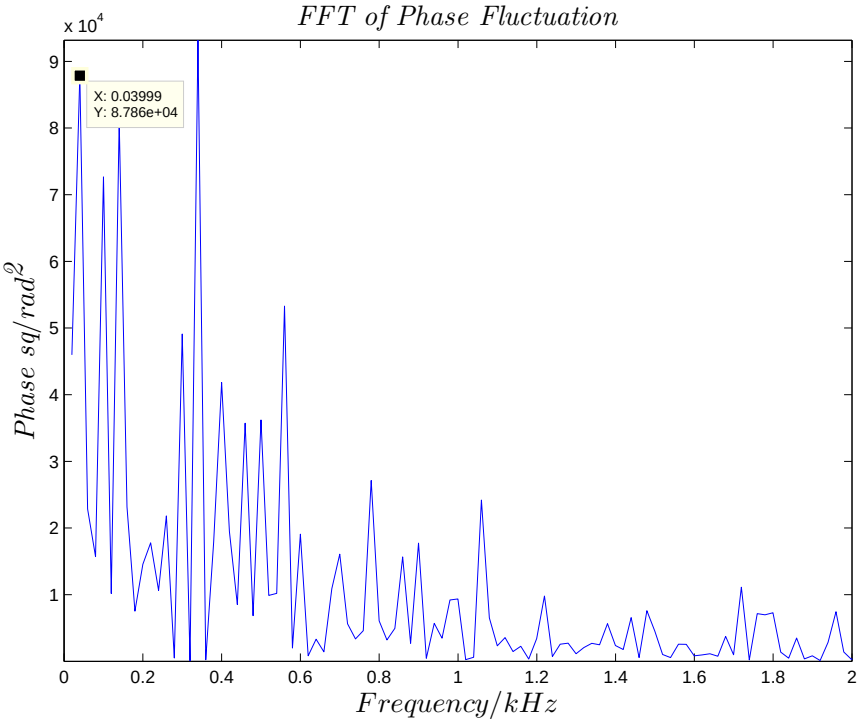

(a) FFT of Phase fluctuation for Gelatine/milk phantom with SPIO mixed at 0.01mg/ml. The 40Hz modulation is detected

Figure 3.4: M-mode scan and spectrum of Gelatine/milk phantom with a magnetite concentration of 0.01mg/ml

In figure 3.4a the first peak is at the 40Hz, this is twice the frequency applied (20Hz) to the samples. This is discussed in the subsequent section.

A control sample (without any SPIOs) was also processed to confirm that without the SPIOs there should be no magnetic induced displacement signals present. The amplitude for the 40Hz component is a lot smaller in comparison to the samples containing SPIOs as seen in figure 3.5b.

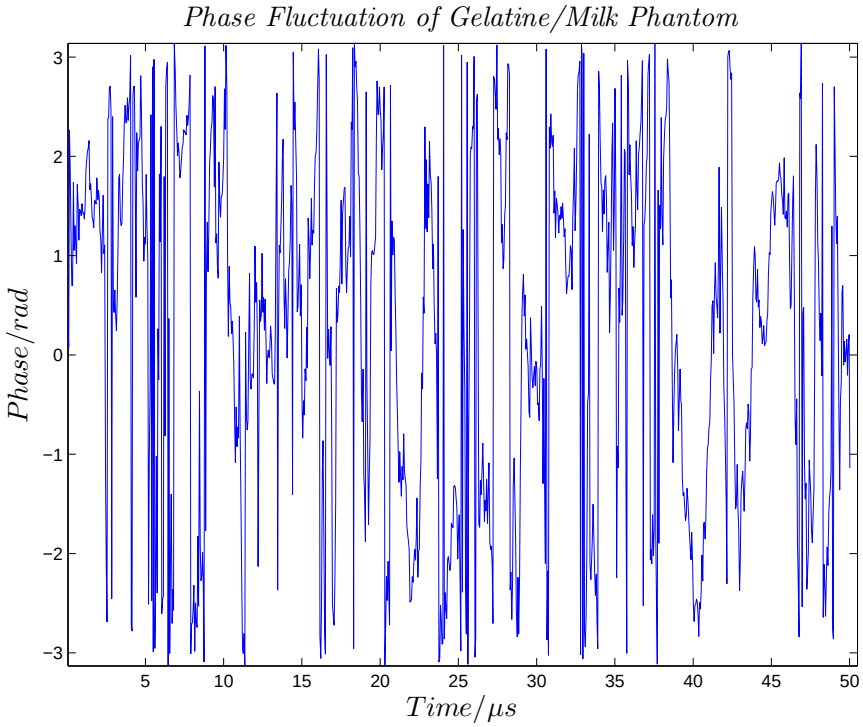

(a) Phase evolution over 50μs for Gelatine/milk phantom with no SPIO

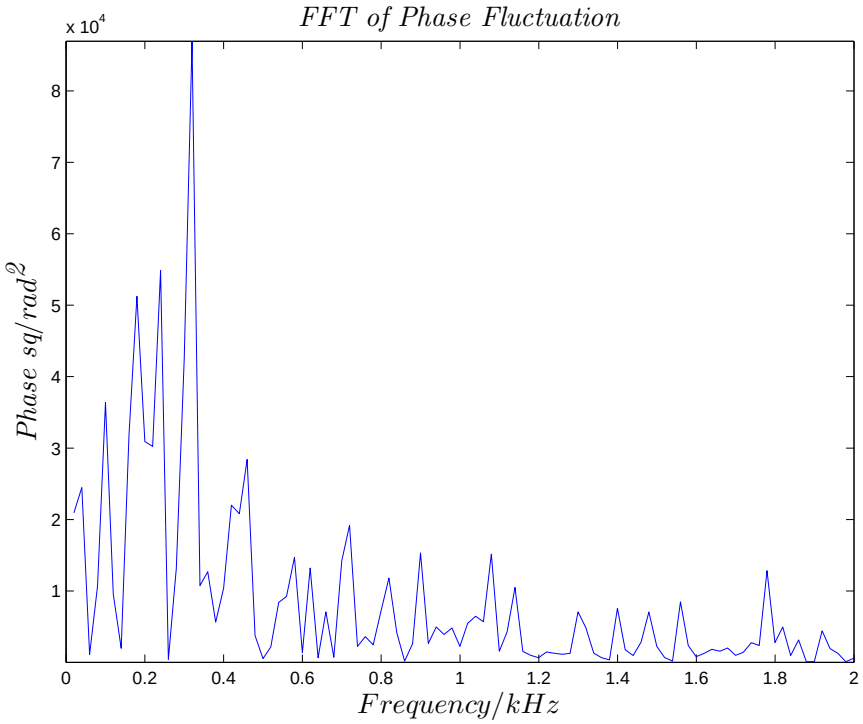

(b) FFT of Phase fluctuation for Gelatine/milk phantom with no SPIO

Figure 3.5: The time evolution and spectrum of a control sample(without any magnetite) shows very low signal at 40Hz

In the higher SPIO concentration samples >1mg/ml the phase modulation is greater and much more evident graphically. Below is the phase graph for sample with 1mg/ml of SPIOs to gelatine, it exhibits prominent phase modulation at the 40Hz.

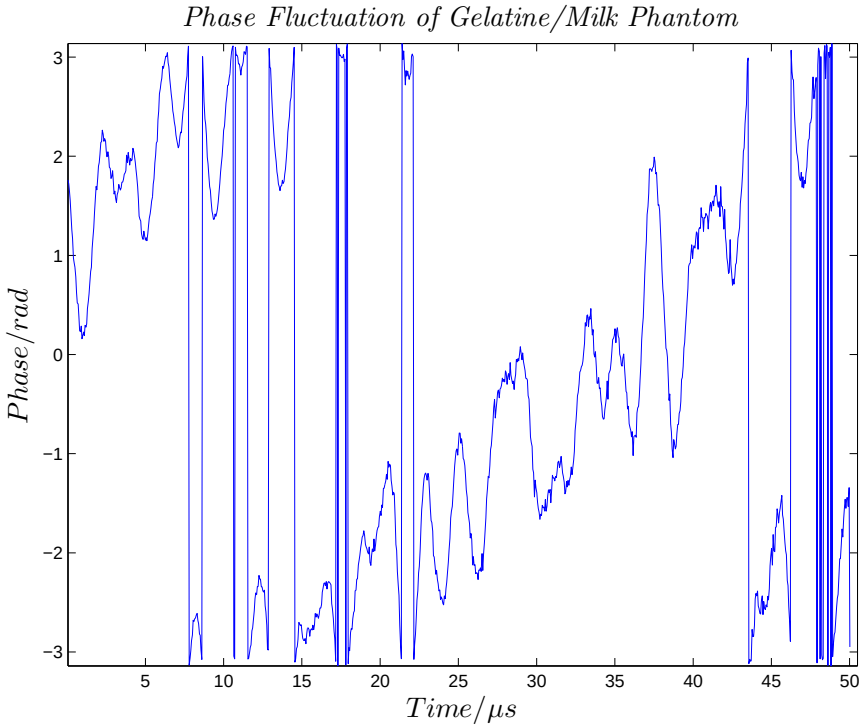

(a) Phase evolution over 50μs for Gelatine/milk phantom with SPIO mixed at 1mg/ml

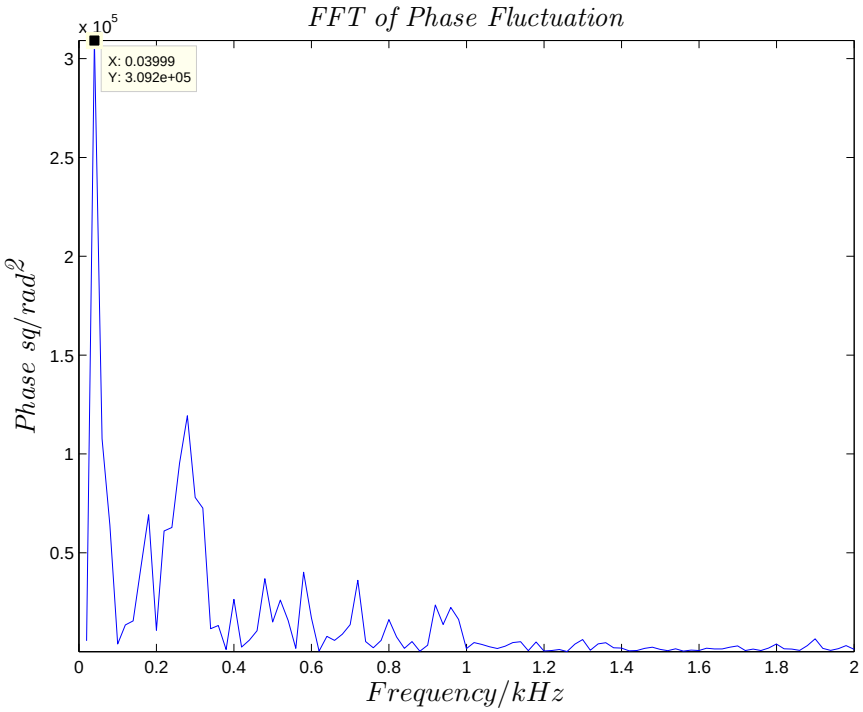

(b) FFT of Phase fluctuation for Gelatine/milk phantom with SPIO mixed at 1mg/ml. The 40Hz modulation is detected

Figure 3.6: M-mode scan and spectrum of Gelatine/milk phantom with a magnetite concentration of 1mg/ml

3.4.3 Discussion

The milk was added to the gelatine to act as an optical scatterer, to increase the amount of return reflected light. This increases the SNR and thus reduces the phase noise floor. Although a frequency of 20Hz is applied to SPIOs, a frequency of 40Hz is detected. The doubling of the applied frequency is due to the paramagnetic nature of the nanoparticles. Regardless of the direction of the B field the nanoparticles are attracted to the solenoid. The doubling of the frequency is also explained by equation (3.2), the squaring of the B field causes the force to oscillate at a second harmonic of the field oscillation frequency. For the control sample there is no presence of the magnetically induced signals. The samples containing SPIOs show a frequency response with an amplitude greater than the controls at 40Hz. The difference in amplitude ranges from four times greater in the 0.01mg/ml sample to an order of magnitude for the 1mg/ml sample.

It is possible for the control sample to show a presence of magnetic induced signals. This occurs if the parts of the MMOCT system in the vicinity of the solenoid can be magnetised. However, the frequency would be at the fundamental frequency if the parts gained a permanent remnant magnetization. Taking this into account the sample holder was constructed of a plastic composite. This can be noticed more easily in 2D MMOCT imaging where the whole sample would exhibit magnetically induced displacements because the whole sample is displaced not localised regions within. The above results show that the samples with SPIOs present do exhibit magnetic induction motion and can be detected using our MMOCT system. The signal can be detected in concentrations as low as 0.01mg/ml corresponding to 2.7×10^{-22}g of iron within 20μl sample volume.

3.5 Agar Phantoms

Our overall aim of the project was to detect the location of SPIOs embedded in rLEC on the cornea. One challenge would be the Fresnel refection at the air-cornea interface. We used agar to mimic the cornea since agar would also give a high reflectivity at the surface. Agar is commonly used as tissue mimicking phantom [6]. In this experiment we investigate the sensitivity of the MMOCT system to SPIOs on an air/agar interface and also whether SPIOs at a depth can also be detected.

3.5.1 Method

The experimental setup is the same as the one used in the M-mode imaging, however, here B-scans are acquired so the spatial positions of the SPIOs can be identified. In this experiment the SPIO nanoparticles are embedded into rabbit limbal epithelium cells (rLEC), these loaded cells are then transplanted onto the agar surface to be located. The rLEC are transported in media, the reflection from the air/liquid interface causes bright Fresnel reflection. This is due to the large change in refractive index at the air-liquid interface. To acquire B scans and maintain transverse phase correlation, the acquisition rate of the camera is reduced to oversample in the transverse direction. The oversample leads to an increase in acquisition time so to compensate the image length is reduced from 4mm to 2mm.

3.5.1.1 rLEC Preparation

In the experiment 1.5% agar is used. The agar is made from powder agar with PBS. The agar is allowed to set and then the rabbit limbal epithelium cells (rLEC) were placed on top. The rLEC has the SPIO embedded. The rLEC were cultured in a SPIO/media solution of concentration $83\mu g$/ml for 24 hours to allow for the uptake

of the nanoparticles. After the time had elapsed the rLEC are washed four times with PBS and the supernatant discarded. This is done to remove any SPIOs not taken up by the rLEC. The rLEC loaded with SPIOs are obtained by firstly using 3ml trypsin for approximately 2 minutes to dislocate the cells from the base of the T75 flask in which they are cultured. The trypsin is the then inhibited by the rLEC media which contains FCS. The resulting solute is centrifuged at 1000 rpm for 5 minutes. The supernatant is discarded to leave behind the SPIO embedded cell pellet. The cell pellet is re-suspended and 10μl is added on to the agar. The number of cells were counted using a haemocytometer. For the experiment 23×10^3 cells were used.

3.5.1.2 Acquisition Setting

The camera acquisition rate was reduced from the 20kHz to 1 kHz and exposure time 50μs. The galvanometer is set to scan 2mm in the transverse direction, this corresponds to 500 A scans. The galvo scan speed is reduced by a factor of 10 this gives a finer and a more oversampled image. A total of 5000 A scans are collected.

3.5.1.3 Phase Processing

The oversampling is done to permit the phase changes to be calculated. The phase is unwrapped to remove 2π ambiguities using the MATLAB "unwrap" function. Short Time Fourier Transform (STFT) a specialised adaptation of the Fourier transform is used to look for the solenoid modulation frequency. STFT is used here because we seek to spatially localise the origin of the modulation frequency. The STFT sections the data into multiple segments and performs the FFT on each segment. Prior to performing the FFTs, a Hanning window is applied to each segment to reduce the spectral leakage in the spectrum. A pitfall of STFT is the trade off between the spatial resolution and frequency resolution due to the sectioning of the data. For a larger section/bin sizes we achieve a better frequency resolution, the modulation frequency is well defined but the spatial resolution decreases and the accuracy of the

location of SPIOs decreases. In the experimentations a bin size of 50 points ($20\mu m$) was chosen to optimise the spatial resolution.

Figure 3.7, a flow diagram illustrating the process acquiring a B scan and using it to compute, the STFT image which maps the locations of the oscillations at $2f_B$. These locations are taken to be the locations of the SPIOs and hence that of the rLEC since the controls(without any SPIOs) give no significant signals above the background.

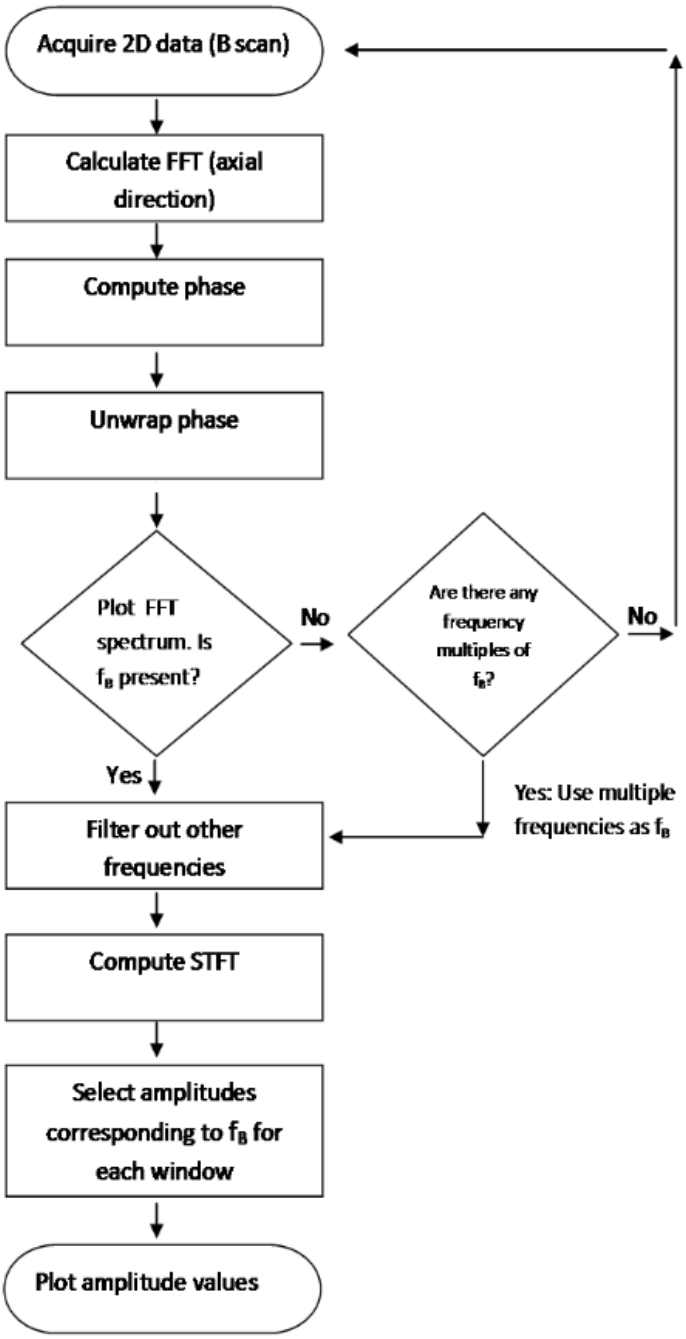

Figure 3.7: Process for computing STFT images

In figure 3.7, a spectrum is plotted at the fifth step in the flow diagram, this is to check that the magnetic modulation displacements at $2f_B$ are present. If the frequency f_B is not present then, a new B scan can be acquired. However, if a multiple of the frequency f_B is present the STFT would be computed to see which location the signals are originating from as it may give information about the medium the nanoparticles are in. The reason for f_B not been present can be numerous, including the solenoid not been aligned underneath the sample correctly. The solenoid not being vertically aligned with the sample will mean the sample will experience a reduced magnetic field strength and therefore only be displaced by a small amount; which might be below the sensitivity of the system. If the frequency f_B is present the STFT can be computed, this stage includes the application of the Hanning window. Following this the amplitudes corresponding to the frequency f_B for each section is found and inserted into a new matrix to produce a modulation amplitude map. The locations with SPIOs present have a larger amplitude. We purposely choose a frequency away from the DC component in the FFT because this will contain any optical phase changes inherent to the system and not time dependent.

3.5.2 Results

In our results the top layer containing the SPIOs display a higher amplitude than the rest of the agar phantom. The higher amplitude is due to the larger displacement experienced by the SPIOs. These results prove that the MMOCT system can be used to locate SPIOs in 2D. During the experimentation it was observed that interference from the fluorescent light was leaking into the measurement. The fluorescent light produces frequencies at twice the mains; 100 Hz and its harmonics. These frequencies were only present if the measurements were done with the lights on.

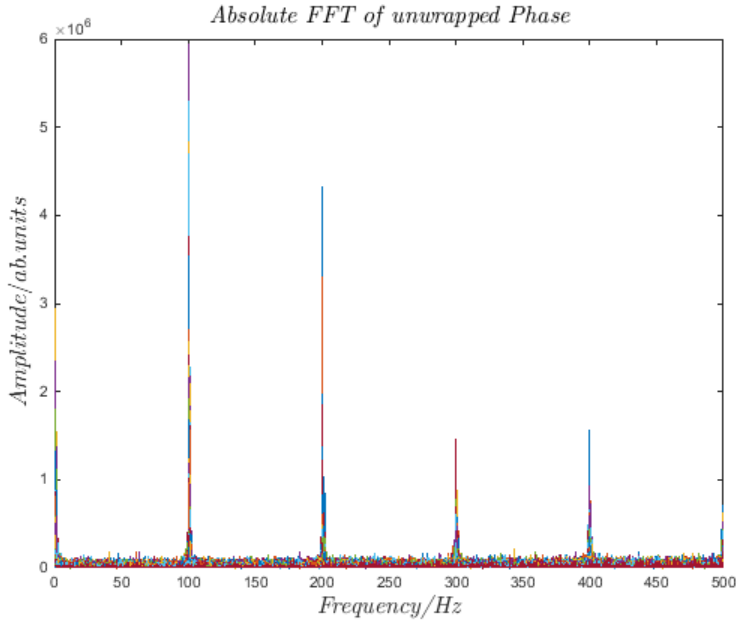

(a) Plot shows 100Hz and harmonics from the lab's fluorescent tubes

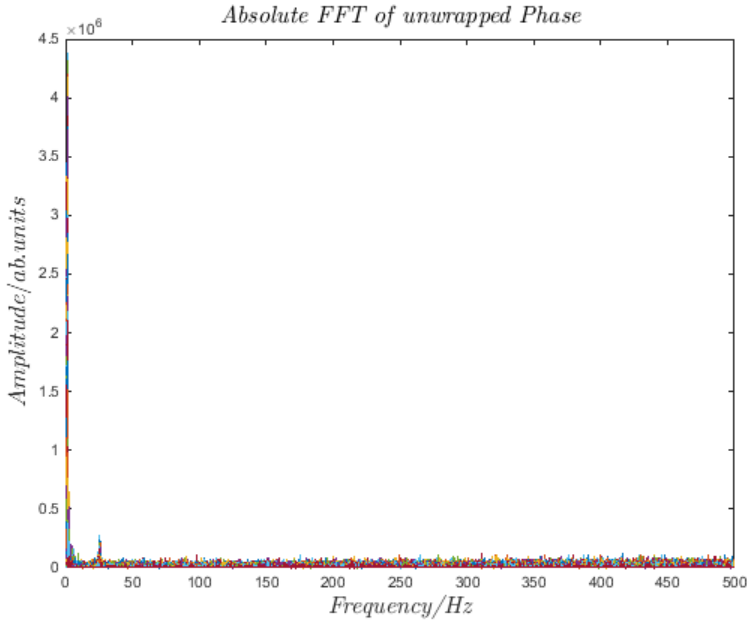

(b) 100Hz and harmonics disappear when the fluorescent lights are turned off

Figure 3.8: Shows the presence of 100Hz and its harmonics when the lights are kept on during imaging b) shows the absence of these frequencies when the imaging is done in a dark room. The colours correspond to different depths in the image

When taking MMOCT measurements the fluorescent lights in the lab has to be turned off because the lights produced modulation signals at double the mains frequency and its harmonics (100Hz, 200Hz, 300Hz...).

The SPIO/milk mixture is at a concentration of 83μg/ml SPIO:milk. 10 μl of the SPIO/milk solution is added to the surface of the agar phantom.

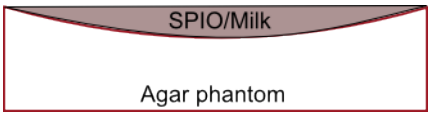

Figure 3.9: Diagram of SPIO/Milk solution on top of agar phantom

Figure 3.10a shows the images of SPIO mixed with milk, the milk makes the layer containing the SPIOs visible on top of the agar.

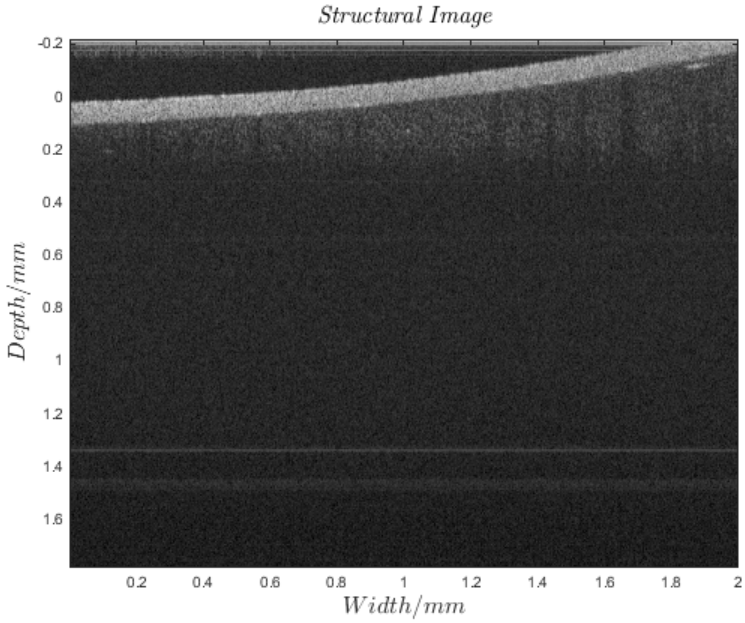

(a) Structural B scan image of the SPIO/milk solution on the agar phantom surface. The agar phantom forms a meniscus when it solidifies

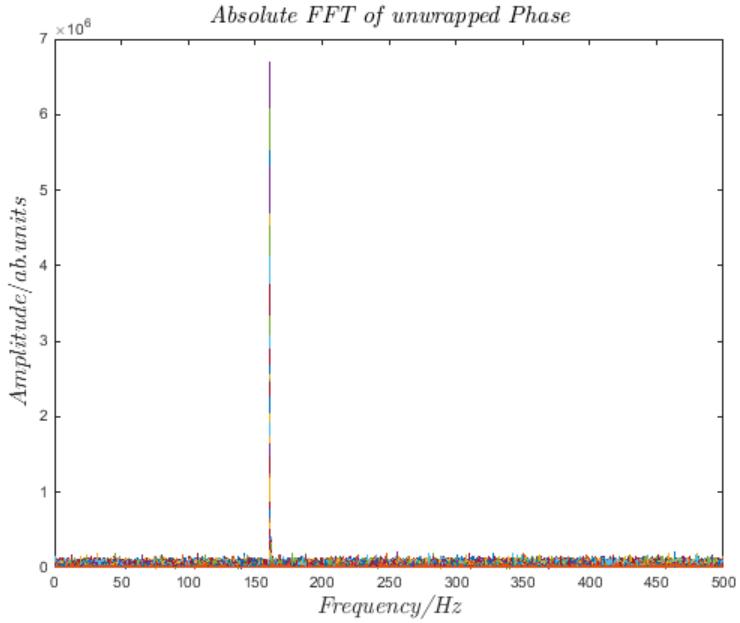

(b) FFT computed shows MMOCT signal at 160Hz as expected at double the f_B

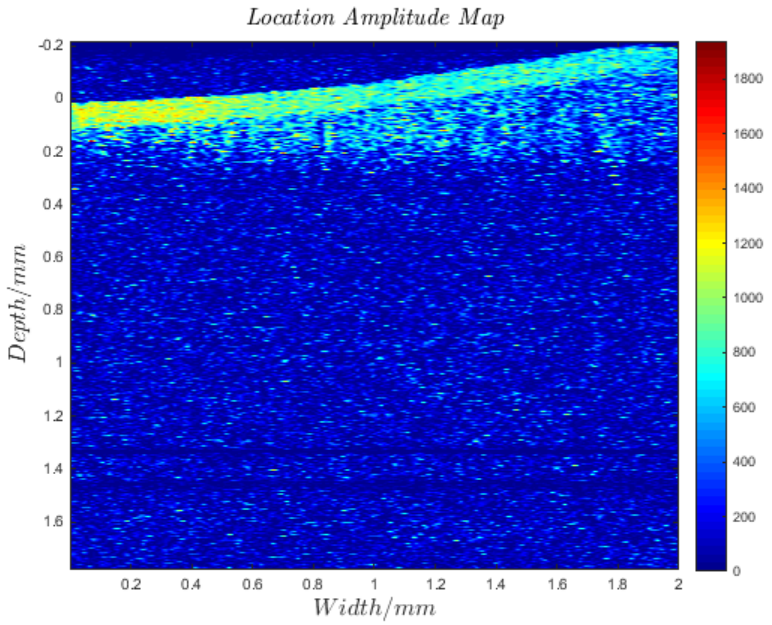

(c) Location map of the SPIO nanoparticles. The SPIO/milk layer has a higher displacement amplitude compared to the agar phantom.

Figure 3.10: The structural B scan and its corresponding SPIO nanoparticle location map for SPIO/milk of concentration $83\mu g/ml$.

In Figure 3.11 the SPIO/milk mixture was allowed to dry in the incubator (temperature= 37^oC , CO_2 level= 5%) for two hours. The drying process evaporates the water in milk leaving behind the SPIOs and lipid molecules from the milk. Both the structural image and the location amplitude map can be seen to have a thinner top layer due to the dehydration process. The layer appearing thin is due to the sectioning(window) size used in the STFT. Both results dried and non dried used a window size of 50 pixels for the STFT, the spatial resolution would have degraded and the top layer would appear thicker if a larger window size was used.

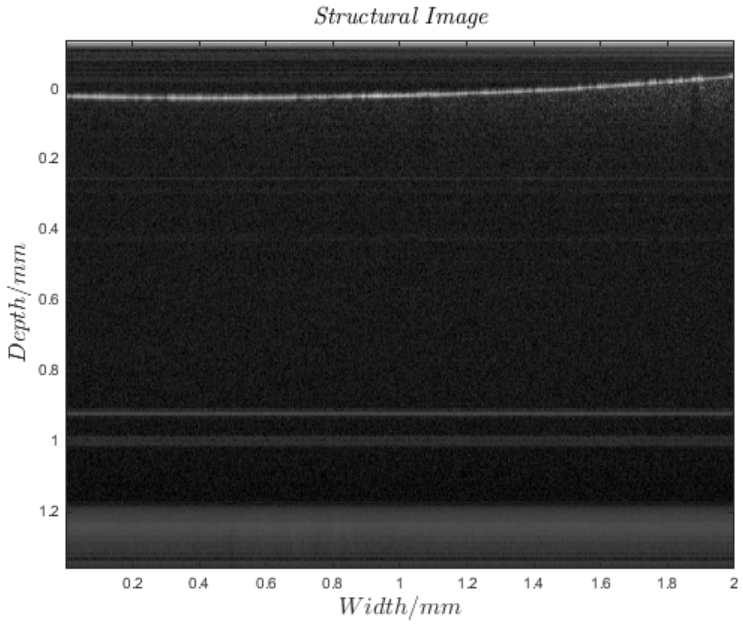

(a) Structural B scan image of the SPIO/milk solution on the agar phantom surface.

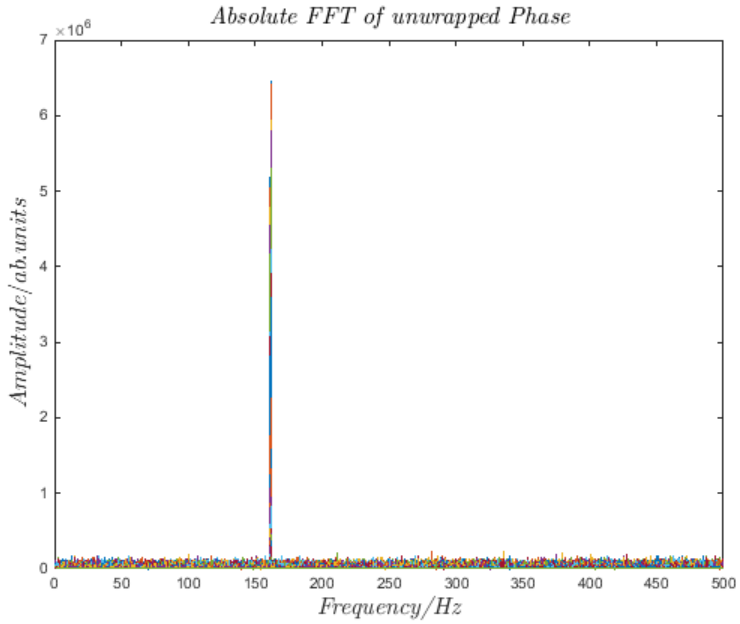

(b) FFT computed shows MMOCT signal at 160Hz as expected at double the f_B

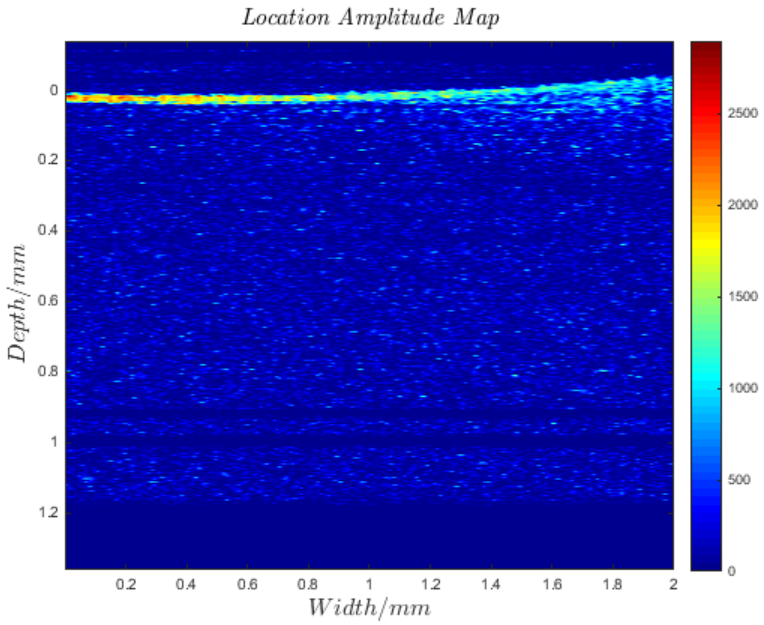

(c) Location map of the SPIO nanoparticles. The SPIO/milk layer has a higher displacement amplitude compared to the agar phantom.

Figure 3.11: The structural B scan and its corresponding SPIO nanoparticle location map for dried SPIO/milk of concentration $83\mu g/ml$.

3.6 Cornea Imaging

This experimentation was the main aim of the project, to be able to embed SPIO nanoparticles within rLEC and successfully transplant these loaded cells onto a cornea ex vivo. Then locate the loaded cells on the cornea using our ultra-high resolution SDOCT in combination with the MMOCT set up. This may play a major role in the future development of stem cell treatment for LSCD, where the stem cells to be transplanted can be labelled with SPIOs and tracked using MMOCT system.

3.6.1 Method

Initially a million cells were transplanted on to the cornea. After the success of this, the cell number was reduced to 250,000 followed by 100,000. These reductions in the number of cells transplanted was to assess the sensitivity of the system and to highlight any signal dependence on the population size of the transplanted embedded cells. The data processing of the rLEC experiment is the same as was done for the agar experiments. However, here the corneas also have to be prepared. The rabbit's eye globe is dissected to leave behind the anterior button (i.e. the cornea surrounded by 2-3 mm of sclera). The vitreous humour and the lens are removed. The reason for dissecting the eye globe is for ease of imaging. The eye globe has a small radius of curvature and the SNR falls off rapidly with lateral position. Dissecting flattens the cornea and decreases the sensitivity fall off. With the cornea button prepared the cells with the embedded SPIO nanaparticles can be transplanted onto the cornea. For this process a cylindrical ring was placed onto the cornea button. After calculating how much media/cells to draw from the incubation flask, this volume is drawn and pipetted into the hollow cylinder onto the cornea. The cylinder is used to contain the cell solution on the cornea and prevent it from running off. This allows the transplanted cells to anchor onto the cornea. The cylinder is made of stainless steel

with an inner bore area of 78.5 mm^2. As the cylinder is made of stainless steel it was left in place on the cornea during imaging. The SPIO embedded cells are allowed 1 hour to anchor to the cornea epithelium before imaging.

Figure 3.12: Cornea button prepared for imaging (left) and stainless steel ring placed on top of cornea to contain the cells embedded with SPIO nanoparticle.

3.6.2 Results

The areas with the high intensities have greater displacements at 160Hz. It is clear that the higher displacements are seen on the epithelium where the rLEC with the embedded SPIOs are transplanted. Figure 3.13 illustrates the results for different cell seeding densities are used. Initially a million cells are transplanted onto the cornea. This is a large number of cells but it also equates to a higher probability of success. This was followed by a transplantation of 2.50×10^5 cells and finally 1×10^5.

This result shows the 1×10^6 SPIO embedded cells transplanted onto the cornea. The top layer containing the transplanted cells embedded with SPIOs is distinguishable from the rest of the cornea. The number of cells seeded is too high as it has formed an opaque multi layer, this is evident in figure 3.13a where the stroma is not as clear as compared to figure 3.14a and figure 3.15a. The epithelium appears bright in the structural image but the stoma below is darkened from 0.4 to 1.5mm on the width axis. With this high density of loaded cells, a MMOCT signal was not needed to locate the region of SPIOS embedded cells. So the seeding number needs to be reduced and tested to see if the MMOCT system can still detected their location.

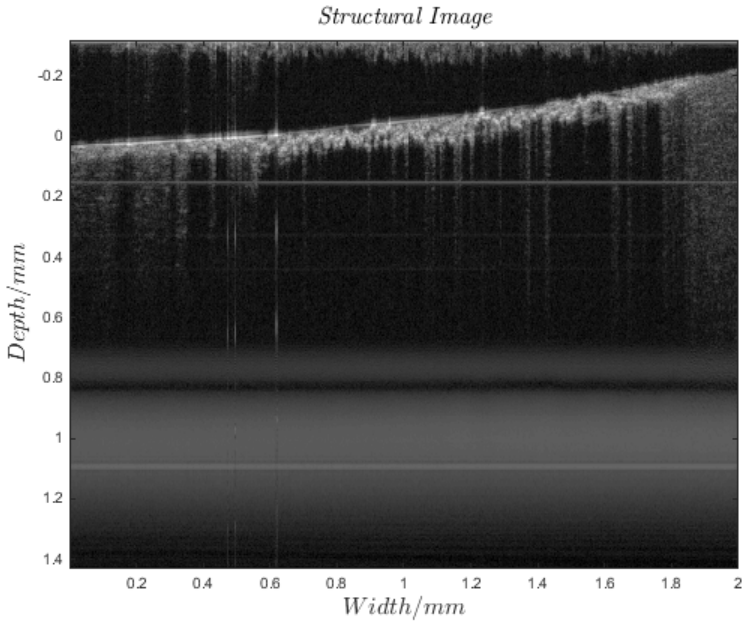

(a) Structural B scan image of the SPIO embedded cells on the cornea epithelium

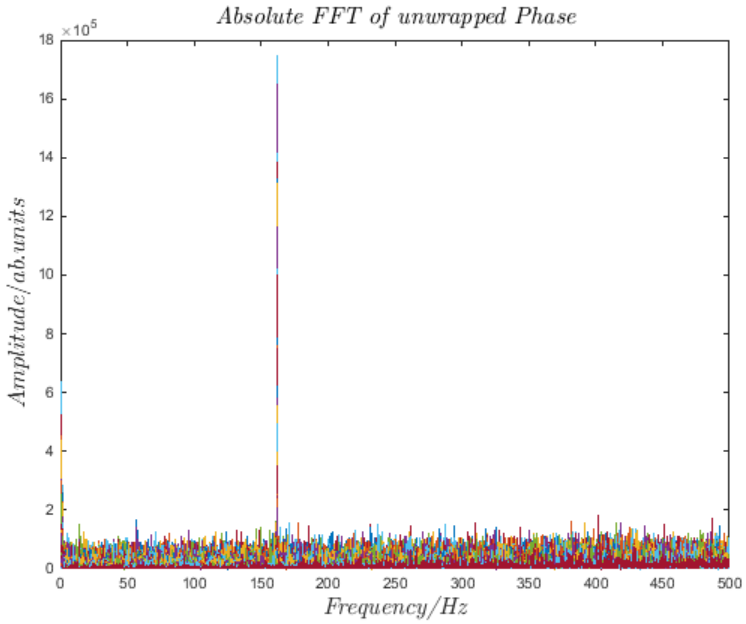

(b) FFT computed shows MMOCT signal at 160Hz as expected at double the field modulation frequency f_B=80Hz.

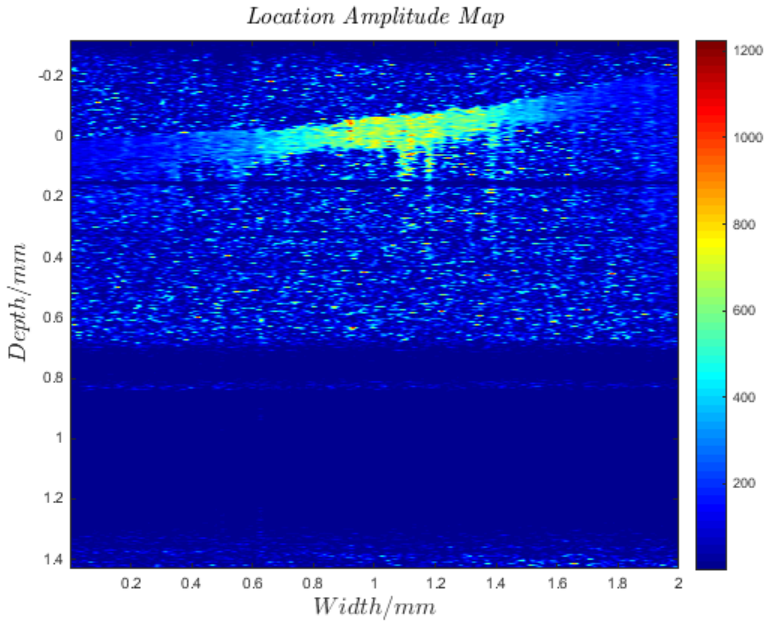

(c) Location map of the cells containing SPIO nanoparticles. The epithelium layer of the cornea has a higher displacement amplitude compared to lower layers

Figure 3.13: Shows the structural B scan and its corresponding SPIO nanoparticle location map for 1×10^6 cells (12732 cells/mm^2) embedded with SPIOs transplanted onto a cornea

The following results illustrates the MMOCT obtained from transplanting 2.50×10^5 cells embedded with SPIO nanoparticles on a rabbit cornea. We do obtain a MMOCT signal at double the f_B. However, we also see a signal at 80Hz and higher harmonics, the required signal at 160Hz is the most dominant.

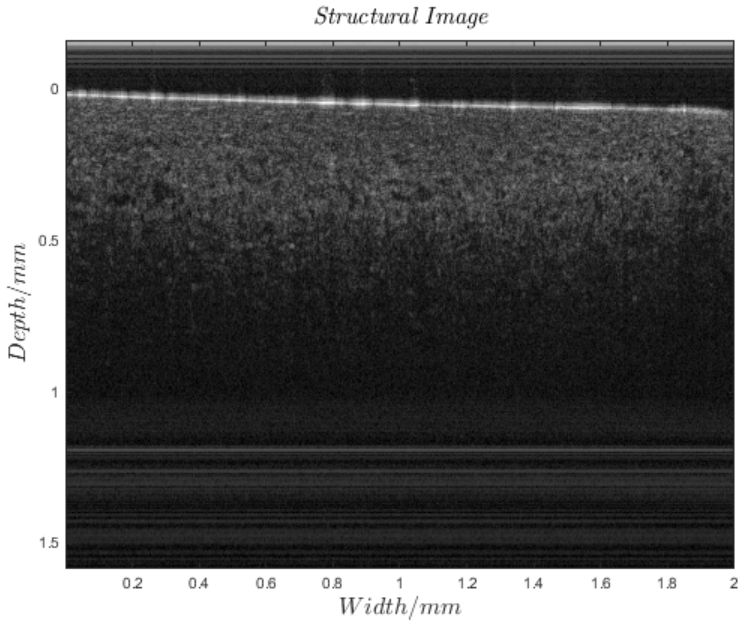

(a) Structural B scan image of the SPIO embedded cells on the cornea epithelium

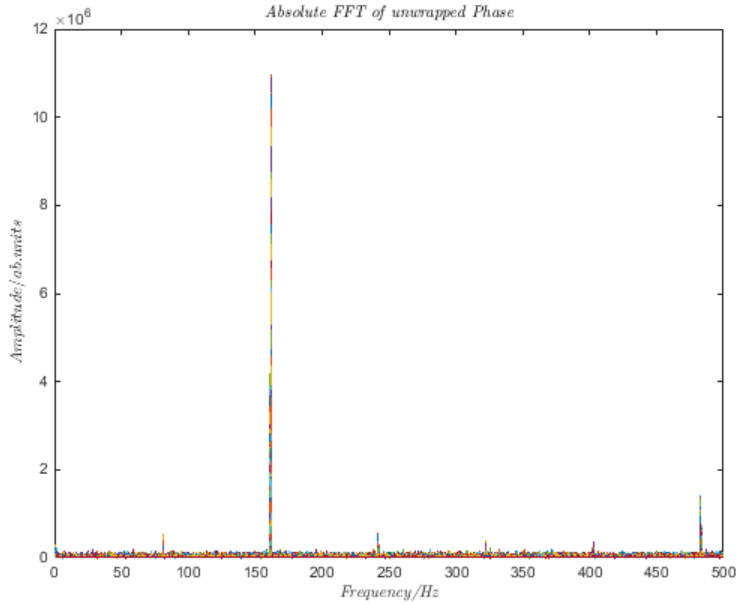

(b) FFT computed shows MMOCT signal at 160Hz as expected at double the f_B=80Hz.

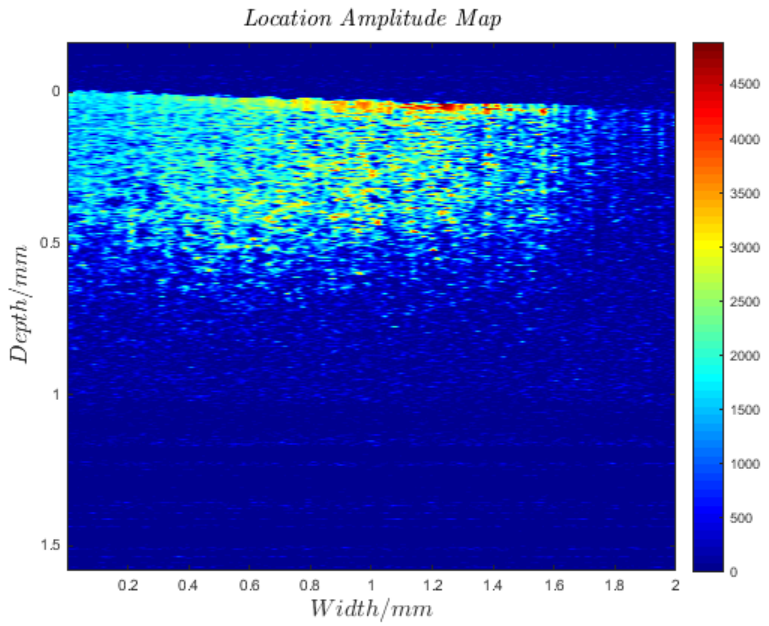

(c) Location map of the cells containing the SPIO nanoparticles. The epithelium layer of the cornea has a higher displacement amplitude compared to lower layers

Figure 3.14: Shows the structural B scan and its corresponding SPIO nanoparticle location map for 2.50×10^5 cells (3183 cells/mm^2)embedded with SPIOs transplanted onto a cornea

Figure 3.15 shows the MMOCT obtained from transplanting 1.0×10^5 cells embedded with SPIO nanoparticles on a rabbit cornea. A strong signal is present at 160Hz but like figure 3.14 the 80Hz MMOCT signal is also present.

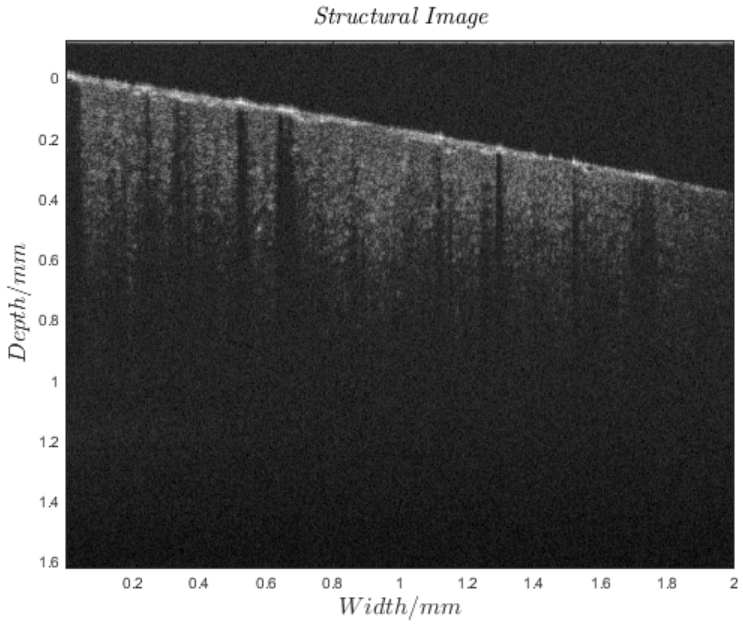

(a) Structural B scan image of the SPIO embedded cells on the cornea epithelium

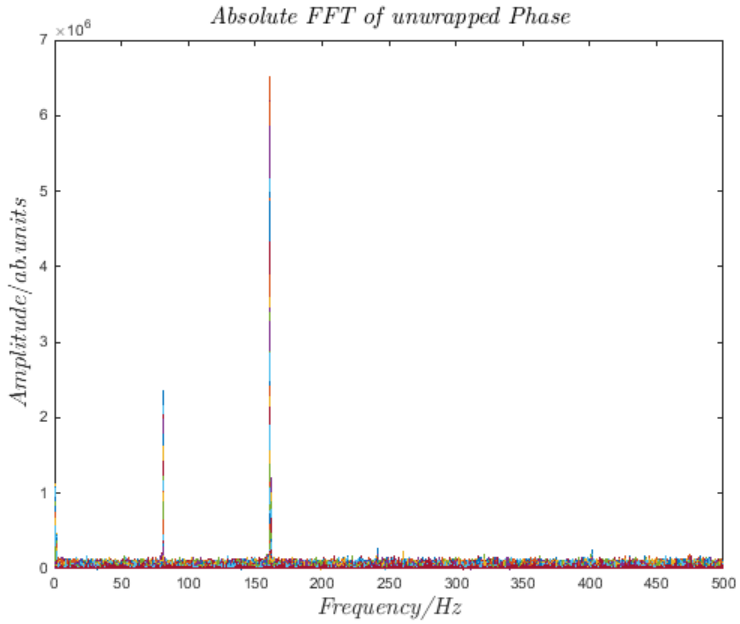

(b) FFT computed shows MMOCT signal at 160Hz as expected at double the f_B=80Hz.

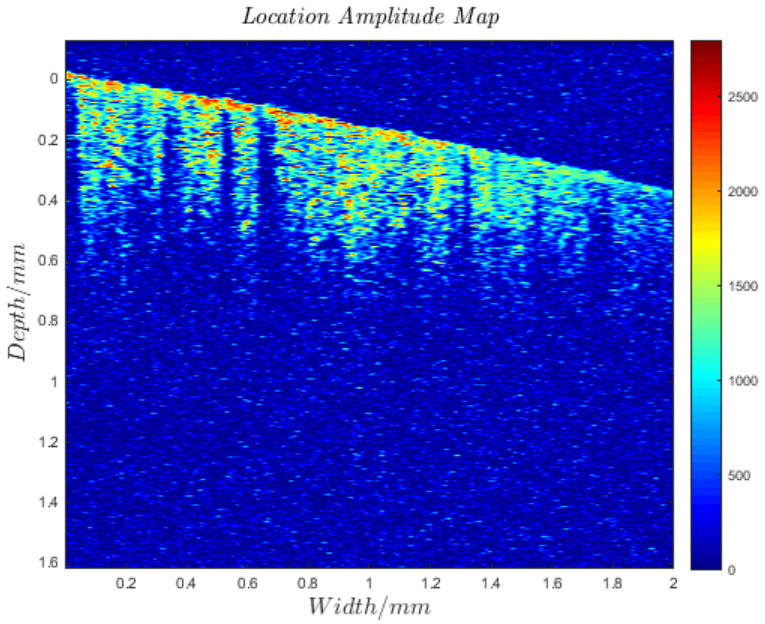

(c) Location map of the cells containing the SPIO nanoparticles. The epithelium layer of the cornea has a higher displacement amplitude compared to lower layers

Figure 3.15: Shows the structural B scan and its corresponding SPIO nanoparticle location map for 1×10^5 cells (1273 cells/mm^2) embedded with SPIOs transplanted onto a cornea

3.6.3 Discussion

Figure 3.14b and figure 3.15b does not only show signals at 160Hz but also at 80Hz and higher frequency harmonics. The reason for this is not totally clear. These harmonics maybe due to the environment in which the particular cells are in. Since even and odd harmonics can be produced by a mechanical response which varies non-linearly with the driving field. When comparing the STFT location amplitude maps figure 3.14c and figure 3.15c to the high cell density sample figure 3.13c; it is noticeable that for figure 3.14c and figure 3.15c the MMOCT signal is present in not only the epithelium layer but also in the stroma. A possible reason for the presence of MMOCT signal in the rest of the cornea could be due to the rLEC containing the SPIO nanoparticles migrating into the cornea, although a more probable explanation is the outward diffusion of SPIO nanoparticles from the transplanted cells into the remaining cornea. These hypotheses can be investigated by imaging the sample more frequently from the time of seeding the cells on the cornea surface. If this phenomenon is due to either the diffusion of the SPIO nanoparticles or the migration of the cells, the image dataset should show a gradually increasing MMOCT at depth with time. These hypotheses were not investigated due to time restrictions on funding.

3.7 Future Works

For future development it would be critical to both automate and synchronise the solenoid modulation at f_B with the acquisition of frames. Also it would be advantageous to sonicate the SPIO solution before incubating it with the cells for uptake and also before pipetting the SPIO/milk solution on the agar. The sonication will disperse the SPIOS, reducing aggregation and giving a more evenly dispersed MMOCT signal. However, the even after sonicating the SPIO solutions if not used straight away the SPIOs will aggregate again, so a better direction forwards would be to use dextran

coated SPIOs which has already been used in animal/human studies. The coating will reduce the nanoparticle aggregations.

Another aspect which can be improved is the introduction of wavelet transforms instead of STFT. The wavelet transforms have the resolution advantage over the STFT. The STFT requires a fixed window size and therefore the tradeoff between spatial and frequency resolution is fixed but the wavelet analysis allows for flexible windowing [7].

Another interesting aspect of the research with scope for further development is the cause of the multiple harmonics. With some samples there are no other frequencies other than at the expected second harmonic where as other have signal power at higher harmonics also. More interestingly the nanoparticles used are paragmagnetic and therefore should be displaced at twice the modulation frequency but some samples do exhibit oscillations at 80Hz.

References

[1] E. L. Madsen, M. A. Hobson, H. Shi, T. Varghese, and G. R. Frank, "Tissue-mimicking agar/gelatin materials for use in heterogeneous elastography phantoms," *Physics in medicine and biology*, vol. 50, no. 23, p. 5597, 2005.

[2] A. Oldenburg, F. Toublan, K. Suslick, A. Wei, and S. Boppart, "Magnetomotive contrast for in vivo optical coherence tomography," *Optics Express*, vol. 13, no. 17, p. 6597, 2005.

[3] J. Oh, M. D. Feldman, J. Kim, C. Condit, S. Emelianov, and T. E. Milner, "Detection of magnetic nanoparticles in tissue using magneto-motive ultrasound," *Nanotechnology*, vol. 17, no. 16, p. 4183, 2006.

[4] X.-M. Zhu, Y.-X. J. Wang, K. C.-F. Leung, S.-F. Lee, F. Zhao, D.-W. Wang, J. M. Lai, C. Wan, C. H. Cheng, and A. T. Ahuja, "Enhanced cellular uptake of aminosilane-coated superparamagnetic iron oxide nanoparticles in mammalian cell lines," *International journal of nanomedicine*, vol. 7, p. 953, 2012.

[5] S. Saito, M. Tsugeno, D. Koto, Y. Mori, Y. Yoshioka, S. Nohara, and K. Murase, "Impact of surface coating and particle size on the uptake of small and ultrasmall superparamagnetic iron oxide nanoparticles by macrophages," *International journal of nanomedicine*, vol. 7, p. 5415, 2012.

[6] G. Lamouche, B. F. Kennedy, K. M. Kennedy, C.-E. Bisaillon, A. Curatolo, G. Campbell, V. Pazos, and D. D. Sampson, "Review of tissue simulating phantoms with controllable optical, mechanical and structural properties for use in

optical coherence tomography," *Biomedical optics express*, vol. 3, no. 6, pp. 1381–1398, 2012.

[7] Y. Zhang, Z. Guo, W. Wang, S. He, T. Lee, and M. Loew, "A comparison of the wavelet and short-time fourier transforms for doppler spectral analysis," *Medical engineering & physics*, vol. 25, no. 7, p. 547, 2003.

Chapter 4

Oral Mucosal Imaging

4.1 Summary

Optical coherence tomography is now the gold standard technique for retinal screening and is emerging rapidly in cardiovascular research however it remains a research goal to establish it to the same degree in epithelial cancer detection and diagnosis. In this chapter we compare two different OCT systems: an 890 nm spectrometer-based OCT system with 2.5 μm axial resolution and a 1300 nm swept-source OCT system with 7.5 μm axial resolution to determine the effect of these different OCT parameters on the endogenous backscatter contrast of dysplastic/malignant oral mucosa models relative to normal mucosa models. Tissue- engineered oral mucosa models constructed with a dysplastic cell line (DOK), a malignant cell line (Cal27) and normal cell were imaged with both of these OCT platforms and comparisons made with regard to apparent epithelial thickness and the visibility of the epithelium relative to the underlying stroma. For the Cal27s, hematoxylin and eosin staining confirmed the formation of a keratinized layer superficial to a thickened layer of viable cells on top of the stroma. The keratinized layer presented as a hyper-reflective thickened layer superficial to a darker region on both OCT platforms. The keratinized layer caused a steep fall in signal at 890 nm, making it difficult to visualise underlying

structures, whereas 1300 nm OCT clearly visualized both the epithelial cells and the stroma lying beneath. For the DOK cells, hematoxylin and eosin staining confirmed the formation of an epithelial layer frequently presenting an abnormal morphology especially at the epidermal/stromal junction, with features such as infiltrating, bulbous rete pegs. These were more clearly visualized under 890 nm OCT. These observations show that 890 nm OCT retains some of its known advantages of higher contrast between anatomical tissue layers when used to observe dysplastic and malignant 3D oral mucosa constructs. However, 1300 nm OCT is confirmed to possess a greater ability to image the full thickness of the model epithelia and in particular it is more suited to imaging through the keratinized layer.

4.2 Introduction

The work in this chapter has been published in the Modern Technologies in Medicine Journal [1].

Optical Coherence Tomography in the medical field was originally used in ophthalmology. It is now the gold standard technique for retinal screening. However, its applications in the screening of superficial cancers is now becoming a focus in research. Using OCT to image cancerous tissues at depths can be very challenging due to the scattering nature of tissues. The highly scattering tissue layers limits the imaging depth of the OCT. However, this is not such a disadvantage in epithelial cancer detection since generally the epithelium is only a few hundred microns in thickness. In this chapter we compare two different OCT modalities: the Ultrahigh resolution 890 nm spectral domain (SD) OCT system and a commercial 1300 nm swept-source (SS) OCT system. The 890nm SDOCT as described in the chapter "Ultra High Resolution Spectral Domain OCT (UHR-SDOCT) for corneal imaging" has an axial resolution of 2.5 μm in air whilst the commercial 1300nm SSOCT has an axial resolution of 7.5 μm in air. In the chapter histology images are used to

show the morphological changes between the normal, dysplastic and carcinoma models. Histology is the gold standard for determining the abnormalities in the cell's nuclear morphology, a recognised marker for dysplastic changes [2] [3]. OCT is used to establish the gross cellular structure and the extent of the tumour. It known that OCT systems with light sources producing a central wavelength below 1 μm and a bandwidth larger than 150 nm will have an advantage in terms of axial resolution. However, systems with central wavelength greater than 1 μm usually 1300nm provide better depth penetration due to the lower attenuation at the longer wavelengths. In this study we compare the OCT presentation of three tissue-engineered oral mucosa models using an 890 nm SLD-based spectrometer system and a commercial 4-beam swept-source system operating at 1300 nm. The aim in this experimentation was to determine the effect of different central wavelengths and axial resolution on the endogenous backscatter contrast of dysplastic/malignant oral mucosa models relative to normal mucosa models. This experiment will also allow us a direct comparison of the in-house UHROCT system to a commercial used system.

4.3 Method

For the experimentations oral mucosa models were constructed from dysplastic cell line (DOK), a malignant cell line (Cal27) and normal cells. These models were then imaged using both of these OCT modalities and a comparison made between their measurements of the epithelial thickness and the overall visibility of the epithelium relative to the stroma.

4.3.1 1300nm SSOCT

The 1300 nm swept source (laser sweeps through wavelength band) OCT system(EX1301, Michelson Diagnostics Ltd., UK) is a multi-beam set-up with four independently focused sample beams. The swept source laser used is the HSL-2000-10 by (Santec, Inc.,Japan). The source provides a centre wavelength of approximately 1300 nm with an approximate bandwidth of 150 nm. The 1300 nm system produces B scans of the samples at a rate of 10,000 A scans per second. The system is also capable of acquiring B scans comprising of different number of A scans. The 890 nm system has a maximum lateral scan distance of 4mm whilst the 1300 nm system's lateral scan distance can cover up to 6mm. In this experiment a lateral scan distance of 4mm was used for both systems. The axial resolution of the SSOCT as measured in air is 7.5 μm and a lateral resolution of 7.5 μm also. In the study B scans acquired comprised of 952 A-scans over a lateral distance of 4mm. Acquisition was at a rate of 5 frames per second. The EX1301 has a stitching algorithm which combines the best focused regions from the four independently focused beams to form a composite image with a two-fold lateral resolution improvement as compared to a single beam imaging the same region [4]. This system is a good standard to compare the 890nm in-house system to because the 1300nm system has been used in clinical setting to identify malignant oral mucosa biopsy samples. The system achieved a sensitivity (ratio of correctly detected positives to total number of positives)of 85% and specificity (ratio of correctly detected negatives to total number of negatives) of 78% when used to image biopsy samples in an immediate ex vivo study [5].

4.3.2 890nm UHR-OCT

The 890 nm system used for imaging oral mucosa models is a custom-built ultra-high resolution spectral domain optical coherence tomography system. A dual super

luminescent diode source (Broadlighter D890-HP, Superlum, Ireland) emits a central wavelength of 890 nm and a bandwidth of 150 nm into the single mode fibre based system. The details of the set up and imaging parameters are recorded in section 2.5.

4.3.3 Tissue Models Preparation

The tissue preparation was conducted by colleagues John Fernandes and S Mittar, PhD and the histology images were provided and used with the permission of Vanessa Hearnden, PhD. The experiments were supervised by S. MacNeil, M.H. Thornhill, C. Murdoch, PhD, K.D. Hunter, PhD and S.J. Matcher.

The group led by Prof. Sheila MacNeil have successfully developed 3D models of healthy human oral buccal mucosa for clinical applications. The model consisting of a base of connective tissue with an upper epithelium layer has been used as replacement for scar tissue in the urethra [6]. A similar process is used to build the dysplasia and carcinoma models but the healthy oral keratinocytes are replaced with dysplastic and malignant cell lines respectively. All the work to generate the tissue models were carried out in sterile condition in class(II) laminar flow tissue cabinets (Walker Safety Cabinets, UK). During tissue culturing the cells were kept in humidified incubators at 37^oC containing 5% CO_2. The tissue models were cultured on an acellular skin scaffold processed from glycerol treated cadaveric skin purchased from Euroskin Bank (Beverwijk, the Netherlands). To preserve the skin until it is used, it was stored in glycerol and kept at 4^oC. Before use the models were washed in sterile phosphate buffer solution repeatedly to remove the glycerol and then incubated in 1M sodium chloride for 1 day. The epidermis from the skin was removed, producing a de-epithelialised dermis (DED). The remaining DED was used as scaffold for tissue engineered oral mucosa models. The DED was dissected into 1.5 by 1.5 cm squares and placed into a 6 well plate. The cylindrical rings are placed on top of

the DED, the rings have some weight to them so it settles into the DED forming a liquid tight seal between the bottom of the ring (in contact with the DED) and the DED. Both Normal Oral Keratinocytes (NOK) and Normal Oral Fibroblasts (NOF) were isolated from waste tissue collected during routine oral surgery (Ethics reference 09/H1308/66) as described by Colley [7]. They were then seeded into the cylindrical ring wells at a ratio of 3:1 ratio. The ring has a 1 cm diameter and a height of 1 cm, hence, seeding 300,000 NOK to 100,000 NOF in Greens media. After 48 hours, the seeding the composites are elevated to air /liquid interface using square stainless steel grids. The composites are then cultured for another 7, 14 and 21 days. To produce the abnormal mucosal models, the Cal27 oral squamous cell carcinoma and the DOK pre invasive cell lines were used. The process for producing these were identical to that used for the normal mucosal models, however, only 250,000 cells of each type were used along with the 100,000 NOF. Each model was grown in media associated with the cell line used. The Cal27, derived from the tongue is an oral squamous cell carcinoma human cell line was cultured in DMEM with 10% FCS. The Cal27 cells used was purchased from ATCC (Manassas, VA, USA). The Dysplastic Oral Keratinocytes (DOK, ECACC 94122104) were acquired from the European Collection of Cell Culture (ECACC) via Sigma Aldrich (Dorset, UK). The DOK cell line was obtained from a tongue lesion. The lesion next to oral squamous cell carcinoma exhibited mild to moderate dysplasia. The DOK cells were also cultured in DMEM with 10% FCS supplemented with hydrocortisone (5 $\mu g/ml$). The abnormal models were also cultured for 7, 14, and 21 days.

4.4 Results

4.4.1 Oral mucosa models histological assessment

During the development of the models it was observed that the thickness of the epithelium and the degree of stratification is dependent on the duration the models are cultured at an air/liquid interface for [7] [8].

Culturing the tissue engineered oral mucosa at an air liquid interface produces a stratified epithelium after 7 days in culture figure 4.1. The epithelium is 10 cell layer thick by the 21st day and displays signs of organisation and differentiation. Over time in culture, the model becomes more organised and the epithelium becomes thicker. Comparing the hematoxylin and eosin (H&E) stained histology sections it is apparent that there are similarities between the tissue-engineered model and the human biopsy figure 4.2. One main similarity is the differentiation pattern observed in-vivo is also observed in the tissue engineered oral mucosa.

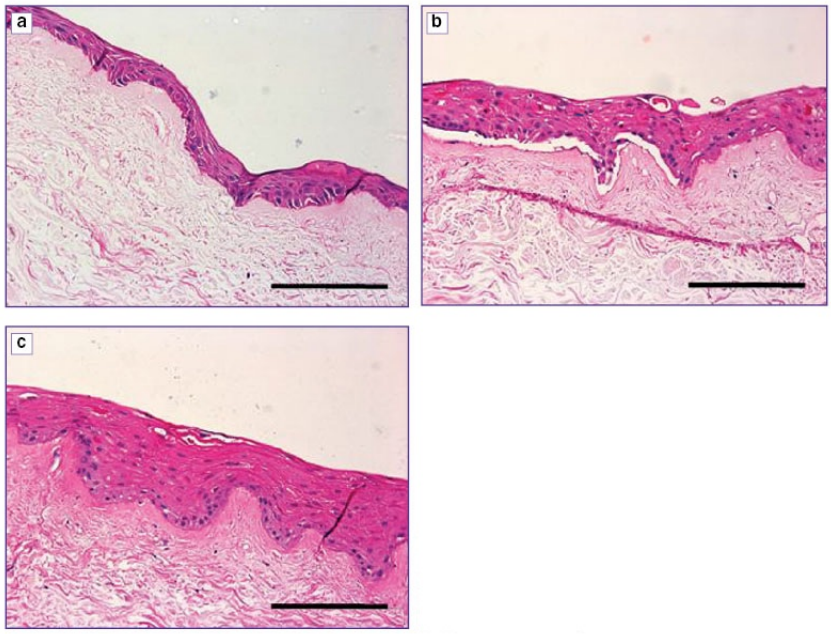

Figure 4.1: H&E stained histology of normal tissue-engineered oral mucosa over 7 (a), 14 (b) and 21 (c) days of culture at an air/liquid interface. Reproduced with permission from Hearnden [8]. Scale bar: 100 μm

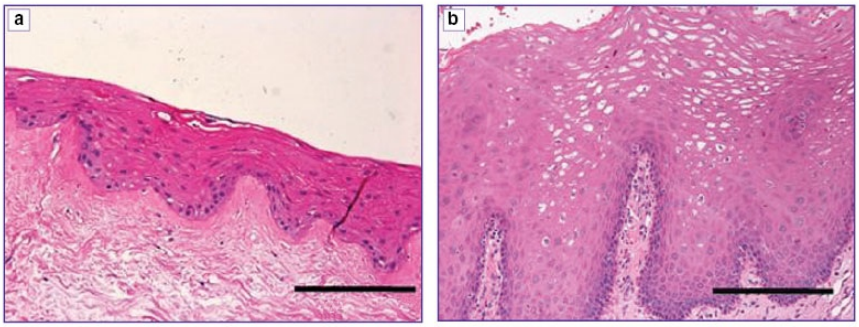

Figure 4.2: H&E stained histological comparison of the normal TEOM (a) with an in vivo biopsy of healthy oral mucosa (b). Reproduced from Hearnden [8] with permission. Scale bar: 100 μm

The basal cells in the basal layer of the epithelium have a high density of nuclei. As the cells begin to differentiate their nuclei are more dispersed, this can be seen in the supra-basal cells. They are larger and their nuclei are more dispersed. Layers at the surface contain cells which are flattened with very dispersed nuclei. These superficial cells are terminally differentiated and produce the smooth flat surface of the epithelium. Both sets of samples, the human biopsy and the tissue engineered oral mucosa (TEOM) have rete ridges, the characteristic rounded extensions protruding into the epithelial connective tissue and forms the epithelial connective tissue junction.

It is noticeable that intracellular signalling plays a part in the evolution of the epithelium because the cells of the epithelium differentiate in strata and not individually.

4.4.1.0.1 DOK model

Below Figure 4.3(a)(f) shows the stages of development of the 3D tissue engineered models resulting from DOK cells cultured on an acellular skin scaffold. DOK cells begin to form an epithelium layer of thickness 2-10 cells by the 7th day of culturing at air/liquid interface. In some areas there are signs that cells have not been able to differentiate into strata and various areas show signs of cell death. After culturing for 14 days the thickness of the epithelium has increased compared to the previous measurement at day 7. The measurement was done taken 2D B scans using OCT, where the epithelium can be distinguished from surrounding tissue due to the difference in refractive indices. The thickness is then measured from the image using ImageJ version 1.47. The epithelium strata is now showing signs of organising themselves. Some of the superficial cells are becoming flattened and their neighbouring connective tissue are starting to organise into a pattern seen in normal epithelia. There are also signs of dysplasia where individual cells are producing keratin instead of strata of cells and also nuclei pleomorphism is present throughout the epithelium (this can indicate severe dysplasia or carcinoma). Significant cytological structural abnormalities are observed in the basal layer which commonly indicates carcinomas (highlighted region

of figure 4.3 (d)). A severe dysplastic and carcinoma appearance alongside cytological and structural abnormalities throughout the epithelium are apparent by day 21. The abnormalities include: rete pegs which are extensions into the connective tissue and keratin pearls which are circular formations of keratin(stained pink by H&E) in the middle of the epithelium. There are regions of cells within the stroma which have the appearance of epithelial cell invading the stroma. The alien cells appear different to fibroblasts in the connective tissue as fibroblasts tend not to cluster in a group as the cells seen in these models do and there is hematoxylin staining around the cells (not seen for the fibroblasts).

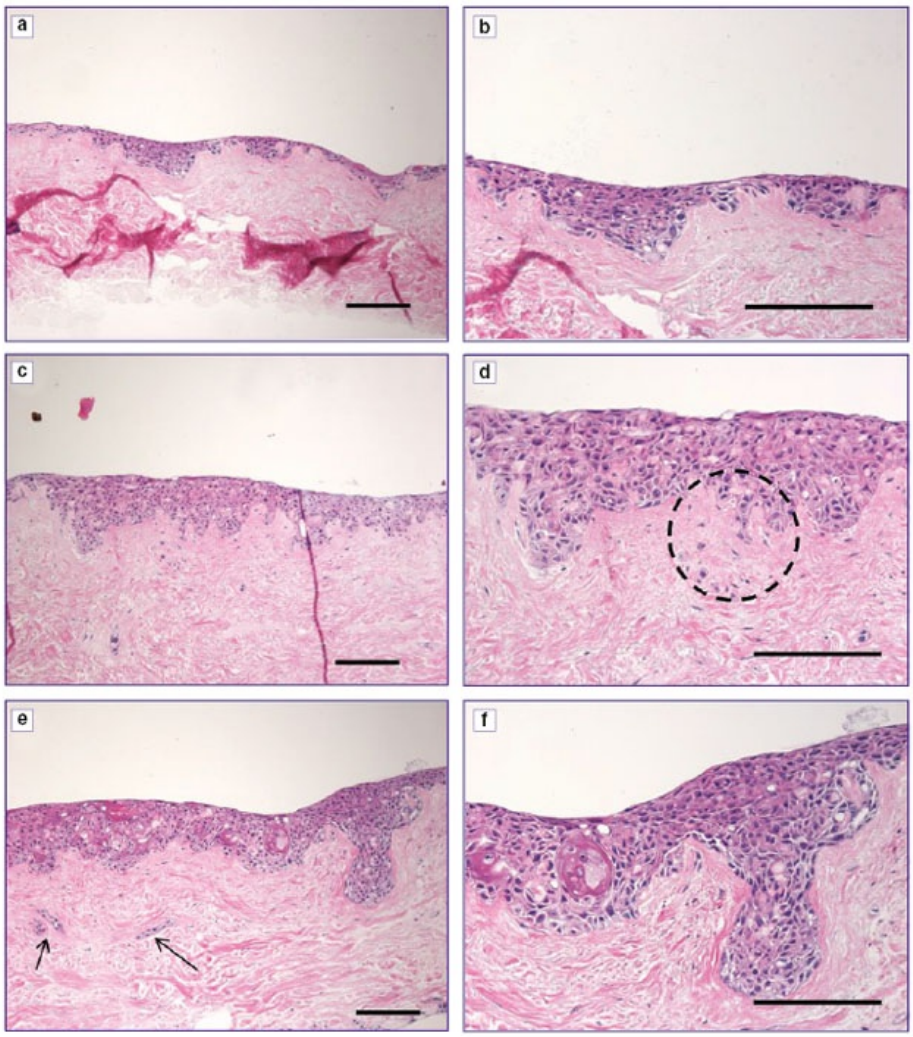

Figure 4.3: H&E stained histological sections of the DOK cell line cultured in three dimensions on DED. Models were grown at an air/liquid interface for 7 days ×10 magnification (a) and ×20 magnification (b); 14 days ×10 magnification (c) and ×20 magnification (d) or 21 days ×10 magnification (e) and × 20 magnification (f). Highlighted circle (d) shows invading cells. Arrows (e) show invaded tumour islands. Scale bar: 200 μm (n=3). Reproduced from Hearnden [8] with permission

4.4.1.0.2 CAL model

Figure 4.4 shows CAL27 model these are most comparable in appearance to that of clinical dysplasia and carcinoma. Within 7 days in culture the epithelium is observed to be differentiated with well defined basal cell layer. The differentiation takes place in regions and strata of the epithelium rather than in isolated cells indicating some cell-cell interactions. Islands of epithelial cell are found within the connective tissue suggesting invasion of the oral squamous cell carcinoma into the connective tissue.

The models cultured for 14 days appear highly keratinised on the surface. This high level of keratinisation is also commonly seen on the surface of dysplastic tissues clinically. Figure 4.4(c) shows the organised differentiation remaining in areas however, in other places this is disrupted by the extensive keratinisation. After 21 days in culture the appearance of the histology is less like dysplastic lesions seen clinically as cells begin to grow over the top of the keratinised areas and the differentiation is mostly lost. This model has the appearance of a squamous cell carcinoma in situ with some signs of invasion as early as 7 days at air/liquid interface.

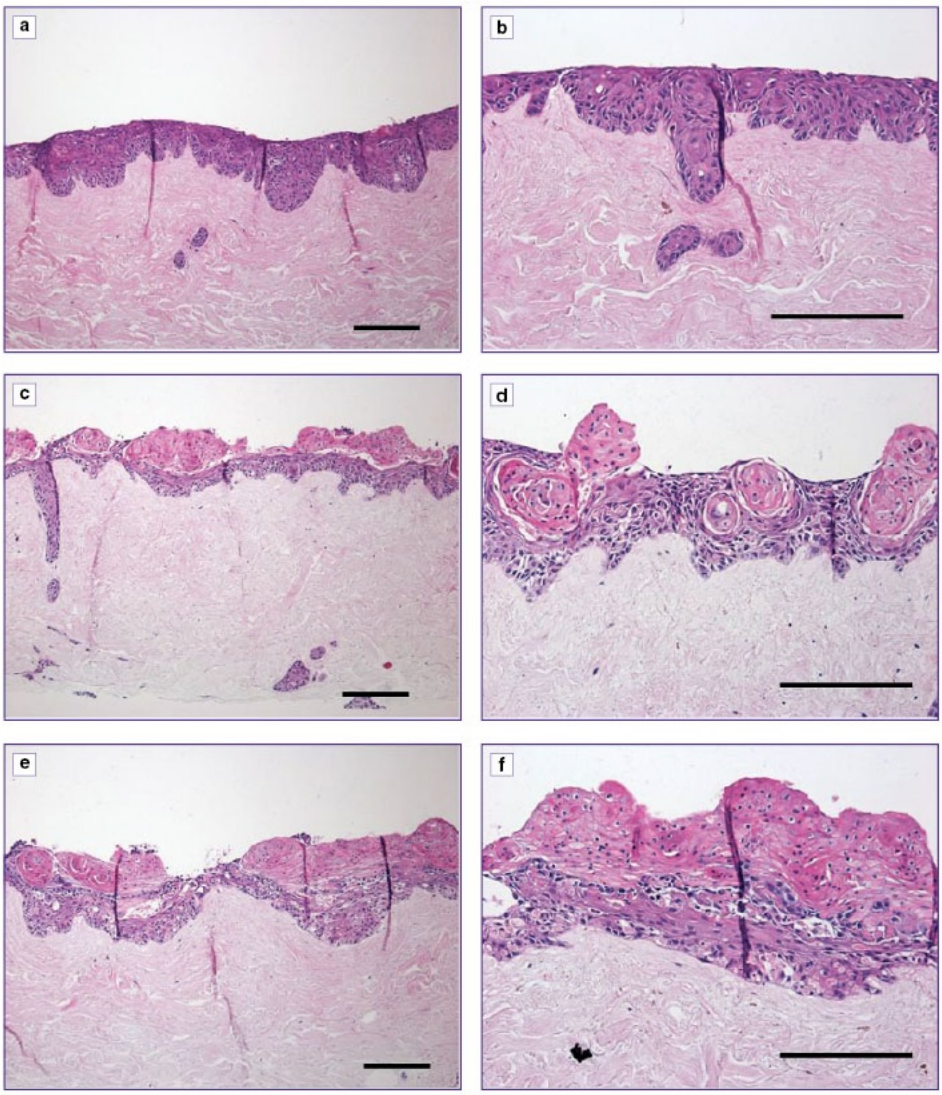

Figure 4.4: H&E stained histological sections of the Cal27 cell line cultured in three dimensions on DED. Models were grown at an air liquid interface for 7 days ×10 magnification (a) and ×20 magnification (b); 14 days ×10 magnification (c) and ×20 magnification (d) or 21 days ×10 magnification (e) and ×20 magnification (f). Scale bar: 200 μm (n=3). Reproduced from Hearnden [8] with permission

4.4.2 Oral mucosa models OCT presentation at 890 and 1300 nm

.

Figure 4.5 shows OCT two dimensional B-scans collected on the normal, dysplastic and carcinoma oral mucosa models at day 21. It is evident that the 890 nm images in general appear darker and have a greater roll-off in sensitivity with depth compared to the 1300 nm images. This may be inherent from the different system parameters, however, it is obvious from comparing image figure 4.5(c) with figure 4.5(f) that there is also a better contrast between the tissue-engineered epithelium and the DED when imaging at 890nm and with 2.5μm axial depth resolution compared with imaging at 1300nm. For this study this improvement in axial resolution means there is a better ability to infer the epithelial thickness and, for the DOK model shown in figure 4.5(c) there is a clearer ability to resolve morphological abnormalities such as infiltrating, drop shaped rete pegs similar to those shown by histology in figure 4.3.

For the Cal27 models we see an inversion of the usual contrast pattern for OCT images of epithelium, with the most superficial band appearing brighter than the underlying layers. With the in house-built 890nm system the superficial layer is significantly brighter than the corresponding layer in the normal model and displays a sharp, irregular lower border indicative of strong contrast between this layer and the underlying material. Even fainter signal is visible below this underlying layer, particularly towards the image centre. Based on our previous experience with OCT imaging of tissue-engineered skin [9], we consider that a plausible interpretation of the Cal27 images is that the brighter superficial region represents keratinized tissue overlying the metabolically active dysplastic epithelial cells (which generally present more darkly than stroma in OCT images). Such keratinization is a late-stage feature of the Cal27 models as seen in figure 4.4 as well as being a common clinical feature of dysplastic oral lesions. There are small dark infiltrations at the surface of model

(especially clear on the 890 nm image), which may be areas of nascent epithelial cell overgrowth. The weak signal seen deep in the Cal27 model may be the remnants of signal from the underlying DED, which is now deep below both the keratinized superficial layer and a thickened layer of epithelial cells. The DOK construct was imaged at day 21. 573 slices were acquired, each 4 mm wide and with 5 micron slice spacing. Data was collected sequentially on the two systems. Fiducial markers were placed on the epithelia surface of the construct, to facilitate the approximate registration of the two data sets. It is clear that the 1300 nm image shows more signal from deeper regions of the stroma whereas the 890 nm image more clearly demarcates the epithelial thickness, epidermal/stromal junction and epidermal infiltrations into the stroma.

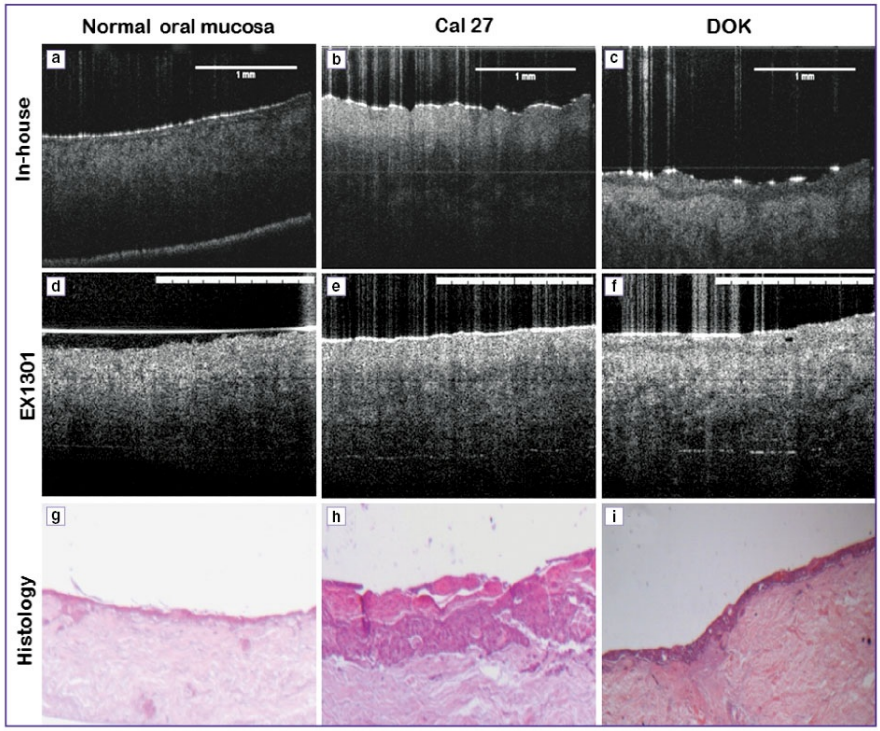

Figure 4.5: Three oral mucosa models imaged using 890 nm (upper row) and 1300 nm OCT (middle row). Scale bar: 1 mm. Contemporary histology shown on the lower row

4.5 Conclusions

It is evident that the 890nm and the 1300nm OCT systems give different levels of contrast between the epithelium and the stroma in both the normal and dysplastic models. The general trend appears to be that the 890nm house built system shows greater contrast between different layers, for the normal and DOK models we see higher contrast at the epithelium/stroma boundary and for the carcinoma models(CAL27) we see the higher contrast at the keratinized/epithelium/ stroma boundaries. Due to the low attenuation at the higher wavelength, the 1300nm system shows a better depth penetration and a more uniform contrast across the imaging depth. This is explained by the scattering coefficient been proportional to λ^4 This is in agreement with earlier in vivo studies on normal human skin [10].

This study has shown that the UHROCT is comparable to the commercially available system in imaging biological scattering tissues. The system performs as well and even provides better contrast so can also be used to classify normal tissues from dysplastic and carcinoma tissues. The study also shows the potential for dual wavelength imaging as a route to improve the imaging of oral lesions, the 890nm channel providing the axial resolution to reveal morphological irregularities and the 1300nm channel providing improved sensitivity to structures at depth including vasculature [11].

References

[1] F. J. Boadi J. *et al.*, "Imaging of 3d tissue-engineered models of oral cancer using 890 and 1300 nm optical coherence tomography," *Sovremennye Tehnologii v Medicine 7(1): 6068*, 2015.

[2] T. Collier, A. Lacy, R. Richards-Kortum, A. Malpica, and M. Follen, "Near real-time confocal microscopy of amelanotic tissue: detection of dysplasia in ex vivo cervical tissue," *Academic radiology*, vol. 9, no. 5, pp. 504–512, 2002.

[3] A. Hoffman, M. Goetz, M. Vieth, P. Galle, M. Neurath, and R. Kiesslich, "Confocal laser endomicroscopy: technical status and current indications.," *Endoscopy*, vol. 38, no. 12, pp. 1275–1283, 2006.

[4] J. Holmes, "In vivo real-time optical coherence tomography imaging of drosophila for cardiovascular research," *Nature Methods*, vol. 6, no. 10, 2009.

[5] Z. Hamdoon, W. Jerjes, T. Upile, G. McKenzie, A. Jay, and C. Hopper, "Optical coherence tomography in the assessment of suspicious oral lesions: an immediate ex vivo study," *Photodiagnosis and Photodynamic therapy*, vol. 10, no. 1, pp. 17–27, 2013.

[6] S. Bhargava, J. M. Patterson, R. D. Inman, S. MacNeil, and C. R. Chapple, "Tissue-engineered buccal mucosa urethroplastyclinical outcomes," *European urology*, vol. 53, no. 6, pp. 1263–1271, 2008.

[7] H. Colley, V. Hearnden, A. Jones, P. Weinreb, S. Violette, S. MacNeil, M. Thornhill, and C. Murdoch, "Development of tissue-engineered models of oral dyspla-

sia and early invasive oral squamous cell carcinoma," *British journal of cancer*, vol. 105, no. 10, pp. 1582–1592, 2011.

[8] V. Hearnden, *Developing tissue engineered models of oral mucosa and oral cancer to study novel therapeutic and diagnostic techniques.* PhD thesis, 2010.

[9] L. E. Smith, V. Hearnden, Z. Lu, R. Smallwood, K. D. Hunter, S. J. Matcher, M. H. Thornhill, C. Murdoch, and S. MacNeil, "Evaluating the use of optical coherence tomography for the detection of epithelial cancers inā vitro," *Journal of biomedical optics*, vol. 16, no. 11, pp. 116015–1160158, 2011.

[10] A. Alex, B. Považay, B. Hofer, S. Popov, C. Glittenberg, S. Binder, and W. Drexler, "Multispectral in vivo three-dimensional optical coherence tomography of human skin," *Journal of biomedical optics*, vol. 15, no. 2, pp. 026025–026025, 2010.

[11] J. Enfield, E. Jonathan, and M. Leahy, "In vivo imaging of the microcirculation of the volar forearm using correlation mapping optical coherence tomography (cmoct)," *Biomedical optics express*, vol. 2, no. 5, pp. 1184–1193, 2011.

Chapter 5

Differential epidermal thinning of human forearm volar skin after steroidal and non steroidal treatments

5.1 Summary

In this chapter we conduct a quantitative study on the effect of two commercially available topical creams for the treatment of eczema using a 1300 nm central wavelength optical coherence tomography system. In the study we compare Betamethasone valerate a corticosteroid with Tacrolimus monohydrate a non-steroidal anti-inflammatory drug using a left/right comparison of epidermal thickness of the volar forearm skin on selected volunteers at baseline and after 14 days of treatment. We observed in 3 out of 4 volunteers that the use of corticosteroid results in the physical thinning of epidermis during a few weeks. It was also noted that in 3 out of the 4 volunteers Tacrolimus produced no physical changes in the epidermal thickness, however 1 out of the 4 volunteers showed evidence of the epidermis actually thickening following the

application of Tacrolimus.

5.2 Introduction

The skin acts as a barrier layer to regulate against fluid loss and pathogen invasion. The barrier function is most prominent in the most superficial layer of the skin: the stratum corneum. The stratum corneum is composed of keratinized corneocytes which are physically bonded together by corneodesmosomes. The stratum corneum typically has a thickness of 15-20 layers, the thickness is maintained by desquamation (the removal of the superficial layer of the stratum corneum) and this is balanced by the constant production of keratinocytes in stratum basale [1]. It thought that the breakdown of these corneodesmosomes is a key factor in the initiation of barrier-degrading inflammatory condition such as atopic dermatitis. The breakdown can be due to degradatory proteases.

A strong link has been established between the loss-of-function mutations in the FLG gene and being predisposed to atopic dermatitis [2]. FLG encodes for the production of filaggrin, a protein that facilitates the formation of the skin barrier. The filaggrin protein aids the formation and maintenance of the barrier function through several aspects including the mediation of keratin intermediate filament production and as a source of water-binding amino acids in the stratum corneum. It is believed that a skin barrier dysfunction is a precursor to clinical atopic dermatitis [3]. This link was established whilst measuring the transepidermal water loss (TEWL) in children, the study showed that TEWL was higher for atopic dermatitis sufferers but not for sufferers of other allergic skin conditions [4]. The conclusion was that children suffering from atopic dermatitis had a higher TEWL. This led to the suggestion of treating atopic dermatitis with barrier enhancing emollient alongside, or possibly as a replacement for, topical corticosteroids. A study conducted by Wiren and colleagues showed that after treating lesions with Betamethasone Valerate the recurrence of eczema can be delayed by using a skin moisturiser [5]. There is a growing interest in the use of non-steroidal anti-inflammatory drugs and more specifically targeted anti-inflammatory agents such as the calcineurin inhibitors for the treatment of atopic

dermatitis [6]. Tacrolimus monohydrate used in our study is such a drug which has reached clinical usage (Protopic ®, Astellas Pharma). Another supporting reason for the use of Tacrolimus and other non-steroidal treatment is the low percentage of unwanted side effects such as atrophy and pigment alteration [7], experienced in comparison to when corticosteroids are used. It is therefore of great interest to quantitatively asses the effect such treatments have on the skin layer thickness. Due to it's micron resolution, optical coherence tomography (OCT) is used routinely in skin imaging in regards to the epidermis. In our study OCT is used to measure the thinning of epidermis and dermis, OCT is non invasive and has a high contrast to differentiate between the anatomical skin layers.

Previous investigations using OCT alone or along with US have been conducted to study the effects of topic corticosteroids on the skin thickness. One of the earliest studies, applied clobetasol proprionate 0.05% (potency class IV) for 3 weeks on a daily basis and the skin was imaged both before and after the treatment using a multi-channel time domain OCT [8]. The epidermis appeared as a thin layer with thickness around 100 μm on top of the dense dermal layer. Corticosteroid induced atrophy was observed as a decreased in the mean epidermal thickness from 74 to 61 μm. OCT in conjunction with ultrasound (US) has been used to quantify the effects of different topical corticosteroid (TCS) compounds epidermal and dermal thickness [9]. The effects due to the daily application of 50 mg of TCS compounds in potency classes I-IV plus placebo (steroid-free cream base) were studied at time points of 0, 3, 7, 14, 21, 28 days and 3-months. Interestingly a reduction in mean epidermal thickness of >20% was observed for all 4 TCS compounds and placebo and control measurements however the effect was more evident with increasing TCS potency. The design of the experiment meant that the control site was adjacent to the five sample sites which could lead to cross contaminations. A further analysis showed that there was no correlation between the thinning at the control site and the potency of the TCS compound applied to the adjacent site (which was randomized between subjects). The authors postulated that the thinning of the control site was a systemic effect. This pattern was also observed in the dermal thickness but to a lesser

extent. The weaker response demonstrates the advantage of OCT's higher resolution. Also the epidermis is fundamentally a more sensitive maker to skin atrophy and hence shows changes at earlier stage.

Both the ultrasound and OCT systems showed a recovery of skin layer thickness towards the baseline between the end of the treatment at day 28 and the final 3 month time point. The effects of twice daily application of clobetasol proprionate 0.05% over a 14 day period has been studied in a cohort of 13 young female volunteers [10]. OCT showed that the TCS produced significant epidermal thinning over the 14 days and also showed a recovery to baseline after the end of the treatment. An increase in stiffness and reduction in viscoelasticity were measured using mechanical testing, these effects were also reversible at the end of the treatment.

5.3 Method

A small cohort pilot study was undertaken consisting of 4 healthy volunteers, none of whom had any contraindications for treatment using either compound. Ethical consent was obtained from the Sheffield NHS Trust. The treatment protocol was as follows. The measurements were done on the volar forearm skin. The left hand of the volunteers was chosen to receive either the TCS or the non steroidal anti-inflammatory drug (NSAID) and the right arm received the other compound. Volunteers were unaware of which arm received which drug until the data analysis was completed. Measurement of each subject was done before the commencing of the study and at the end of the treatment (day 14). The actual treatment consisted of covering the entire forearm with 2 fingertip units (FTU) of cream twice daily [11].

Three different measurement protocols were employed in the progression of the pilot study. Firstly, for subject 1, a single measurement site was scanned prior to the treatment and at the end. Natural anatomical markers such as moles were used as location references to allow the measurement site to be revisited for measurement at the end of the treatment. Secondly for subject 4 the site imaged at the beginning of the study was maintain for future imaging by using ink markers. Further more a 3 $\times$ 3 grid of measurements was collected at the end of the study. The midpoint between the elbow and the wrist was marked with a pen, then a rectilinear grid of points with 1.5 cm spacing in both the distal/proximal and lateral/medial directions was marked out. A single B scan image was collected at each grid point; the scan orientation was always along the distal/proximal line. The measurements were done for subjects 2 and 3 at baseline and post-treatment.

For subjects 2, 3 and 4 the imaging was done on a commercial multi-channel OCT system (Michelson Diagnostics Ltd EX1301). The system is swept source based OCT using a Santec HSL-2000 swept laser with a sweeping range of 150 nm around 1310 nm. The system has improved lateral resolution due to its four independently focussed

sample beam. The images from each beam are stitched together using a proprietary algorithm to produce an image with resolution of 7.5 μm in both the axial and lateral direction. For subject 1 a home built modified version of this system was used. A home built fibre interferometer which used Thorlabs' LSM03 OCT objective to illuminate the sample however the light source, data acquisition hardware and software were the same as that used on the other subjects. B scans from this modified system yielded a lateral resolution of around 18 μm.

Quantitative data analysis of the epidermal thickness of subjects 2-4 were carried out by an independent operator who was blind to the hypothesis under test. The epidermis shows up as a hypoechogeneic layer situated on top of the brighter dermal layer. To help with the accuracy in measuring the epidermal thickness each image was rotated to get the epidermis layer to be horizontal. After the rotation a polygon region of interest tool was used to manually select the epidermal layer. Both of these processes were completed using ImageJ version 1.47. The geometric area and lateral extension of this region of interest was also measured using Image J. Figure 5.1 shows the original B scan and the rotated B scan with the highlighted ROI.

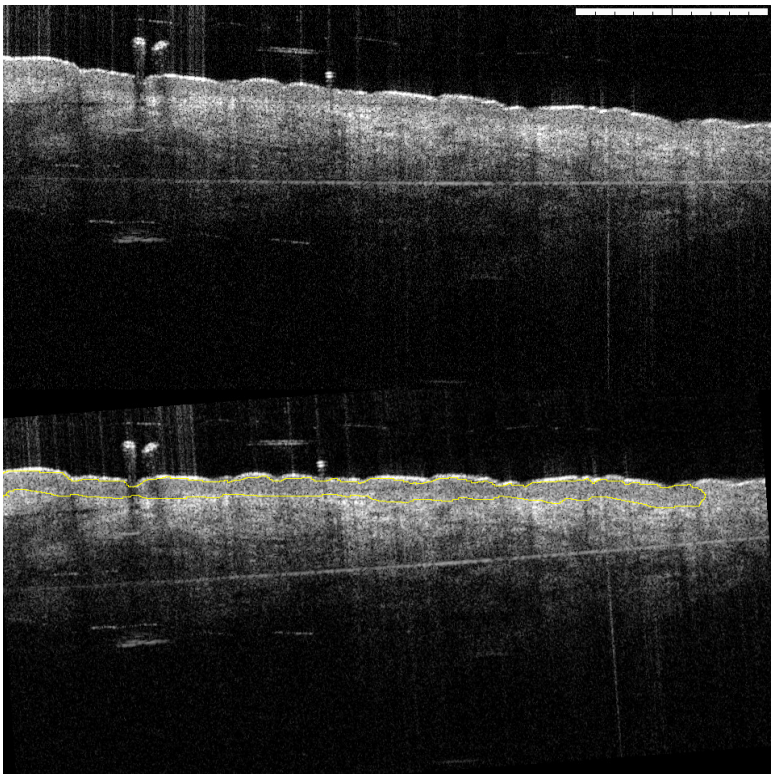

Figure 5.1: Raw B scan (above figure)and the rotated B scan with the epidermis (ROI) highlighted

The ratio of the geometric area and the lateral extension was then used to calculate the mean epidermal thickness. Some B scans were excluded in the calculations if the operator could not clearly identify an epidermal layer extending over at least 25% of the total B-scan.

A paired two-sided Student t-test was conducted to test the null hypothesis that the means of each grid were identical. The data was paired into matching sites on the forearm, before and after treatment. In the case of subject 4 a grid of values was not available at the baseline so to make use of this, a comparison between equivalent regions on the left and right forearms was done. This comparison would identify if there was a significant difference in the left and right epidermal thickness after the treatment.

5.4 Results

Below are individual B scans of before and after treatment for subject 1.

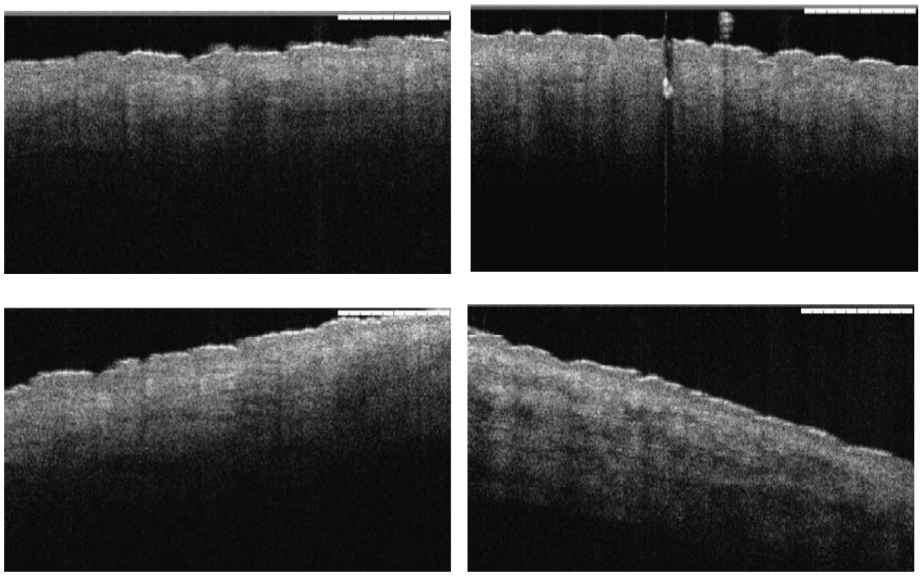

Figure 5.2: B scans before(upper row)and after (lower row) 14 days of treatment with (left column) Tacrolimus and (right column) BMV.

From figure 5.2 it is clearly evident that the epidermis after treatment with BMV image is thinner, compared to the upper right image recorded at baseline. This suggest that the Betamethasone valerate (BMV) has lead to epidermal atrophy. An interesting observation is also made on the dermis. The backscatter appears more heterogeneous making the image penetration depth seem greater. This effect is also observable in figures 3 & 4 of Cossmann and Welzel [9] and hence may indicate disruption of the dermal collagen structures, in addition to epidermal thinning. This should be further investigated. It is possible that the BMV alters the scattering coefficient of the dermis and hence light travels deeper.

With the 3×3 grid data for volunteers 2 and 3 a quantitative comparison was done, using the methods previously described. The tables in table 5.1 shows the mean (across all valid sites) epidermal thickness prior to and after treatment for both forearms. The left table is for subject 2 and the data for subject 3 is in the table on the

	BMV	Tacrolimus
Pre-	89 ± 0.5 μm	83 ± 0.5μm
Post-	69 ± 0.5μm	83 ± 0.5μm
p-value	0.002	0.88

	BMV	Tacrolimus
Pre-	74 ± 0.5μm	74 ± 0.5μm
Post-	59 ± 0.5μm	83 ± 0.5μm
p-value	0.01	0.01

Table 5.1: Table showing mean pre-/ post epidermal thickness measured over 3 × 3 grid site for subjects 2 and 3. The p-values are also calculated

right.

The data from subject 2 rejects the null hypothesis and support the alternate hypothesis that the mean epidermal thickness falls by around 25% by the end of the 14 days' treatment with BMV. However, the null hypothesis is accepted with 88% confidence for the Tacrolimus measurements, hence is supports the view that the non steroidal cream does not produce epidermal atrophy. The data from subject 3 also supports the hypothesis that BMV treatment produces epidermal atrophy, observing a 20% reduction in the epidermal thickness after 14 days of treatment. Interestingly the null hypothesis is also rejected for the Tacrolimus treatment with an apparent increase in mean thickness of around 13%. To our knowledge such epidermal hypertrophy caused by Tacrolimus treatment has not previously been reported and is worthy of a more detailed study.

In order to gain quantitative data from subject 4, where a grid was only measured post-treatment, we used a pair t-test comparing matching sites on the left and right forearm. The results are displayed in the tables 5.2. Tables 5.2(a) and 5.2(b) shows the pre and post data for the left(one compound) and right forearm(other compound) for subject 2 and 3 respectively. Table 5.2(c) shows the data for subject 4.

The data from subject 2 accepts that null hypothesis that the forearms have identical epidermal thickness prior to any treatment, however, it rejects this hypothesis after treatment due to the pronounced atrophy due to the BMV. Similarly, the data from subject 3 accepts the null hypothesis pre-treatment but rejects it post treatment even more emphatically partly due to the hypertrophy caused by the Tacrolimus in

	Pre-	Post-
BMV	89±0.5 μm	70±0.5 μm
Tacrolimus	84±0.5 μm	83±0.5 μm
p-value	0.18	0.02

(a) Left and right forearm comparison data for subject 2

	Pre	Post
BMV	74± μm	60± μm
Tacrolimus	74± μm	85± μm
p-value	0.99	0.005

(b) Left and right forearm comparison data for subject 3

	Pre-	Post-
BMV		96± μm
Tacrolimus		96± μm
p-value		0.92

(c) Left and right forearm comparison data for subject 4

Table 5.2: Tables showing t-test comparison between left and right forearm with a different compound on each arm

addition to the atrophy due to the BMV. Subject 4 appears not to have any response to either compound since the epidermal thickness of the left and right forearm are identical. The non responder conclusion is drawn because it seems very unlikely that both the left and right arm decreased or increased by the same amount given the results from the previous patients.

5.5 Conclusion

In our study we have confirmed reports that epidermal atrophy due to corticosteroids cream produce significant reduction in the epidermal thickness as detected by OCT. Furthermore, we have shown that a popular non- steroidal alternative, Tacrolimus monohydrate, does not produce such thinning in any of the four volunteers. Interestingly we have found that the drug may cause epidermal hypertrophy(1 out of 4 subjects) which deserves further investigation. We also identified a single non- responder out of the four test subjects, it may be of use to investigate the prevalence of such subjects.

From comparing the results obtained to previous studies, we can conclude that OCT is a useful tool for comparison of skin atrophy of steroidal and non-steroidal anti-inflammatory skin treatments.

References

[1] P. Ovaere, S. Lippens, P. Vandenabeele, and W. Declercq, "The emerging roles of serine protease cascades in the epidermis," *Trends in biochemical sciences*, vol. 34, no. 9, pp. 453–463, 2009.

[2] C. N. Palmer, A. D. Irvine, A. Terron-Kwiatkowski, Y. Zhao, H. Liao, S. P. Lee, D. R. Goudie, A. Sandilands, L. E. Campbell, F. J. Smith, *et al.*, "Common loss-of-function variants of the epidermal barrier protein filaggrin are a major predisposing factor for atopic dermatitis," *Nature genetics*, vol. 38, no. 4, pp. 441–446, 2006.

[3] C. Flohr, K. England, S. Radulovic, W. McLean, L. Campbell, J. Barker, M. Perkin, and G. Lack, "Filaggrin loss-of-function mutations are associated with early-onset eczema, eczema severity and transepidermal water loss at 3 months of age," *British Journal of Dermatology*, vol. 163, no. 6, pp. 1333–1336, 2010.

[4] J. Gupta, E. Grube, M. B. Ericksen, M. D. Stevenson, A. W. Lucky, A. P. Sheth, A. H. Assa'ad, and G. K. K. Hershey, "Intrinsically defective skin barrier function in children with atopic dermatitis correlates with disease severity," *Journal of Allergy and Clinical Immunology*, vol. 121, no. 3, pp. 725–730, 2008.

[5] K. Wirén, C. Nohlgård, F. Nyberg, L. Holm, M. Svensson, A. Johannesson, P. Wallberg, B. Berne, F. Edlund, and M. Lodén, "Treatment with a barrier-strengthening moisturizing cream delays relapse of atopic dermatitis: a prospec-

tive and randomized controlled clinical trial," *Journal of the European Academy of Dermatology and Venereology*, vol. 23, no. 11, pp. 1267–1272, 2009.

[6] E. L. Simpson, "Atopic dermatitis: a review of topical treatment options," *Current Medical Research & Opinion*, vol. 26, no. 3, pp. 633–640, 2010.

[7] A. Coondoo, M. Phiske, S. Verma, and K. Lahiri, "Side-effects of topical steroids: a long overdue revisit," *Indian dermatology online journal*, vol. 5, no. 4, p. 416, 2014.

[8] A. Pagnoni, A. Knuettel, P. Welker, M. Rist, T. Stoudemayer, L. Kolbe, I. Sadiq, and A. Kligman, "Optical coherence tomography in dermatology," *Skin Research and Technology*, vol. 5, no. 2, pp. 83–87, 1999.

[9] M. Cossmann and J. Welzel, "Evaluation of the atrophogenic potential of different glucocorticoids using optical coherence tomography, 20-mhz ultrasound and profilometry; a double-blind, placebo-controlled trial," *British Journal of Dermatology*, vol. 155, no. 4, pp. 700–706, 2006.

[10] G. Josse, C. Rouvrais, A. Mas, M. Haftek, A. Delalleau, Y. Ferraq, F. Ossant, J. George, J. Lagarde, and A. Schmitt, "A multitechnique evaluation of topical corticosteroid treatment," *Skin Research and Technology*, vol. 15, no. 1, pp. 35–39, 2009.

[11] Z. Lu, J. Boadi, S. Danby, M. Cork, and S. J. Matcher, "Optical coherence tomography demonstrates differential epidermal thinning of human forearm volar skin after 2 weeks application of a topical corticosteroid vs a non-steroidal anti-inflammatory alternative," pp. 85650C–85650C, International Society for Optics and Photonics, 2013.

Chapter 6

Appendix

6.1 Photographs of Ultrahigh resolution OCT

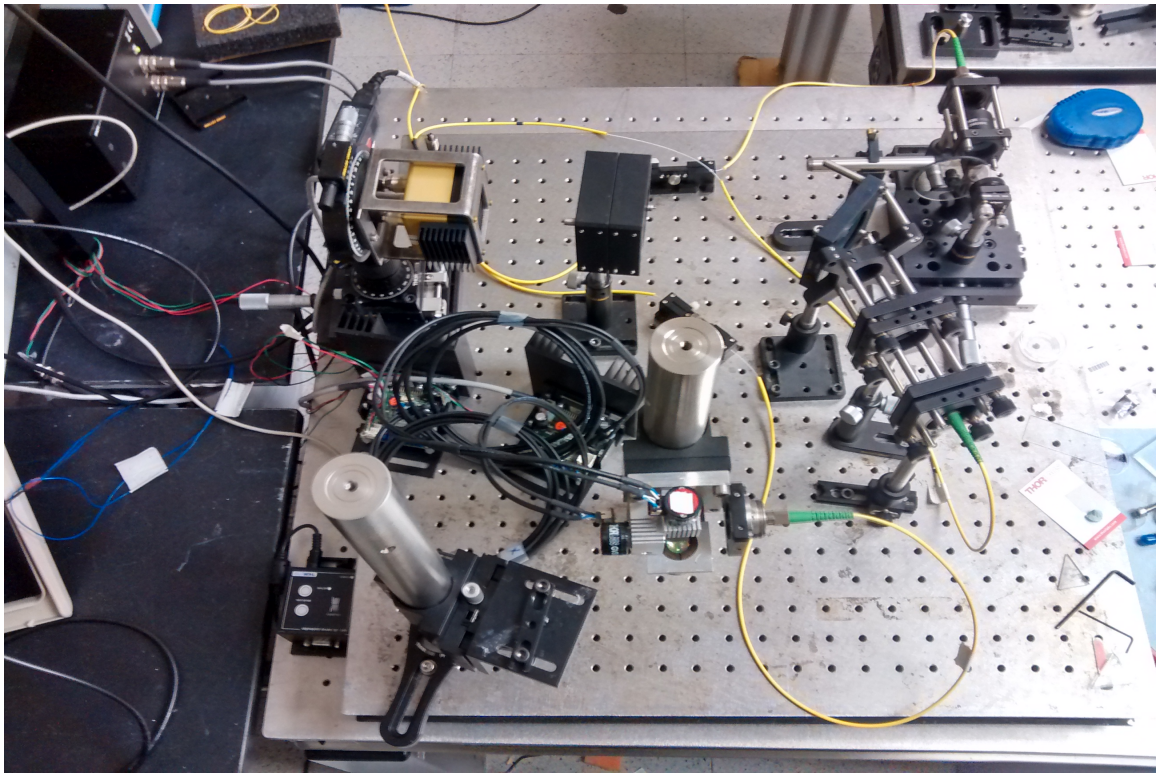

Figure 6.1: Plan view of the Ultrahigh resolution system

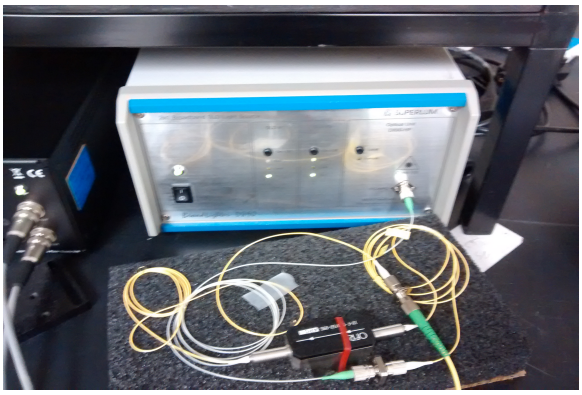

Figure 6.2: Superlum Broadlighter D890 HP light source

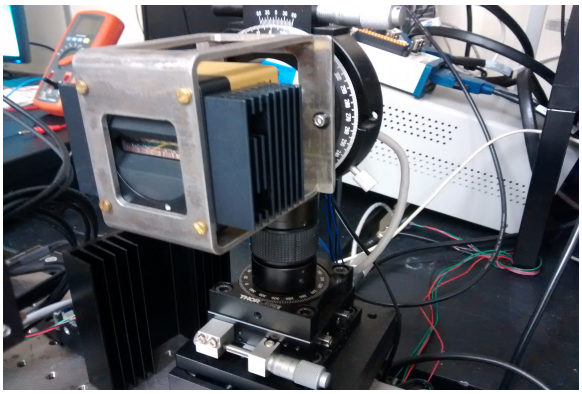

Figure 6.3: The Aviiva CCD mounted on a six degree movement stage

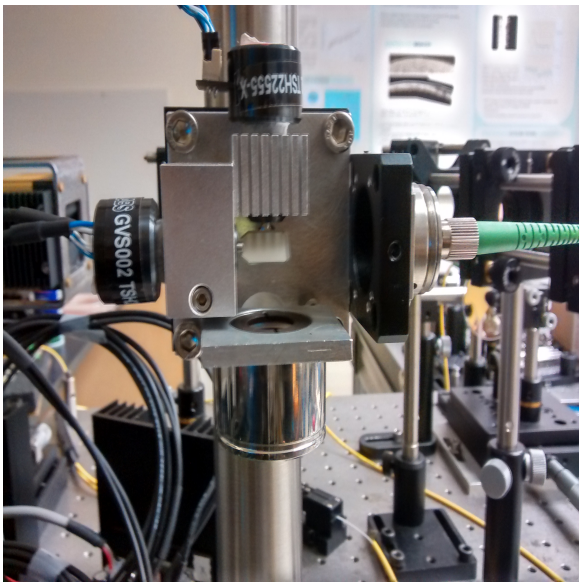

Figure 6.4: Sample arm housing the galvo scanning mirror and the telescentric lens

6.2 Phase Processing

```
MATLAB script for Phase processing

close all
fclose all
clear variables;
clc
name=['joseph'];
while name==['joseph'];
% ********************************************************
% [1] Parameter initialization
% ********************************************************

disp('* Parameter intitialization');
% default data folder ----
% PLease edit here according to your own data folder path ----
folder = 'G:\Conc3usingsmallEM';
% folder = 'C:\Documents and Settings\User\My Documents\LabVIEW Data\previous files\New
% exposure time /us
expo=50.016
% Scanning length <<xm>> should rewrite here
xm = 1;            % width in mm
 ---
*************
zm = 2.9638;        % depth in mm in air
% Refractive index depending on your sample
n = 1.44;
treshold = 0.10;
```

```
% select save processed data or not
savedata = 0;
% Optical input channel as from MD detection board
channel = 1;
% Number of samples per A-scan, as selected in image4
Ascansamples = 1024;
% Kazai autocorrelation equation parameters
de = 2;     % depth
wi = 4;     % width
% Select .oct raw data file(s) to compute
clear RDfolder RDfilelist
[RDfile RDfolder] = uigetfile({'*.oct', 'MD raw data (oct)'; ...
    '*.*', 'All files'}, 'Select .OCT raw data file to process', ...
    folder, 'multiselect', 'off');
if eq(RDfolder,0)
    % User press cancel - script interrupted
    disp('* Window closed - script interrupted');
    return
end


% ********************************************************
% [3] Compute the .oct file
% ********************************************************
disp(['* Compute .oct raw data file: ', RDfile]);

% Open selected file
fidOCT = fopen(fullfile(RDfolder, RDfile), 'r', 'b');
if fidOCT == -1
    % Error in opening the file!
    disp('*** File open error! - script interrupted');
    return
end

% Read the first part of header (4 bytes: 'M', 'D', format version '2' and variant '0';
% and use them to match the image data; % see MD documentation for details)
H0 = fread(fidOCT, 2, '*char')';
H1 = fread(fidOCT, 2, 'int8')';
if ( (strcmp(H0,'MD') == 0) || (H1(1)~= 2) || (H1(2)~= 0) )
    disp('*** The data file is not compatible with this script - please use the correct
    return
end
clear H0 H1    % fseek(fidOCT, 4, 'bof');

% Read the content of the configuration string (data as in .ini file)
l = fread(fidOCT, 1, 'long');             % Length of configuration string
Hstring = fread(fidOCT, l, '*char')';

% Extract the averaging factor value
avgfac = str2double(Hstring(findstr('AveragingFactor=', Hstring)+length('AveragingFacto
disp(['- Frame average factor: ', num2str(avgfac)]);

% Number of acquired slices: slices;
% - slices = 1 - single tomography
```

```
% - slices > 1 - multislices tomographies
slices = fread(fidOCT, 1, 'ushort')  ;
if gt(slices, 1)
    disp(['- multislices data; ', num2str(slices), ' slices']);
else
    disp('- single slice data');
end

% Read spectral table data
l = fread(fidOCT, 1, 'long');             % Length of spectral table data
ST = fread(fidOCT, l, 'long');            % Spectral table data

% Read resample table data
l = fread(fidOCT, 1, 'long');             % Length of resample table data
RT = fread(fidOCT, l, 'float');           % Resample data


% Read stray light data (4 channels)
l = fread(fidOCT, 1, 'long');                % Length of stray light channel 1
ch(:,1) = fread(fidOCT, l, 'short');         % Stray light channel 1 data
SL = ch(:,channel);
clear ch

% Read noise floor data (4 channels)
l = fread(fidOCT, 1, 'long');                % Length of noise floor channel 1
ch(:,1) = fread(fidOCT, l, 'float');         % Noise floor channel 1 data
NF = ch(:,channel);
clear ch


% Read data frame
c = fread(fidOCT, 1, 'long');             % no. of columns of raw data 2D array
% (# of acquired A-scans = # of A-scans per tomography * avgfac)
r = fread(fidOCT, 1, 'long');             % no. of rows of raw data 2D array (# of sample
RD0 = fread(fidOCT, [r c], 'short');      % raw data


for jj = 1:slices

   if gt(slices,1);
        disp(['- Computing slice no. ', num2str(jj)]);
    end

    RD = RD0(:,(jj-1) * c/slices +1 : jj * c/slices );

    % Rescale and resample the raw data from the selected input channel (channel)
    % perform steps 1-5 as from MD documentation
    % NOTE: the function is defined in this script
    RD = F_MDFresample(SL, ST, RT, RD, jj);



    % Compute the (inverse) fft to transform the raw data signal from f-space (frequancy
    disp('- Computing the DFT...');
```

```
    E = fft(RD);                                % 6. d
    clear RD ans


    xs = c/avgfac/slices;
    zs = r;

    % Taking first half of the data
    E = E(1:r/2, :);


    % Structural image, i.e. REFLECTIVITY image,
    % expressed in dB, NB: [log10] not [log] used
    S = 10 * log10( abs(E).^2 );

    %%%%%%%%%%%%%%%%%%%%%%%%%PHASE%%%%%%%%%%%%%%%%%%%%%%%%%


xaxis=(1:size(E,2))*(expo)/size(E,2);
%find surface
[val,surface]=max(S(:,500));
yaxis=(1:size(E,1));
yaxis=yaxis-surface;
yaxis=yaxis*2.5e-3;

h=imagesc(xaxis,yaxis,S);colormap gray
xlabel('$$Time /\mu s$$','Interpreter','latex');
ylabel('$$Depth/mm$$','Interpreter','latex');
title('$$\textit{M mode scan of Gelatine/Milk Phantom}$$','Interpreter','latex')
set(findall(gcf,'type','text'),'fontSize',16,'Interpreter','latex');
axis([0 inf -0.09 1])
line=repmat(20e3,[0 1000]);
hold on; plot(xaxis,20e-3,'g-');
%  print -depsc Gelatinphantom.eps

%      [x,posn]=ginput(1)
posn=20e-3; %distance below surface 20microns


    %PHASE%%%%%%%%%%
phase=(angle(E));
Phase=phase(:,1:1000);

    %index value posn=pix below+surface position
posn2=(posn/2.5e-3)+surface;
standdev=std(Phase(posn2,1:999))


P=figure(); plot(xaxis,Phase(posn2,:))
xlabel('$$Time /\mu s$$','Interpreter','latex');
ylabel('$$Phase /rad$$','Interpreter','latex');
title('$$\textit{Phase Fluctuation of Gelatine/Milk Phantom}$$','Interpreter','latex')
set(findall(gcf,'type','text'),'fontSize',16,'Interpreter','latex');
```

```
axis([-inf 50.5 -inf inf])
print -depsc highPhase.eps



    %FFT of phase measurement -to find freq of oscillation&&&7
FFT_phase=(abs(fft(Phase(posn2,:)))).^2;
s=size(FFT_phase,2)+1;
FFT_phase1=(FFT_phase(1:s/2)); %select only positive frequency
FFT_len=length(FFT_phase1);
xax= (1:FFT_len)/(FFT_len)*(0.5*1e3/expo);
FF=figure(); plot(xax,((FFT_phase1)));
clear s; s=max(FFT_phase1(8:end));
axis([0 2 -inf inf])
xlabel('$$Frequency /kHz$$','Interpreter','latex');
ylabel('$$\textit{Phase sq}  /rad^\textit{2}$$','Interpreter','latex');
title('$$\textit{FFT of Phase Fluctuation}$$','Interpreter','latex')
set(findall(gcf,'type','text'),'fontSize',16,'Interpreter','latex');
print -depsc highFFT_Phase.eps
print -depsc FFT_Phase.eps

end
end
```

6.3 MATLAB Script for MMOCT processing

```
% Process OCT file and produce Structural image data set S
%

%     SNR improvement / smooth the image
    S = F_SNRimprovement(S,de,wi,treshold);

        figure;imagesc(S);
        title(['Structural Image', num2str(jj)]);
        xlabel('Width (\itmm\rm)');
        ylabel('Depth (\itmm\rm)');
        colormap gray;
%         imwrite(S,'Structural.png');
 print('-dpng','-r72','Structure.png')

%Find Phase
angleE=angle(E);

%length of signal
len=size(angleE,2);

xx=linspace(1,(Acq/2),(len/2));

% %Unwrap 2pi
unwrapD=unwrap(angleE,[],2);
```

```
%max displacement
displacement= unwrapD.*((890e-9)/(4*pi*1.3));
maxDisp=max(max(displacement))

%differentiate to remove time independent phase
diffAngle=diff(unwrapD,1,2);
displacement= diffAngle.*((890e-9)/(4*pi*1.3));
maxDisp2=max(max(displacement))

%fft of unwrap phase this shows the freqs in phase
% NFFT=2^nextpow2(size(diffAngle));%fft length
aFFT=((fft(diffAngle')));
% meanaFFT=mean(aFFT,2);
aFFT=aFFT(1:len/2,:);
figure;plot(xx,(abs(aFFT)).^2); title('Absolute FFT of unwrapped Phase');
xlabel('Frequency/Hz');
aFFTnoise=mean(mean(abs(aFFT(2000:end,:)).^2));
[b_cut a_cut]=butter(5,[0.29 0.35],'bandpass');  %160Hz
H=freqz(b_cut,a_cut,(len/2)); % freq response of filter
figure; plot(xx,abs(H))% see filter frequency response
title('Filter Freq Response');xlabel('Frequency/ Hz');
print('-dpng','-r72','Filter.png')

for nn=1:size(unwrapD,1);
    phase_filtered(nn,:)=filter(b_cut,a_cut,diffAngle(nn,:));
end
figure; imagesc(phase_filtered);
title('Filter Phase Image');

yy=abs(fft(phase_filtered')).^2;

figure; plot(xx,(yy(1:(len/2),:))); title('Filtered absolute FFT of unwrapped phase');
xlabel('Frequency/Hz');
clear yy
print('-dpng','-r72','FilterdabsoluteFFT.png')

%%%SLIDING WINDOW
win_width = 100;  %Sliding window width
slide_incr = win_width;  %Slide for each iteration

%windowing function
win = hamming((win_width +1), 'periodic');
%repeat window to fit all of data matrix
win=repmat(win,[1 size(phase_filtered,1)]);
%place window matrix onto GPU
%win=gpuArray(win);

nfft=(2^nextpow2(win_width));%fft length
X=(phase_filtered); %place data on gpu
stft=zeros(size(phase_filtered,1),len-win_width-1); %preallocate final matrix on gpu
% stft=gpuArray.zeros([800 50]);
% X=gpuArray(diffAngle);
```

```
%windowing

h=waitbar(0,'wait...');

for ii = 1:(len-win_width-1);
    waitbar(ii/(len-win_width-1),h,sprintf('%d',ii))
%    mean_win(ii) = mean(a(ii:ii+win_width));%Calculation for each window
%     X=gpuArray(phase_filtered(nn,ii:ii+win_width));
    Xi=X(:,ii:ii+win_width);
    Xi=Xi.*win';
    temp=(abs(fft(Xi,nfft,2))).^2;
    stft(:,ii)=((temp(:,22)));%160
end

close(h);

STFT=gather(stft);

figure;imagesc(STFT);
colormap jet
colorbar
  print('-dpng','-r72','STFT.png')
end
```